

DUAL BAND HYPERSPECTRAL IMAGING SPECTROMETER

By

John Paul Hartke

---

A Dissertation Submitted to the Faculty of the

COLLEGE OF OPTICAL SCIENCES

In Partial Fulfillment of the Requirements  
For the Degree of

DOCTOR OF PHILOSOPHY

In the Graduate College

THE UNIVERSITY OF ARIZONA

2005

THE UNIVERSITY OF ARIZONA  
GRADUATE COLLEGE

As members of the Dissertation Committee, we certify that we have read the dissertation

prepared by John Paul Hartke

entitled DUAL BAND HYPERSPECTRAL IMAGING SPECTROMETER

and recommend that it be accepted as fulfilling the dissertation requirement for the

Degree of Doctor of Philosophy

\_\_\_\_\_ Date: June 20, 2005  
Eustace L. Dereniak

\_\_\_\_\_ Date: June 20, 2005  
William J. Dallas

\_\_\_\_\_ Date: June 20, 2005  
Paul D. LeVan

Final approval and acceptance of this dissertation is contingent upon the candidate's submission of the final copies of the dissertation to the Graduate College.

I hereby certify that I have read this dissertation prepared under my direction and recommend that it be accepted as fulfilling the dissertation requirement.

\_\_\_\_\_ Date: June 20, 2005  
Dissertation Director: Eustace L. Dereniak

### STATEMENT BY THE AUTHOR

This dissertation has been submitted in partial fulfillment of requirements for an advanced degree at The University of Arizona and is deposited in the University Library to be made available to borrowers under rules of the Library.

Brief quotations from this dissertation are allowable without special permission, provided that accurate acknowledgment of source is made. Requests for permission for extended quotation from or reproduction of this manuscript in whole or in part may be granted by the head of the major department or the Dean of the Graduate College when in his or her judgment the proposed use of the material is in the interests of scholarship. In all other instances, however, permission must be obtained from the author.

SIGNED: John Hartke

## ACKNOWLEDGEMENTS

There have been many people and organizations that have contributed to this work who need to be acknowledged and thanked. First, I would like to acknowledge and thank the United States Army and the United States Military Academy for allowing me time to earn this degree, especially while the nation is at war. I would also like to thank Lee Hudson from LumiLed Lighting for providing the blue LEDs used in this work and Paul Horton for his insight into the dual band infrared focal planes.

There have been numerous people within the College of Optical Sciences and particularly the Optical Detection Group who have shared ideas and offered assistance. In particular, I would like to thank: Chris Tebow, Anne Locke, Brian Kinder, Nathan Hagen, Jim Scholl, Margy Green, Andrea Amaro, Dave Salyer, Tomasz Tkaczyk, and John Tamkin.

The faculty of the College of Optical Sciences has been extremely supportive and helpful in the completion of this work. In particular I would like thank Tom Milster, H Angus Macleod, and Kurt Thome. I would also like to give a special thanks to my committee for their input, guidance, and support: Eustace Dereniak, William Dallas, and Paul LeVan from Air Force Research Labs, for their guidance, patience and support.

None of this would have been possible without the love and support of my wife, Lisa, and children, Matthew and Alexandra. I am forever grateful.

## TABLE OF CONTENTS

LIST OF ILLUSTRATIONS. ....	7
LIST OF TABLES. ....	10
ABSTRACT .....	11
1. BACKGROUND .....	12
1.1. IMAGING SPECTROMETRY .....	12
1.2. USES OF IMAGING SPECTROMETRY .....	13
1.3. CONVENTIONAL IMAGING SPECTROMETERS .....	14
1.4. CTIS OPTICAL SYSTEM .....	16
1.5. LIMITS ON CTIS .....	17
1.6. RESEARCH OBJECTIVES .....	18
2. COMPUTED TOMOGRAPHIC IMAGING SPECTROMETER IMAGING SCIENCE .....	19
2.1. TOMOGRAPHY .....	20
2.2. RADON TRANSFORM .....	22
2.3. INVERSE PROBLEM .....	29
2.4. RECONSTRUCTION TECHNIQUES .....	31
2.4.1. EM RECONSTRUCTION ALGORITHM .....	32
2.4.2. MART RECONSTRUCTION ALGORITHM .....	33
2.5. CTIS MODEL /H-MATRIX CONSTRUCTION .....	35
2.5.1. CTIS MODEL .....	35
2.5.2. H-MATRIX CONSTRUCTION .....	36
2.6. DATA CUBE .....	38
2.7. SPATIAL RESOLUTION .....	39
2.8. SPECTRAL RESOLUTION .....	41
2.9. Radiometric Resolution .....	42
2.10. ORDER OVERLAP .....	43
2.11. DUAL BAND THEORY .....	45
3. COMPUTER GENERATED HOLOGRAPHIC DISPERSER .....	48
3.1. CGH DESIGN ALGORITHM .....	49
3.2. RECTANGULAR PHASELS .....	55
3.3. ETCH DEPTH QUANTIZATION .....	56
3.4. DESIGN EVALUATION .....	60
4. DUAL BAND VISIBLE CTIS PROOF OF CONCEPT .....	64
4.1. PROOF OF CONCEPT .....	64
4.2. EXPERIMENTAL SET-UP .....	66
4.3. CALIBRATION PROCEDURES .....	70
4.4. RESULTS .....	74
4.4.1. SPATIAL RESULTS .....	74
4.4.2. SPECTRAL RESULTS .....	78
4.5. ERROR ANALYSIS .....	83
4.6. CONCLUSIONS .....	86
5. DUAL BAND INFRARED CTIS DESIGN .....	87

TABLE OF CONTENTS – *Continued*

5.1. DESIGN APPROACH / ASSUMPTIONS .....	87
5.2. DESIGN SPECIFICATIONS .....	87
5.3. DUAL BAND INFRARED FOCAL PLANE ARRAYS .....	88
5.3.1. QUANTUM WELL INFRARED PHOTODETECTORS (QWIP) .....	89
5.3.2. HgCdTe DETECTORS .....	92
5.4. CGH DESIGN .....	96
5.5. OPTICAL DESIGN .....	104
5.5.1. OPTICAL COMPONENTS .....	111
5.5.2. OPTICAL DESIGN .....	112
6. CONCLUSIONS AND FUTURE WORK .....	120
6.1. CONCLUSIONS .....	120
6.2. FUTURE WORK .....	121
APPENDIX A: LINEAR SHIFT INVARIANCE .....	124
APPENDIX B: CGH DESIGN RESULTS .....	136
APPENDIX C: VISIBLE CTIS RESULTS .....	141
APPENDIX D: IR CTIS PARAMETERS .....	159
REFERENCES .....	161

## LIST OF ILLUSTRATIONS

Figure 1.1: Dual band dispersion of two data cubes. ....	13
Figure 1.2a: Schematic of a whiskbroom system. ....	15
Figure 1.2b: Schematic of a pushbroom system. ....	15
Figure 1.3a: Data cube filling technique using whiskbroom, pushbroom, and filtered camera techniques. ....	16
Figure 1.3b: Data cube filling by CTIS. ....	16
Figure 1.4: Schematic of CTIS. ....	16
Figure 2.1: Representation of an X-ray tomographic system. ....	21
Figure 2.2. Dispersion of the monochromatic planes of the object cube.....	22
Figure 2.3: Schematic of Radon Transform in one plane of a three-dimensional distribution function. ....	23
Figure 2.4a: Geometrical description of Tomosynthesis in medical Imaging. ....	26
Figure 2.4b: CTIS first order diffraction projections of data cube. ....	26
Figure 2.4c: CTIS test object. ....	27
Figure 2.4d: Raw CTIS image of test object. ....	27
Figure 2.5: Fourier space representation of the data cube. ....	28
Figure 2.6: CTIS response to a 450 nm point source. ....	37
Figure 2.7: Differential voxel element inside the data cube. ....	39
Figure 2.8: Raw image of white light extended source. ....	44
Figure 2.9: Schematic of interwoven mixed focal plane under clustering scheme and separated color bands. ....	46
Figure 3.1: Graph of quantization of etch depth on manufactured vs ideal case. ....	57
Figure 4.1: Image of dual band visible CTIS. ....	66
Figure 4.2: Energy distribution by band for each wavelength. ....	67
Figure 4.3: CTIS calibration set-up. ....	69
Figure 4.4: Negative calibration images at 450 nm and 650 nm. ....	73
Figure 4.5: White and black bar object illuminated by 75 watt white light bulb. ....	75
Figure 4.6 a: Cut along y-pixels in white bar of blue data cube. ....	76
Figure 4.6 b: Cut along y-pixels in white bars of red data cube. ....	76
Figure 4.6 c Cut along y-pixels in red and blue bars of blue data cube. ....	77
Figure 4.6 d Cut along y-pixels in red and blue bars of red data cube. ....	77
Figure 4.7: Laser spectrum reconstruction after 8 iterations of EM compared to laser spectrum measured by Ocean Optics. ....	79
Figure 4.8 a: EM reconstructions of laser. ....	80
Figure 4.8 b: MART reconstructions of laser. ....	80
Figure 4.9: Blue diode spectrum reconstruction after 8 iterations of EM compared to spectrum measured by Ocean Optics. ....	81
Figure 4.10 a: EM reconstructions of diode. ....	82
Figure 4.10 b: MART reconstructions of diode. ....	82

LIST OF ILLUSTRATIONS – *Continued*

Figure 4.11 a: Laser spectrum reconstruction with a systematic error. ....	84
Figure 4.11 b: Diode spectrum reconstructed with a systematic error. ....	84
Figure 5.1a Allowed energy levels in a single quantum well. ....	89
Figure 5.1b Energy level splitting due to two quantum wells in close Proximity. ....	89
Figure 5.1c Energy banding due to a series of quantum wells in close Proximity. ....	90
Figure 5.1d Photocurrent produced by incident light incident on biased QWIP structure. ....	90
Figure 5.2 Schematic of dual band QWIP structure. ....	91
Figure 5.3 An HgCdTe dual band detector design. ....	93
Figure 5.4 Index of refraction curves for CGH materials in the infrared. ...	96
Figure 5.5 CGH Design patterns. ....	97
Figure 5.6a: Diffraction pattern on FPA from 16x16 CGH unit cell. ....	99
Figure 5.6b: Diffraction pattern on FPA from 8x8 CGH unit cell. ....	99
Figure 5.7a MWIR and LWIR diffraction efficiency for uniform3 pattern....	103
Figure 5.7b MWIR and LWIR diffraction efficiency for Ring pattern. ....	103
Figure 5.7c MWIR and LWIR diffraction efficiency for Hybrid pattern. ....	103
Figure 5.8 Diffraction pattern for hybrid design pattern. ....	109
Figure 5.9: Objective and field stop of CTIS system. ....	112
Figure 5.10: Sketch of reflective CTIS optical design. ....	114
Figure 5.11: Sketch of refractive CTIS optical design. ....	117
Figure A.1: Plane wave incident on an ideal lens. ....	126
Figure A.2: Ideal lens imaging a point source in the plane $z = -p$ at the off-axis position $r_0$ imaged to plane $z = q$ . ....	130
Figure B.1: Uniform 3 design pattern, 8x8 Unit Cell. ....	136
Figure B.2: Uniform 3 design pattern, 10x10 unit cell. ....	136
Figure B.3: Uniform 3 design pattern, 16x16 unit cell. ....	137
Figure B.4: Ring design pattern, 8x8 unit cell. ....	137
Figure B.5: Ring design pattern, 10x10 unit cell. ....	137
Figure B.6: Ring design pattern, 16x16 unit cell. ....	138
Figure B.7: Hybrid design pattern, 8x8 unit cell. ....	138
Figure B.8: Hybrid design pattern, 10x10 unit cell. ....	138
Figure B.9: Hybrid design pattern, 16x16 unit cell. ....	139
Figure B.10: Old design pattern, 8x8 unit cell. ....	139
Figure B. 11: Old design pattern, 10x10 unit cell. ....	139
Figure B.12: Old design pattern, 16x16 unit cell. ....	140
Figures C.1 – C.6. Calibration source output at 400 nm, 450 nm, 500 nm 600 nm, 650 nm, and 700 nm. ....	141
Figures C.7 – C.43. Cuts along constant y value of black and white bars at a given wavelength from 400 – 500 nm and 600 – 675 nm every 5 nm. ....	142

LIST OF ILLUSTRATIONS – *Continued*

Figures C.44 – C.80. Cuts along constant y value of red and blue bars at a given wavelength from 400 – 500 nm and 600 – 675 nm every 5 nm. ....	149
Figures C.81 – C.88. Reconstruction of spectral signature of HeNe laser line after 1 to 8 EM iterations. ....	155
Figures C.89 – C.96. Reconstruction of spectral signature of HeNe laser line after 1 to 8 MART iterations. ....	157

## LIST OF TABLES

Table 4.1: Relation between voxel and object extent. ....	69
Table 5.1 Comparison of mean diffraction efficiencies for the different CGH cell sizes and diffraction patterns. ....	100
Table 5.2: RMS deviation from average diffraction efficiency averaged over all wavelengths. ....	102
Table 5.3a Optimal component focal lengths and field stop size for each diffraction pattern and CGH cell size. ....	107
Table 5.3b Optimal spectral and spatial resolution and focal plane usage for each diffraction pattern and CGH cell size. ....	108
Table 5.4 IR lens material properties. ....	117
Table D1: CGH design etch depth profile. ....	159
Table D2: Objective lens specifications. ....	159
Table D3: Collimating and re-imaging lens specifications. ....	159
Table D4: Off-axis parabolic lens specifications. ....	160

## ABSTRACT

A temporally and spatially non-scanning imaging spectrometer covering two separate spectral bands in the visible region using computed tomographic imaging techniques is described. The computed tomographic techniques allow for the construction of a three-dimensional hyperspectral data cube  $(x, y, \lambda)$  from the two-dimensional input in a single frame time. A computer generated holographic dispersive grating is used to disperse the incoming light into several diffraction orders on a focal plane composed of interwoven pixels independently sensitive to the two bands of interest. Separating the input of the two spectral pixel types gives co-registered output between the two bands and overcomes the limitation of overlapping orders. The proof of concept in the visible is presented using a commercially available camera.

The lessons learned from the visible system are applied to a dual infrared band imaging spectrometer. Utilizing recent developments in dual band infrared focal planes a dual band imaging spectrometer is designed covering portions of the MWIR and LWIR atmospheric transmission windows. The system design includes the evaluation of recent developments in dual band infrared focal planes, the design and evaluation of the computer generated holographic disperser, and the optical elements in the system.

## **CHAPTER 1**

### **BACKGROUND**

#### **1.1. IMAGING SPECTROMETRY**

Imaging spectrometry involves the acquisition of the spatially registered spectral content of a scene of interest. A classical imaging system is a system that provides a scene's spatial radiance distribution. A spectrometer on the other hand provides the spectral radiance content of a scene or spectral signature of an object. Therefore, the objective of an imaging spectrometer is to combine these tasks and provide a spatially registered spectral content of a scene's radiance distribution.

The manifestation of an imaging spectrometer is the creation of a data cube. A data cube is a three-dimensional representation of the scene with two spatial coordinates and wavelength as the third coordinate. The value at each three-dimensional point within the data cube gives a radiometric measurement. From this data cube, we can then take slices through the data cube to analyze different characteristics of the scene. Cuts along a constant wavelength show the scene content at that wavelength. A slice at a particular spatial location gives the spectral signature of the scene at that spatial location.

A dual band computed tomographic imaging spectrometer is a spectrometer that reconstructs two data cubes simultaneously using diffractive optics and tomographic reconstruction techniques. The diffractive optics

separates the spectral content of the scene while tomographic techniques are used to reconstruct the two data cubes. The two data cubes are spatially co-registered but cover two separate regions of the spectrum. Figure 1.1 is a cartoon of how the two spectrally separated data cubes may be dispersed onto the same focal plane to maintain spatial co-registration.

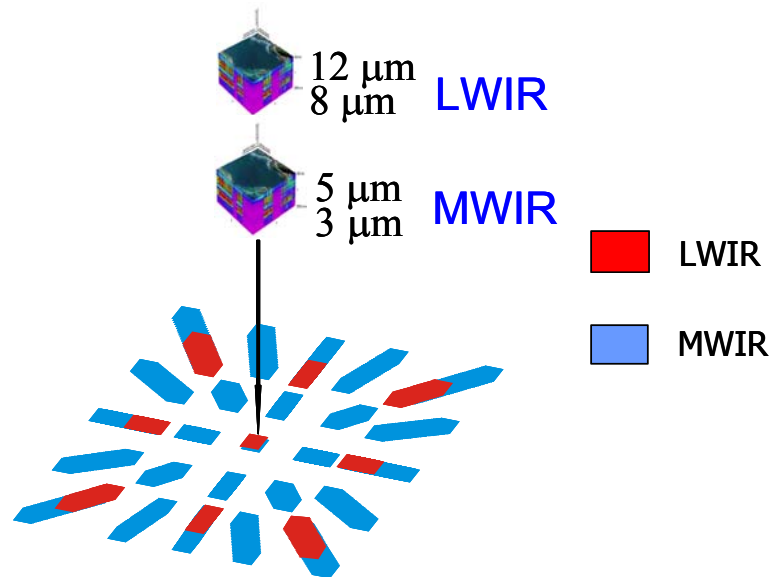


Figure 1.1 Dual band dispersion of two data cubes

## 1.2. USES OF IMAGING SPECTROMETRY

There are numerous uses of imaging spectrometry that include astronomy, resource mapping, and military applications.<sup>1</sup> Astronomers can use imaging spectrometry to classify the spectral signature and locations of distant stars, study the composition of planets, and characterize other celestial objects by their emitted and reflected spectra. Remote sensing applications include identifying natural resources and geological structures and thematic mapping.

The military can use imaging spectrometry for buried mine detection<sup>2</sup>, missile defense, and target identification.<sup>3</sup> In all of these applications the goal is the same: provide the spectral content of each spatial point in the scene.

In many cases there is an interest to investigate two separate spectral regions simultaneously. For example, the atmospheric transmission windows of 3-5  $\mu\text{m}$  and 8-12  $\mu\text{m}$  provide two infrared spectral regions to simultaneously investigate. By analyzing both spectral regions, we can increase our ability to detect targets in clutter and distinguish between targets and decoys.<sup>4</sup>

### **1.3. CONVENTIONAL IMAGING SPECTROMETERS**

Conventional means of obtaining the data cube have been pushbroom systems, whiskbroom systems, and the use of numerous spectral filters. A whiskbroom (Figure 1.2a) spectrometer obtains the spectral signature of the scene along a single x, y coordinate in the data cube. The spectral signature is obtained by placing a line of detectors behind a spectrally dispersive element giving the spectral content of a single point on the ground. The spectrometer is then swept back and forth as the detector platform moves forward obtaining the spectral signature for the rest of the scene. A pushbroom (Figure 1.2b) spectrometer is similar but gets the spectral signature along an entire line. The pushbroom system uses a two-dimensional array of detectors behind the dispersive element instead of just a linear array of detectors like in a whiskbroom system. The spectrometer only has to scan the line in one direction to complete the data cube. Although there are more detectors to calibrate in a pushbroom

system compared to a whiskbroom system, the pushbroom system has a longer dwell time than a whiskbroom thus giving a better signal to noise ratio than the whiskbroom. A third type of imaging spectrometer is a filter system which completes the data cube by obtaining information about the scene at one wavelength band at a time. A two-dimensional array is placed behind a color filter and the filter spectral band pass is changed after each integration time.

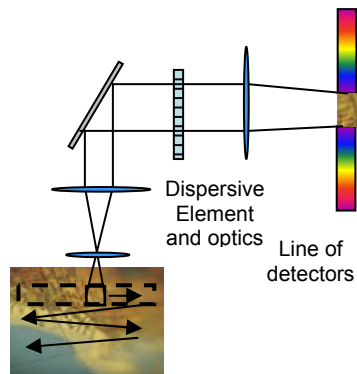


Figure 1.2a: Schematic of a whiskbroom system

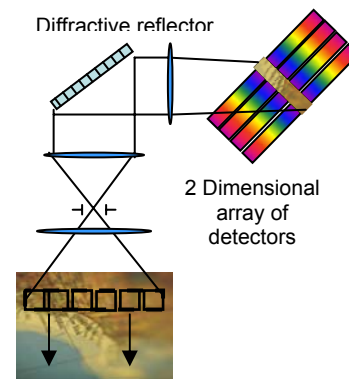


Figure 1.2b: Schematic of a pushbroom system

In all of these cases, the acquisition of the data cube takes numerous integration times to gather all the required information while the system scans either spatially as in a pushbroom or whiskbroom system, or spectrally as in a filter system. For a dynamic scene, the scene changes can occur much faster than the total data cube collection time. A Computed Tomographic Imaging Spectrometer (CTIS) uses diffractive optics and tomographic techniques to reconstruct a data cube from an image taken over a single integration time. Figures 1.3 a and b depict the data cube filling techniques.

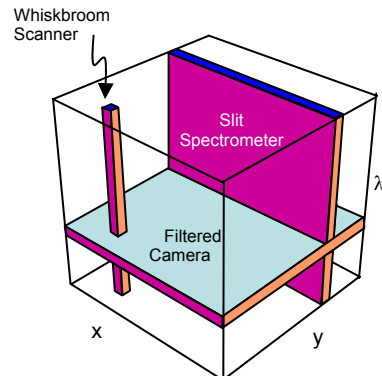


Figure 1.3a: Data cube filling technique using whiskbroom, pushbroom, and filtered camera techniques

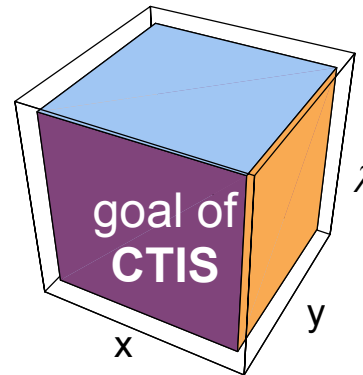


Figure 1.3b: Data cube filling by CTIS

#### 1.4. CTIS OPTICAL SYSTEM

The CTIS optical system consists of four main optical elements: objective optics, collimating optics, a disperser, and a re-imaging element. The objective takes the scene and images it to the field stop. The collimator takes the light from the field stop and collimates it to pass through the disperser. After passing through the disperser the light is re-imaged to a two-dimensional detector array. (Figure 1.4)

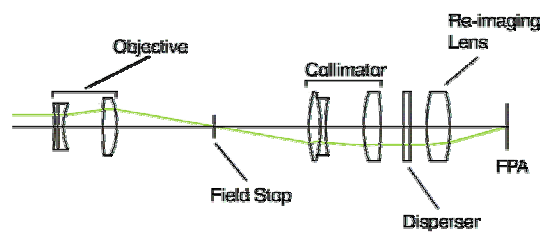


Figure 1.4: Schematic of CTIS

The CTIS system is based on the computed tomographic techniques similar to those used in medical imaging. Computed tomography involves reconstructing a three-dimensional data cube from a series of two-dimensional

projections of the object. In this system the two-dimensional projections are created by the dispersive element in the collimated space of the system. The two-dimensional projections are the diffracted images of the object's image in the plane of the field stop and constitute a series of parallel projections of the three-dimensional object cube.<sup>5</sup> The center, or zero order projection, is a direct polychromatic image of the object. The first orders are projections through the data cube at the same angle measured from the wavelength axis. A more detailed description of the CTIS system and tomography is given in Chapter 2.

### 1.5. LIMITS ON CTIS

One of the limitations of the CTIS is that the spectral bandpass of the system is limited to about one octave. The single octave limit is similar to that of a linear diffraction grating. Consider the diffraction grating equation:

$$d \sin \theta = m\lambda \quad (1.1)$$

where  $d$  is the grating period,  $\theta$  is the angle from the grating normal to the point of constructive interference,  $m$  is the order number, and  $\lambda$  is the wavelength of the light. The left side of the equation specifies the point on the observation screen where constructive interference occurs. We see from the right side of the equation that light with a 1.0  $\mu\text{m}$  wavelength in the second diffraction order ( $m=2$ ) falls in the same location as 2.0  $\mu\text{m}$  light in the first diffraction order ( $m=1$ ).

Therefore, if we have an interest in obtaining hyperspectral imaging information

over a spectral region greater than one octave or obtaining hyperspectral imaging over more than one spectral region, we must develop a technique to overcome the order overlap issue.

## **1.6. RESEARCH OBJECTIVES**

This dissertation has two main objectives:

1. Using a three-band commercially available visible camera, demonstrate the feasibility of a dual visible spectral-band hyperspectral imaging spectrometer.
2. Based on the results of the more readily available visible system, design a similar CTIS hyperspectral imaging spectrometer to simultaneously obtain data cubes in the MWIR and LWIR spectral regions.

The first objective will demonstrate the feasibility of creating a dual band hyperspectral imaging spectrometer. The second objective of designing a dual band hyperspectral imaging spectrometer over two infrared bands will lay the groundwork for a prototype system for testing. The MWIR and LWIR spectral bands were chosen to correspond with the infrared atmospheric transmission windows. Further testing of the system could allow for eventual fielding of a dual band IR CTIS system for missile defense, astronomical studies, and remote sensing.

## **CHAPTER 2**

### **COMPUTED TOMOGRAPHIC IMAGING SPECTROMETER IMAGING- SCIENCE**

This chapter will address the imaging-science theory that forms the basis of the CTIS system and how the theory is applied to the dual band CTIS problem. We will begin by describing tomography and application of the Radon transform to the forward imaging problem. We will then describe the inverse problem as it pertains to the CTIS system and the reconstruction algorithms that have proven effective with the CTIS. We will continue by discussing how the system matrix is developed and factors that determine the system's spatial, spectral, and radiometric resolution. Finally, we will apply the principles to the dual band and order-overlap problem.

We must define several terms that will be used throughout the rest of this work. The point spread function is defined as the diffraction limited ideal system response to a monochromatic point of light. The point response function is the measured system response to a real point source ignoring the spectral content of the source. The voxel response function is the measured real system response to a quasi-monochromatic point source where the spectral content of the source is considered.

## 2.1. TOMOGRAPHY

The basic theory that allows the collection of the entire data cube within a single integration time is computed tomography. Computed tomography, as applied to CTIS, involves the acquisition of a three-dimensional distribution function from two-dimensional projections of the distribution. The mathematical basis for tomography was first proposed by Johann Radon in 1917.<sup>6</sup> Ziedses des Plantes formed the principles of longitudinal or conventional tomography in 1932.<sup>7</sup> The techniques were then applied to medical imaging using X-rays in computer-assisted transaxial tomography, or simply computed tomography, and resulted in the Nobel Prize in 1979 for A.M. Cormack and G.N. Hounsfield.<sup>8</sup> Today computed tomography is just one of many three-dimensional imaging techniques that are used with ultrasound, microwaves and nuclear magnetic resonance as a part of diagnostic radiology.<sup>9</sup> The three-dimensional imaging techniques have also been applied to mapping mineral deposits using cross-borehole imaging.<sup>10</sup>

One of the first applications of computed tomography is the case of X-ray imaging of the human body. X-rays traverse the body and the attenuation dependant transmission of the X-rays are measured (Figure 2.1). Each tissue type of the body (bone, muscle, etc.) has a different attenuation coefficient for X-rays. The image acquired at the detectors is a projection of the X-ray attenuation of the body at that given angle. The X-ray source and detectors are now rotated to another projection angle through the body and the process repeated.

Reconstruction techniques are then employed in this nonlinear problem to map the attenuation coefficients and the related tissue types within the body.

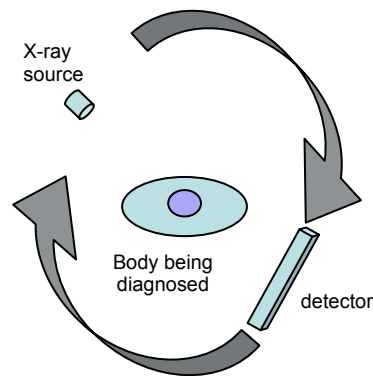


Figure 2.1: Representation of an X-ray tomographic system. The X-ray source is rotated around the patient with the detector opposite the source. One rotation gives a single slice of the body. The source and detector are moved down the body to get multiple slices.

The computed tomographic techniques in the CTIS system are similar; but instead of mapping the attenuation coefficients of body tissues, CTIS maps the spectral content of an object using diffractive optics. As discussed in Chapter 1, the goal of the CTIS system is to reconstruct the data cube in a single integration time. Comparing the CTIS system to the X-ray computed tomographic systems, the data cube is like the human body and the diffraction orders are like rotated X-ray attenuation projections. Each diffraction order is an image of the projection of the data cube at the diffraction angle. Therefore, the zero order is a direct polychromatic image of the object. The first diffracted order is a projection of the data cube at a relatively small angle, while the second and third diffraction orders are projections at increasing diffraction angles.

If we consider the data cube as a series of monochromatic images stacked on top of each other, then the diffracted projections of each of the monochromatic planes are slightly displaced from each other on the detector array (Figure 2.2). When the diffraction angle is increased at higher orders, the separation between the monochromatic projections of the field stop on the focal plane array also increases. Reconstruction techniques then reassemble the data cube based on the projections.

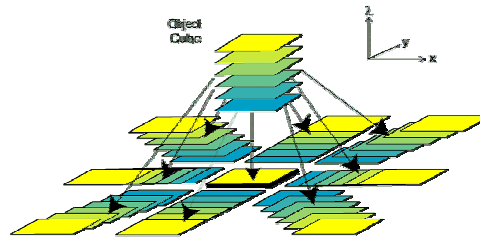


Figure 2.2. Dispersion of the monochromatic planes of the object cube

## 2.2. RADON TRANSFORM

Much of the mathematical description of tomography is contained in the Radon transform. The Radon transform is an integral transform along a plane through the body of interest. The three-dimensional Radon transform is defined as:

$$\lambda(p, \hat{\mathbf{n}}) = \int_{-\infty}^{\infty} f(\mathbf{r}) \delta(p - \mathbf{r} \cdot \hat{\mathbf{n}}) d^3 r \quad (2.1)$$

where  $\lambda$  is the Radon transform of  $f(\mathbf{r})$ ,  $\int_{-\infty}^{\infty} d^3 r$  is the integral over the three-dimensional infinite space,  $p = \mathbf{r} \cdot \hat{\mathbf{n}}$  is the plane of integration,  $f(\mathbf{r})$  is the three-dimensional function of interest, and  $\hat{\mathbf{n}}$  is a three-dimensional unit vector that is

defined by two polar angles. The result of the Radon transform is the reduction of the three-dimensional distribution function to a two-dimensional function.

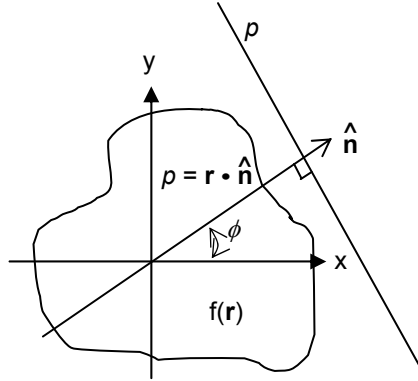


Figure 2.3: Schematic of Radon Transform in one plane of a three-dimensional distribution function. The integral is repeated at all angles  $\phi$  and at all angles  $\theta$  measured from the normal to the plane of the paper

One of the useful properties of the Radon transform is the central-slice theorem that comes from taking the one-dimensional Fourier transform of the Radon transform with respect to  $p$ . Taking the one-dimensional Fourier transform of equation (2.1) we find:

$$\Lambda(\sigma, \hat{\mathbf{n}}) = [\mathcal{F}_1 \lambda(p, \hat{\mathbf{n}})](\sigma) = \int_{-\infty}^{\infty} d^3 r f(\mathbf{r}) \int_{-\infty}^{\infty} dp \exp(-2\pi i \sigma p) \delta(p - \mathbf{r} \cdot \hat{\mathbf{n}}). \quad (2.2)$$

Here we use  $\Lambda$  as the one-dimensional Fourier transform of the Radon transform,  $\sigma$  is the transform variable, and  $\mathcal{F}_1$  as the one-dimensional Fourier transform operator. Using the sifting property of the delta function allows us to rewrite equation (2.2) as:

$$\Lambda(\sigma, \hat{\mathbf{n}}) = \int_{-\infty}^{\infty} f(\mathbf{r}) \exp(-2\pi i \mathbf{r} \cdot \hat{\mathbf{n}} \sigma) d^3 r. \quad (2.3)$$

Equation (2.3) is the three-dimensional Fourier transform where  $\hat{\mathbf{n}}\sigma$  takes the place of spatial frequency vector  $\rho$ . By fixing  $\hat{\mathbf{n}}$  at a single projection angle,  $\rho$  becomes a plane passing through the origin in the three-dimensional frequency space. Equation (2.3) tells us that the one-dimensional Fourier transform of a projection  $\lambda(p, \hat{\mathbf{n}})$  is equal to the three-dimensional Fourier transform of the original distribution,  $f(\mathbf{r})$ , evaluated along a plane through the origin in Fourier space.

The power of the central-slice theorem is in the inversion of the Radon transform. Rewriting the central-slice theorem in operator form:

$$\mathcal{F}_3 = \mathcal{F}_1 \mathfrak{R}_3 \quad (2.4)$$

as long as we evaluate the three-dimensional Fourier transform at  $\rho = \hat{\mathbf{n}}\sigma$ . Here  $\mathcal{F}_3$  is the three-dimensional Fourier transform operator,  $\mathcal{F}_1$  is the one-dimensional Fourier transform operator, and  $\mathfrak{R}_3$  is the three-dimensional Radon transform operator. Using equation (2.4) we represent the inverse Radon transform in terms of the Fourier transforms:

$$\mathfrak{R}_3^{-1} = \mathcal{F}_3^{-1} \mathcal{F}_1. \quad (2.5)$$

Now we have a tool to reconstruct the object of interest by using an inverse Radon transform algorithm. We start by replacing the operator forms of equation (2.5) with their integral forms:

$$\begin{aligned}
[\mathcal{F}_3^{-1}\mathcal{F}_1\lambda](\mathbf{r}) &= \int_{\frac{1}{2}S} d\Omega \int_{-\infty}^{\infty} |\sigma|^2 d\sigma \exp(2\pi i \mathbf{r} \cdot \hat{\mathbf{n}} \nu) \int_{-\infty}^{\infty} dp \lambda(p, \hat{\mathbf{n}}) \exp(-2\pi i \sigma p) \\
&= \int_{\frac{1}{2}S} d\Omega \int_{-\infty}^{\infty} d\sigma \exp(2\pi i \mathbf{r} \cdot \hat{\mathbf{n}} \sigma) |\sigma|^2 \Lambda(\sigma, \hat{\mathbf{n}}). \tag{2.6}
\end{aligned}$$

We can treat the integral over  $\sigma$  as the inverse Fourier transform of  $|\sigma|^2 \Lambda(\sigma, \hat{\mathbf{n}})$  and rewrite the integral portion of equation (2.6) as:

$$\int_{-\infty}^{\infty} d\sigma \exp(2\pi i \mathbf{r} \cdot \hat{\mathbf{n}} \sigma) |\sigma|^2 \Lambda(\sigma, \hat{\mathbf{n}}) = \hat{\lambda}(\mathbf{r} \cdot \hat{\mathbf{n}}, \hat{\mathbf{n}}) \tag{2.7}$$

Here  $\hat{\lambda}(\mathbf{r} \cdot \hat{\mathbf{n}}, \hat{\mathbf{n}})$  is the filtered version of  $\lambda(p, \hat{\mathbf{n}})$  where  $|\sigma|^2$  is the filter function.

Now the inversion of the Radon transform can occur by back-projecting the filtered  $\Lambda$  function:

$$f(\mathbf{r}) = [\mathcal{R}_3^{-1}\lambda](\mathbf{r}) = \int_{\frac{1}{2}S} d\Omega \hat{\lambda}(\mathbf{r} \cdot \hat{\mathbf{n}}, \hat{\mathbf{n}}). \tag{2.8}$$

The term back-projection refers to integrating back along all projection angles.<sup>11</sup>

The discussions so far have been for systems that obtain a full compliment of projections. In practice, there are numerous geometries that employ tomography principles, few for which a full complement of projections are obtained. Limited angle tomography is defined as a system where there are a limited, but continuous, range of angles available for reconstruction. The CTIS system is limited in both the angles available and the number of projections at each angle through the data cube. The geometry of the CTIS system allows us to classify it more precisely as a tomosynthesis system. In conventional

longitudinal tomography, the source and detector rotate around the object to be reconstructed. Figures 2.4 a and b compare a limited angle tomographic system to the CTIS. A tomosynthesis system is a version of longitudinal tomography where the source rotates above the object while the detectors rotate below the object. There is a plane at the vertex of the cone described by the rotation of the source called the tomographic plane.<sup>12</sup> The other planes of interest are blurred. Although there is no emitting source for which we measure the attenuation in a CTIS system, the effect of the disperser is similar in that the three-dimensional object cube is projected into a series of two-dimensional diffraction orders. Figure 2.4d demonstrates the blurring of the object in Figure 2.4c due to the disperser in the CTIS.

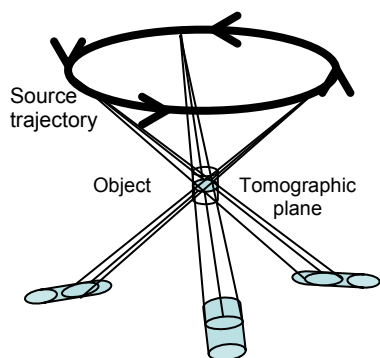


Figure 2.4a: Geometrical description of tomosynthesis in medical imaging

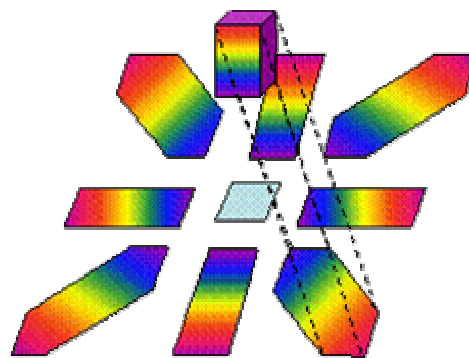


Figure 2.4b: CTIS first order diffraction projections of data cube



Figure 2.4c: CTIS test object

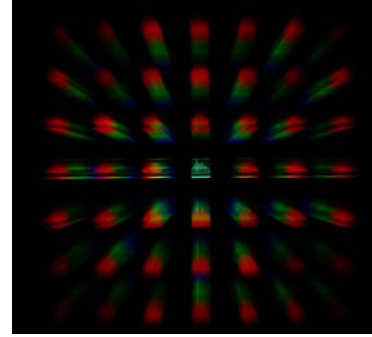


Figure 2.4d: Raw CTIS image of test object in Figure 2.4b imaged to the +/- 3 diffraction orders

A complete, detailed mathematical model of the forward problem of the CTIS system was described by Michael Descour and Curtis Volin in their dissertations by:<sup>13</sup>

$$g(\mathbf{r}') = \sum_j \iiint d^2r d\lambda f(\mathbf{r}, \lambda) t_j(\lambda) \delta(\mathbf{r} - \mu \mathbf{r}' + \mu m_j \lambda \hat{\mathbf{r}}'_j), \quad (2.9)$$

where the index  $j$  is the sum over diffraction orders. The vector  $\mathbf{r}$  is the two-dimensional position vector in the data cube. The  $\mathbf{r}'$  vector is the two-dimensional vector in image space. The function  $t_j$  accounts for the diffraction efficiency of each order. The scalar  $\mu$  is a magnification factor from the field stop to the focal plane. The scalar  $m_j$  is a dispersion factor that is proportional to the diffraction angle and  $\hat{\mathbf{r}}'_j$  is the vector that defines the diffraction order's dispersion with the focal plane axis. Taking the two-dimensional Fourier transform of equation (2.9) and using the sifting property of the delta function, while ignoring the diffraction efficiency function, yields:

$$G_j(\boldsymbol{\rho}) = F(\xi / \mu, \eta / \mu, m_j \boldsymbol{\rho} \cdot \hat{\mathbf{r}}'_j). \quad (2.10)$$

By the central slice theorem, the Fourier transform defines a plane in the three-dimensional Fourier space for each of the diffraction projections. The zero diffraction order is the  $\zeta=0$  plane. The higher the diffraction order, the more steep the plane relative to  $\zeta=0$ . More planes in Fourier space can be obtained by increasing the number of diffraction orders or by increasing the number of projections at each order. There is a practical limit to the number of diffraction orders constrained by the size of the focal plane and the system magnification. When displaying the Fourier space representation of the projection planes through the data cube as in Figure 2.5, we see that there is a missing cone of data. This missing cone encompasses low spatial frequency and high spectral frequency features in the object.<sup>14</sup> This missing cone also corresponds to part of the null space of the system.

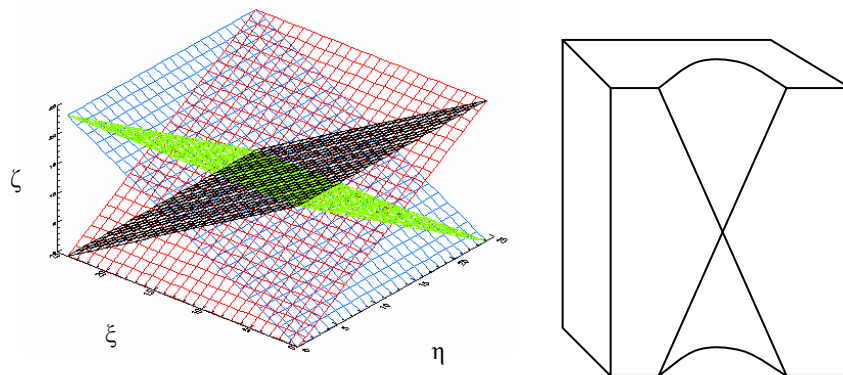


Figure 2.5: Fourier space representation of the data cube showing four diffraction projections. The missing cone is the area above (and below) the intersection of the four planes bounded by the four planes.

### 2.3. INVERSE PROBLEM

So far we have been discussing the forward problem of CTIS imaging where we have attempted to characterize the imaging system by the processes that form the image from a given object. This process can be described by the mathematical expression:

$$\mathbf{g} = \mathcal{H} \mathbf{f}, \quad (2.11)$$

where  $\mathbf{g}$  is the image vector formed on the detector array,  $\mathbf{f}$  is the continuous object, and  $\mathcal{H}$  is the continuous to discrete system operator that describes the mapping from the object to the image. This description has ignored noise. Equation (2.9) contains a detailed mathematical expression of equation (2.11) for the CTIS system. Although the development of the forward problem gives us insight into the CTIS system, it does not allow us to solve our inverse problem. In tomography, as in many imaging problems, we are given  $\mathbf{g}$  as the output of the camera or detector array; and we are trying to draw conclusions about the content of the object,  $\mathbf{f}$ . It is convenient to employ a sampling scheme on  $\mathbf{f}$  and treat the remainder of the problem as a discrete to discrete mapping. Now each element in the discrete object vector,  $\mathbf{f}$ , is a voxel of the object cube and the operator,  $\mathcal{H}$ , becomes the two-dimensional matrix operator,  $\mathbf{H}$ . If  $\mathbf{H}$  is an invertible matrix, then solving for the object,  $\mathbf{f}$ , is as simple as multiplying the image by the inverse of the  $\mathbf{H}$  operator,  $\mathbf{H}^{-1}$ .

$$\mathbf{f}=\mathbf{H}^{-1}\mathbf{g} \quad (2.12)$$

If  $\mathbf{H}$  is singular, then a true inverse does not exist and we must look to other techniques to find  $\mathbf{f}$ .

One technique to find  $\mathbf{f}$ , if  $\mathbf{H}$  is singular, is to calculate the Moore-Penrose pseudoinverse. Even if  $\mathbf{H}$  is singular and a true inverse does not exist, we can calculate the pseudoinverse by using singular value decomposition to find basis set of Eigenvectors in both object and image space. From those Eigenvectors we can calculate the Moore-Penrose pseudoinverse,  $\mathbf{H}^+$ , and find  $\mathbf{f}$  by equation (2.13):

$$\mathbf{f}=\mathbf{H}^+\mathbf{g}. \quad (2.13)$$

One of the problems with this technique is that it is computationally prohibitive. Even using sparse matrix techniques, today's computers cannot do these calculations.

Even if computational power was able to handle the pseudoinverse calculations, we know that the system matrix,  $\mathbf{H}$ , has null functions. Therefore, finding  $\mathbf{f}$  is not as simple as multiplying the image by the pseudoinverse. The object,  $\mathbf{f}$ , then consists of both a measurement component and an orthogonal null component. What this means in our problem is that there are many objects,  $\mathbf{f}$ , that can give the same image,  $\mathbf{g}$ . In addition to the null components that arise from the missing cone, when we discretized the object we created additional null components. We have continued to ignore noise and its impact on the system

and the null components. In addition to the presence of the null components limiting the effectiveness of the pseudoinverse, calculating the Moore-Penrose pseudoinverse of the  $\mathbf{H}$  matrix is computationally prohibitive in this case. For the visible system tested in this work, the  $\mathbf{H}$  matrix is 210,000 x 6,128,640 or about  $1.287 \times 10^{12}$  elements.

#### 2.4. RECONSTRUCTION TECHNIQUES

It may be more efficient to address the inverse problem in terms of an estimation problem instead of trying to invert the Radon transform, account for the null components, and calculate a pseudoinverse. We start the estimation process by assuming the system is consistent and will allow us to rewrite equation (2.13) as:

$$\hat{\mathbf{f}} = \mathbf{H}^+ \mathbf{g} \quad (2.14)$$

where  $\hat{\mathbf{f}}$  is the estimate of the object vector,  $\mathbf{f}$ . Then we want to find a solution that minimizes the residual vector given by  $\mathbf{g} - \mathbf{H}\hat{\mathbf{f}}$  using statistical methods. This then gives the estimate of the object that, when acted on by the system matrix, most closely matches the measured image. There are numerous algorithms that can be employed to calculate the estimate of the object,  $\hat{\mathbf{f}}$ .<sup>15</sup> Two algorithms have been shown to be effective by Descour<sup>16</sup> and Volin<sup>17</sup> to effectively reconstruct the CTIS data cube. The two algorithms are the Expectation

Maximization (EM) and Multiplicative Algebraic Reconstruction Technique (MART).<sup>18</sup>

### 2.4.1. EM RECONSTRUCTION ALGORITHM

The expectation maximization algorithm for reconstruction is rooted in Poisson statistics. We start by assuming that the CTIS system has signal dependent photon noise dominating the system. We then look for an estimate of the object that maximizes the probability of the measured image or maximize  $P(\mathbf{g} | \hat{\mathbf{f}})$ . Because we have assumed Poisson statistics, we can write the probability function as

$$P(g_m | \hat{f}) = \exp[-(\mathbf{Hf})_m] \frac{(\mathbf{Hf})_m^{g_m}}{g_m!} \quad (2.15)$$

where  $\mathbf{H}$  is the two-dimensional matrix representation of the system operator,  $\mathcal{H}$ , and the subscript  $m$  refers to the  $m^{\text{th}}$  pixel. We also assume that each  $g_m$  is statistically independent which allows us to express the probability function for the entire  $\mathbf{g}$  vector as:

$$P(\mathbf{g} | \hat{\mathbf{f}}) = \prod_{m=1}^M \exp[-(\mathbf{Hf})_m] \frac{(\mathbf{Hf})_m^{g_m}}{g_m!} \quad (2.16)$$

where  $M$  is the number of pixels. We can take the natural logarithm to turn the multiplication to a sum and eliminate the exponential:

$$\ln[P(\mathbf{g} | \hat{\mathbf{f}})] = \sum_{m=1}^M \left[ -(\mathbf{Hf})_m + g_m \ln(\mathbf{Hf})_m - \ln(g_m!) \right] \quad (2.17)$$

We want to find the maximum of the natural logarithm of the probability function with respect to the estimate of the object. We achieve this by taking the derivative of the natural logarithm of the probability function with respect to  $\hat{\mathbf{f}}$ , set it to zero, and solve for the maximum likelihood estimation,  $\hat{\mathbf{f}}_{\text{ML}}$ :

$$\frac{\partial}{\partial \hat{f}_n} [\ln[P(\mathbf{g} | \hat{\mathbf{f}})]] = \sum_{m=1}^M \left\{ -\mathbf{H}_{mn} + \frac{\mathbf{g}_m}{(\mathbf{H}\hat{\mathbf{f}})_m} \mathbf{H}_{mn} \right\} = 0 \quad (2.18)$$

Now we can develop an iterative process using equation (2.18) giving:<sup>19</sup>

$$\hat{f}_n^{(k+1)} = \frac{\hat{f}_n^{(k)}}{\sum_{m'=1}^M \mathbf{H}_{m'n}} \sum_{m=1}^M \mathbf{H}_{mn} \frac{\mathbf{g}_m}{(\mathbf{H}\hat{\mathbf{f}}^{(k)})_m} \quad (2.19)$$

Here  $m$  denotes the  $m^{\text{th}}$  component of  $\mathbf{g}$  and  $n$  is the  $n^{\text{th}}$  component of  $\mathbf{f}$ . We can now use equation (2.19) repeatedly until the changes in  $\hat{f}_n$  from one iteration to the next is small enough, or until we start to see noise amplification.

The advantages of the expectation-maximization algorithm are that it has a rapid, nonlinear convergence and that each iteration is, in general, a better estimate than the last. The drawback of the EM algorithm is that it has a tendency to produce high frequency spatial and spectral features, especially near the edges of the data cube.<sup>20</sup>

#### 2.4.2. MART RECONSTRUCTION ALGORITHM

The Multiplicative Algebraic Reconstruction Technique is based on finding a maximum entropy reconstruction. Entropy in this context is defined as:

$$S = -\sum_{n=1}^N f_n \ln f_n, \quad (2.20)$$

where  $n$  is the  $n^{\text{th}}$  component of  $\mathbf{f}$ .

The assumptions needed to apply MART to our problem are that  $\mathbf{g}$ ,  $\mathbf{H}$ , and  $\mathbf{f}$  are all nonnegative and the elements of  $\mathbf{H}$  are scaled to be less than or equal to one.<sup>21</sup> The iterative algorithm used to reconstruct the estimated data cube is:<sup>22</sup>

$$\hat{f}_n^{(k+1)} = \left( \frac{\mathbf{H}^T \mathbf{g}}{\mathbf{H}^T \mathbf{H} \hat{\mathbf{f}}^{(k)}} \right) \hat{f}_n^{(k)}. \quad (2.21)$$

The advantages of the MART method are that it converges very quickly and the reconstruction of high frequency objects is smoother, which reduces the high frequency spikes present in other reconstruction algorithms.<sup>23</sup> It can be advantageous to apply the MART algorithm to the estimate obtained from the EM algorithm to smooth out the high frequency artifacts created by the EM iterations.

The EM and MART algorithms are just two of many reconstruction algorithms shown to be effective at reconstructing estimates of the object. These two were discussed here because these are the two that have been used extensively with the CTIS system. The choice of reconstruction algorithm or algorithms should be based on the characteristics of the object. The EM method has a tendency to produce high frequency spikes near the edges while the MART method tends to smooth high frequency objects.

## 2.5. CTIS MODEL / H-MATRIX CONSTRUCTION

In both reconstruction algorithms, the system matrix  $\mathbf{H}$  is used to obtain the estimate of the data cube. From equation (2.9) we could develop an analytic form of  $\mathcal{H}$  if the CTIS system had a complete set of Radon transform projections at all angles through the data cube. But, the CTIS system is a limited angle tomographic system, so we must obtain  $\mathbf{H}$  with another technique. We choose to construct the  $\mathbf{H}$ -matrix using experimental techniques that are also used to calibrate the system.

### 2.5.1. CTIS MODEL

We start by modeling the CTIS system and reconstruction as a continuous-to-discrete-to-discrete mapping. That is to say, the object is spatially and spectrally continuous, the image is discretized by pixels into a two-dimensional digital camera output, and the reconstruction is a three-dimensional discrete estimate of the data cube. For the purposes of this discussion, we will continue to ignore noise. Then the  $\mathbf{H}$ -matrix describes the mapping of the object through the optical system to the image output of the camera and is described as:

$$\mathcal{H} f(\mathbf{r}) = \mathbf{g} \tag{2.22}$$

where  $\mathbf{g}$  is a  $M \times 1$  column vector with  $M$  being the number of pixels on the focal plane array,  $f(\mathbf{r})$  is the three-dimensional object cube, and  $\mathcal{H}$  is the continuous-to-discrete mapping. The reconstruction of the data cube is then described by:

$$\mathbf{H}^\dagger \mathbf{g} = \hat{\mathbf{f}} \quad (2.23)$$

where  $\hat{\mathbf{f}}$  is an  $N \times 1$  vector and where  $N$  is the number of reconstructed voxels in the data cube. From previous discussions we need to use statistics and estimation theory to reconstruct the data cube because of the null components in the system matrix. Therefore, the challenge is to create the discrete-to-discrete system matrix,  $\mathbf{H}$ , from the continuous-to-discrete mapping,  $\mathcal{H}$ . The discrete-to-discrete system matrix,  $\mathbf{H}$ , is developed while calibrating the system.

### 2.5.2. H-MATRIX CONSTRUCTION

The  $\mathbf{H}$ -matrix is developed by sending light from a monochromatic point source through the system and measuring the point response of the CTIS system. By rearranging equation (2.23) to a forward problem,

$$\mathbf{g} = \mathbf{H} \hat{\mathbf{f}}, \quad (2.24)$$

we see that any column of  $\mathbf{H}$  represents the voxel-spread function of the CTIS. This allows us to fill the  $\mathbf{H}$ -matrix one column at a time by having an object that occupies one voxel at a time. Experimentally, we send what is quasi-monochromatic light through the system and measure the response. The CTIS response in the zero diffraction order appears as a point near the center of the

focal plane array. Each of the diffraction orders also consists of a series of spots but the spatial extent of the spots increases as the spectral width of the source increases (Figure 2.6).

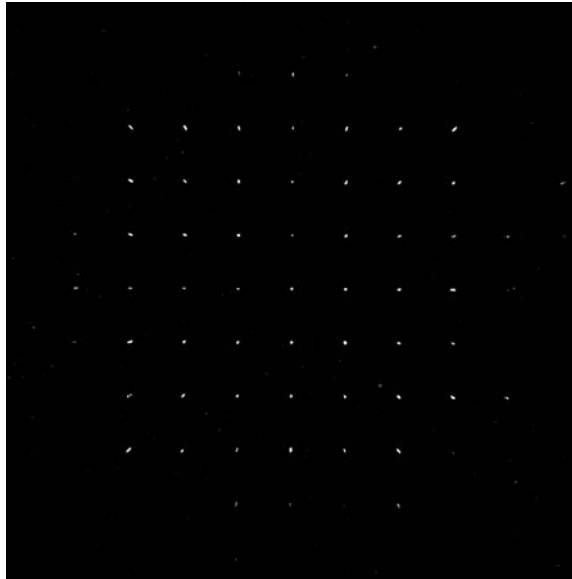


Figure 2.6: CTIS response to a 450 nm near point source.

We then step the quasi-monochromatic source a  $\Delta\lambda$  corresponding to the spectral size of the voxel and repeat. After we have taken images at each spectral step, we have filled all the rows of the  $\mathbf{H}$ -matrix that correspond to the single spatial location. We then assume that the system is spatially shift invariant. This allows us to take the responses of the single spatial location and translate the response to all the other spatial locations in the field stop to fill the remaining rows of the  $\mathbf{H}$ -matrix.

This  $\mathbf{H}$ -matrix construction technique assumes that the system is linear shift invariant. Appendix A discusses the conditions for the linear shift invariant assumption to be valid. From the development in Appendix A, the linear shift invariant assumption is valid as long as the field dependent aberrations are balanced to zero and that:

$$|\mathbf{r} - \mathbf{r}_o|^4 \ll \lambda p^3 \quad (2.25)$$

where  $\mathbf{r}$  is the vector from the optical axis to the off-axis object point,  $\mathbf{r}_o$  is the vector from the optical axis to the radial point in the lens and  $p$  is the distance from the lens to the object as defined in Figure A2.

## 2.6. DATA CUBE

We have stated that the goal of the CTIS system is the reconstruction of the spatially registered spectral content of the scene. We represent the scene reconstruction as a three-dimensional data cube. In our discrete-to-discrete mapping model, the data cube is three-dimensional and discrete. We characterize each discrete location in the data cube as a three-dimensional differential voxel element. Each voxel is indexed by a single number in a lexicographic format corresponding to its  $\mathbf{f}$  vector component. The numerical value in each voxel is a radiometric measurement. The voxel size also corresponds to the spectral and spatial resolution of the system (Figure 2.7). The resolution of

the system, and therefore the voxel size of the data cube, is a function of the optics, the CGH design, the calibration techniques, and the detector array.

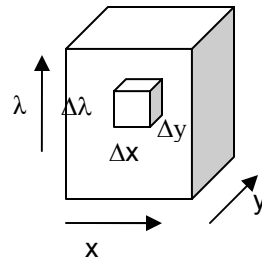


Figure 2.7: Differential voxel element inside the data cube

## 2.7. SPATIAL RESOLUTION

The theoretical spatial resolution of the system can be predicted by examining the system point response at the zero diffraction order. The zero order of the diffraction pattern is a direct polychromatic image of the system field stop. It is the zero order that specifies the spatial extent of the voxel. The spatial extent of the voxel is determined by the spot size of the point source relative to the image size of the field stop. For example, consider a system for which the image of the field stop extends over a 72 x 72 pixel portion of the focal plane. Then let the diffraction limited spot size through the CTIS system subtends a 3 x 3 pixel area on the focal plane. During the  $\mathbf{H}$ -matrix construction where we shift the voxel response function as we fill in the columns, we shift the 3 x 3 voxel spread function to the 24 x 24 locations on the focal plane without overlap. This has the same effect as taking the point source and moving it to the 24 x 24 positions in the field stop where the voxel spread functions do not overlap in the

zero order. The goal then is to design a system where the spatial extent of the point response function completely fills only one pixel in the zero order. If we assume that the detector size is fixed, then we can control the size of the point response function by controlling the size and power of the optics. If we assume that the optics are rotationally symmetric and aberration free, then the diameter of the point spread function is given as:

$$D = 2.44\lambda f/\# \quad (2.26)$$

where  $D$  is the diameter of the Airy disc,  $\lambda$  is the wavelength of the light, and  $f/\#$  is the f-number of the system given as the focal length of the system at the given wavelength divided by the diameter of the entrance pupil.

The size of the point response function may not be the diffraction limit of the system. Recall that the  $\mathbf{H}$ -matrix is formed by sending a monochromatic point source through the system and measuring the voxel spread function. So the point response function is experimentally measured. Experimentally, our point source does have spatial extent. Therefore, to maximize the spatial resolution performance of the system, the calibration procedures used to create the  $\mathbf{H}$ -matrix should create the smallest point source possible to try and achieve the diffraction limit corresponding to an Airy disk diameter smaller than or equal to the diameter of the detector.

## 2.8. SPECTRAL RESOLUTION

Although the zero order gives the most spatial information about the scene, there is little spectral information. The theoretical spectral width of the voxel can be predicted by the displacement of the monochromatic point source at the highest diffraction order. The only spectral information in the zero order is the bandpass of the detector because all of the monochromatic planes of the data cube are co-located. As the light from the field stop is diffracted, the monochromatic planes of the data cube are slightly displaced relative to one another. As the diffraction order is increased, the spatial displacement of the monochromatic planes also increases. The spectral resolution of the system then is the difference of the wavelengths of the two monochromatic planes displaced by a pixel from each other on the detector array. This means that if in the highest diffraction order the point source for a perfect 500 nm falls on the  $i^{\text{th}}$  pixel and 505 nm spot falls on the  $(1+i)^{\text{th}}$  pixel, then the spectral width of the voxel and the spectral resolution of the system is 5 nm. The number of diffraction orders and the diffraction angle is set by the CGH design. Given the diffraction angle from the CGH, the magnification of the system combined with the diffraction angle gives the spatial displacement of the monochromatic planes on the detector array. The mathematical description of the spectral resolution is contained in Chapter 5.

As with the spatial resolution, the calibration procedures influence the spectral resolution as much as the CGH design. The voxel spread function

assumes the calibration source is monochromatic. The reality is that the source has some finite spectral spread. To ensure that the system, not the calibration procedures, is the limiting resolution factor, the spectral spread of the calibration source has to be less than the spectral limitations of the system.

These parameters then set the limits on the spectral width of the calibration source to make the reconstruction limited by the CTIS system parameters instead of the calibration. In the example above, if we can image a smaller spot into the field stop and diffraction limit the spot to the pixel size of the detector array, then we can reduce the voxel spatial size to match. If we use a calibration source with a spectral spread greater than 5 nm, then the spectral width of the voxel will increase to the spectral width of the calibration source because the diffraction spot at the highest diffraction order will exceed the pixel size. Throughout this discussion we have ignored both sub-pixel and sub-voxel effects. In Chapter 4 we will see that sub-voxel sampling can improve system performance.

## **2.9. RADIOMETRIC RESOLUTION**

The numerical value in each voxel of the data cube is a radiometric measurement of the light at the wavelength and spatial location of the voxel. The radiometric resolution is determined by the responsivity, noise, dynamic range, and number of the bits of the detector array. Therefore the radiometric resolution of the system is solely a function of the detector and its electronics. The

radiometric resolution is again determined during the  $\mathbf{H}$ -matrix construction and calibration procedures. The radiometric calibration gives the radiometric strength of the source corresponding to the digital number output of the detector. The radiometric resolution of the system is then the change in radiant flux per digital number. There are two types of calibration, relative and absolute. To get the most precise absolute radiometric measurements of the system, the source used for calibration should be a National Institute of Standards and Technology (NIST) traceable spherical integrating source passed through a monochromator. But, for most applications a relative calibration is sufficient to reconstruct the data cube with relative radiometric strengths. For either case, the critical element is that the source remains stable over the entire length of the calibration process.

## 2.10. ORDER OVERLAP

One of the limitations of the CTIS is that the range of wavelengths is limited to about a single octave. This limitation occurs because where the higher wavelengths of one diffraction order strike the focal plane at the exact same location as the lower wavelength of the next higher order. If we consider the diffraction equation:

$$m\lambda = \text{OPD} \quad (2.27)$$

where  $m$  is the diffraction order number and OPD is the optical path difference between two rays, we see that the diffraction maxima for  $m=2$  and  $\lambda=1 \mu\text{m}$  occurs at the same location in the observation plane as  $m=1$  and  $\lambda=2 \mu\text{m}$ . For

the CGH used in this work, the third order diffraction spots from 400 nm to 470 nm point source at the center of the field stop span the same location on the focal plane as the second order diffraction spots for the entire red spectral region (600-700 nm). If we consider a red light source on the left edge of the field stop and a blue source at the right edge, the order overlap is even more dramatic between the second and third diffraction orders to left side of the zero order. The area circled in Figure 2.8 is the area of order overlap in the visible system. Similar overlap occurs in all diffraction directions.

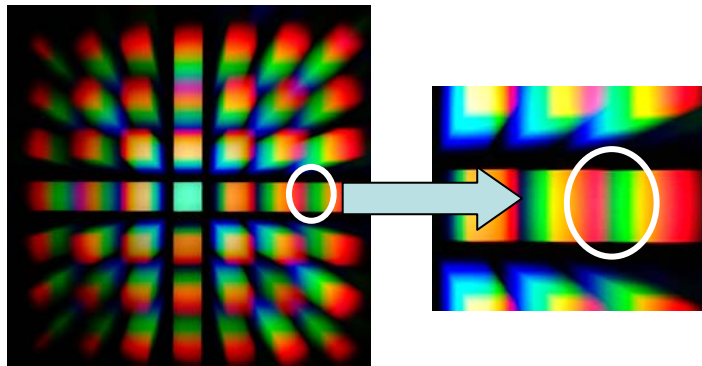


Figure 2.8: Raw image of white light extended source. Circled area shows where the higher wavelength of the second diffraction order overlaps the low wavelengths of the third diffraction order.

A possible solution to overcoming the order overlap issue is to use prisms and filters to split the incoming light into two separate focal planes, each sensitive to a different spectral range of interest. The drawback to this approach is that the spatial co-registration of the two focal planes is difficult at best and would have to be rechecked during operation to insure there is no shift. Now if we have an interest in determining the spectral content of a scene over two separate spectral regions, we must overcome the order overlap and spatial co-registration issues.

## 2.11. DUAL BAND THEORY

It is possible to overcome the order overlap limitation by using an interwoven mixed detector focal plane instead of a focal plane made up of only one detector type. Many standard digital cameras' focal plane arrays consist of the required interwoven mixed detectors in the visible portion of the spectrum. These focal plane arrays consist of predominately silicon detectors with filters that have three spectral bandpasses, red (600-700 nm), green (500-600 nm), and blue (400-500 nm). An interwoven mixed pattern for the detectors is where the detector types alternate between red, green, and blue sensitive pixels (Figure 2.9). If we now group one set of red, green, and blue pixels into a single cluster, we can treat the cluster as a single spatial pixel providing the spectral content of all three bands at that focal plane cluster location. Now we can treat the set of all pixels sensitive to a single band as one focal plane and the pixels sensitive to another spectral band as a second focal plane. These two focal planes are automatically spatially co-registered by the clustering scheme. At the points of order overlap on the focal plane, we can separate the input of the two bands with the proper imaging software and resolve the order overlap issue. The fact that the red pixels are slightly shifted from the blue pixels is accounted for in the calibration procedures described in Chapter 4.



the blue light at the areas where the blue light of one order overlaps the red light of another order and the red pixels pass the red light. In addition to overcoming the order overlap limitation, the mixed detector focal plane allows for co-registration of two or more separate spectral bands.<sup>24</sup>

Integrating a CGH disperser into a commercially available professional digital camera, we can demonstrate a dual band CTIS system as a proof of concept for an extension to a dual band infrared CTIS system. The CGH is designed to operate from about 400 –700 nm. As a part of the proof of concept, we will treat the red and blue bands as the two bands to reconstruct, ignoring the green band.

Infrared focal plane arrays have been developed that detect over two spectral regions at the exact same location on the focal plane instead of interweaving mixed detector types. A detailed discussion of the dual band infrared focal planes is covered in Chapter 5. The advantage of the dual band infrared designs is that a cluster scheme, as used in the color detector arrays, is not needed. Because the detectors sensitive to each band are stacked on top of each other, they are automatically co-located. We will exploit this feature as we design a dual band infrared CTIS system.

## CHAPTER 3

### COMPUTER GENERATED HOLOGRAPHIC DISPERSER

Key to the CTIS system is the dispersive element. The visible system in this research uses a computer generated holographic (CGH) etched phase grating. The CGH for this system was made from poly-methyl methacrylate (PMMA) material etched with an electron beam at JPL. The dispersion of the light is achieved by changing the depth of the PMMA and thus changing the phase of the wavefront at each point. The disperser is composed of numerous unit cells. Each cell consists of an integer number (usually  $8 \times 8$ ,  $10 \times 10$  or  $16 \times 16$ ) of square phasels. Each phasel is etched to a specified depth. The term phasels is used to distinguish the cell etching of the CGH from the detector pixel on the focal plane array and the voxel, which is the three dimensional unit cell of the data cube. The etched depth leads to a phase delay of the transmitted wavefront.

In designing the CGH, we modify the wavefront incident on the CGH to create the desired diffraction pattern on the focal plane. The diffraction pattern becomes the tomographic projections through the data cube discussed in Chapter 2. We design diffraction patterns that create a  $3 \times 3$ ,  $5 \times 5$ , or even a  $7 \times 7$  diffraction pattern on the focal plane. When designing a CGH, we must consider the required spectral and spatial resolution, focal plane characteristics, and the object's characteristics. This chapter will develop the theory behind

designing the CGH etch depth profile and the figures of merit for choosing one etch depth profile over another. In Chapter 5 we will apply the theory of this chapter to design and evaluate a CGH for the dual band infrared CTIS system.

### 3.1. CGH DESIGN ALGORITHM

There are several methods of designing the CGH etch depth profile that include Gerchberg-Saxton,<sup>25</sup> simulated annealing,<sup>26</sup> random search,<sup>27</sup> and genetic iteration.<sup>28</sup> In all of these algorithms the CGH designs are for monochromatic illumination. Using a CGH in an imaging spectrometer requires the design algorithm to design over a substantial range of wavelengths. One such algorithm involves the use of singular valued decomposition.<sup>29</sup>

We start with the phase delay of the light given by:

$$\Phi_{\lambda} = \frac{2\pi d}{\lambda}(n_{\lambda} - 1) \quad (3.1)$$

where  $\lambda$  is the wavelength of the light,  $\Phi_{\lambda}$  is phase delay of the light at the given wavelength,  $n_{\lambda}$  is the wavelength dependent index of refraction of the disperser, and  $d$  is the etch depth of the disperser at each phase.<sup>30</sup> The complex amplitude transmittance of the CGH can be described mathematically as:<sup>31</sup>

$$t(x, y) = A \exp[i\Phi(x, y)] \quad (3.2)$$

where  $\Phi(x, y)$  is the phase of the transmitted wave, at the  $(x, y)$  coordinates in the plane of the CGH from equation (3.1).  $A$  is the amplitude of the electric field.

Now we discretize the CGH and model it as an array of point transmitters by multiplying equation (3.2) by a two-dimensional comb function. In this discrete model the complex amplitude transmittance is given by:

$$t_{mn} = A_{mn} \exp(i\Phi_{mn}) \quad (3.3)$$

where the indexes  $m$  and  $n$  correspond to  $x$  and  $y$  points on the CGH given by the comb sampling function. In this discrete system equation (3.1) then becomes

$$\Phi_{\lambda,mn} = \frac{2\pi d_{mn}}{\lambda} (n_{\lambda} - 1). \quad (3.4)$$

where  $d_{mn}$  is the etch depth at the  $m, n$  phase.  $\Phi_{\lambda,mn}$  and  $n_{\lambda}$  keep the wavelength subscripts to emphasize their wavelength dependence. We can calculate the electric field complex amplitude at the image plane by using the Fraunhofer diffraction model.

To facilitate the computer design of the system, we will model the system as a point-to-point mapping; which is to say we will map the complex amplitude transmittance of the CGH as a two-dimensional collection of evenly distributed points given by equation (3.3) to a collection of two-dimensional evenly spaced points representing the complex amplitude of the electric field incident on the pixels of the focal plane. This model allows us to square the complex amplitude at each point to model the output of an array of digital detectors. This discrete-to-discrete modeling allows us to use the two-dimensional discrete Fourier transform. So, by taking the discrete Fourier transform of the complex amplitude

transmittance of the CGH, we find the complex amplitude of the field at the focal plane array is:

$$u_{kl} \propto \sum_{m,n} A_{mn} \exp\left[i \frac{2\pi d_{mn}}{\lambda} (n_{\lambda} - 1)\right] \exp[-i2\pi(mk + nl)/N] \quad (3.5)$$

where the subscripts  $k$  and  $l$  correspond to a two-dimensional discrete location on the focal plane and the subscripts  $m$  and  $n$  are the discrete locations on the CGH.

Unfortunately, equation (3.5) does not give a simple linear relation between the phase profile of the CGH and the complex amplitude on the focal plane; therefore, we employ the calculus of variations. Calculus of variation involves finding the function of a functional for which changes in the function result in a stationary, or small changes, in the functional. In our case, the complex amplitude at the FPA is the functional for which the phase profile,  $\Phi$ , is the function we vary. To employ the calculus of variations in this problem, let us consider a differential change in the phase profile of the CGH and look at the change in the field at the FPA with the goal of finding the point where the differential change in the field is small.<sup>32</sup> During the manufacturing process, we do not specify the phase, but instead manufacture an etch depth profile. We substitute equation (3.4) into equation (3.5) and look at the differential change in the field due to a differential change in the etch depth. We take the partial derivative of both sides of equation (3.5) with respect to  $d$ :

$$\frac{\partial}{\partial d} u_{kl} \propto \frac{\partial}{\partial d} \left\{ \sum_{m,n} A_{mn} \exp \left[ i \frac{2\pi d_{mn}}{\lambda} (n_{\lambda} - 1) \right] \exp \left[ -i 2\pi (mk + nl) / N \right] \right\}. \quad (3.6)$$

We can rewrite the differential as:

$$\Delta u_{kl} \propto \sum_{m,n} i \frac{2\pi}{\lambda} (n_{\lambda} - 1) A_{mn} \exp \left[ i \frac{2\pi d_{mn}}{\lambda} (n_{\lambda} - 1) \right] \exp \left[ -i 2\pi (mk + nl) / N \right] \Delta d_{mn} \quad (3.7)$$

where  $\Delta u_{kl}$  is the differential change in the field due to the differential change in the etch depth  $\Delta d_{mn}$ . Now we do have a linear relationship between the changes in the complex amplitude due to a change in the etch depth.

$$\Delta u_{kl} \propto \sum_{m,n} S_{(d):kl,mn} \Delta d_{mn} \quad (3.8)$$

where:

$$S_{(d):kl,mn} = i A_{mn} \exp \left[ i \frac{2\pi d_{mn}}{\lambda} (n_{\lambda} - 1) \right] \exp \left[ -i 2\pi (mk + nl) / N \right]. \quad (3.9)$$

$S_{(d):kl,mn}$  is a component of the sensitivity matrix. The  $(d)$  subscript shows that the sensitivity matrix depends on the current etch depth distribution of the CGH.

Now we can rasterize  $\Delta u_{kl}$  and  $\Delta d_{mn}$  into column vectors and the sensitivity matrix will be a two-dimensional array that relates the strength of the change of the complex amplitude field distribution due to a small change in the CGH etch depth profile:

$$\Delta \mathbf{u} = \mathbf{S} \Delta \mathbf{d}. \quad (3.10)$$

Equation (3.10) has a form for which we can implement an iterative algorithm that will allow us to specify the etch depth profile that will meet our design objectives. First, we specify the desired design field distribution  $\mathbf{u}_{\text{goal}}$ .

Next, we generate a random etch depth pattern,  $\mathbf{d}_{\text{int}}$ , and use equation (3.5) to calculate  $\mathbf{u}_{\text{int}}$ . Now we add a small change in the etch depth profile,

$$\mathbf{d}_{\Delta} = \mathbf{d}_{\text{int}} + \Delta \mathbf{d}, \quad (3.11)$$

and calculate the resulting field,  $\mathbf{u}_{\Delta}$ . By rewriting equation (3.10) and substituting equation (3.11) we can solve for the sensitivity matrix,  $\mathbf{S}$ .

$$\mathbf{S} = (\mathbf{u}_{\Delta} - \mathbf{u}_{\text{int}}) \Delta \mathbf{d}^{-1} \quad (3.12)$$

We choose to use this form of  $\mathbf{S}$  instead of the form found in equation (3.9) because we are going to invert  $\mathbf{S}$  to solve for a new etch depth profile and iterate until we get a stable solution to the etch depth profile. If we were to use equation (3.9), we would get oscillations around a solution and may never converge to an optimal solution. By using a small enough  $\Delta \mathbf{d}$ , we will “sneak-up” on a solution and converge much quicker.

Once we have  $\mathbf{S}$ , we must invert it. But,  $\mathbf{S}$  is a non-square singular matrix, so a direct inverse does not exist. Therefore, we use the Moore-Penrose Pseudoinverse. To find the pseudoinverse, we decompose the sensitivity matrix

$$\mathbf{S} = \mathbf{U} \mathbf{W} \mathbf{V}^t. \quad (3.13)$$

The matrix  $\mathbf{V}$  contains the column-oriented object space singular vectors, or phase-perturbation vectors. The matrix  $\mathbf{W}$  is a diagonal matrix consisting of the singular values  $w_n$  and the  $\mathbf{U}$  matrix contains the corresponding column-oriented

image space singular vectors, or diffraction-order amplitude-variation vectors.

The pseudoinverse then becomes:

$$\mathbf{S}^+ = \mathbf{V}\tilde{\mathbf{W}}^{-1}\mathbf{U}^t = \sum_{n=1}^R \frac{1}{w_n} \mathbf{v}_n \mathbf{u}_n^t. \quad (3.14)$$

The inverse of any zero-valued singular values are set to zero in  $\tilde{\mathbf{W}}^{-1}$ . This change is reflected in the use of the rank as the upper limit of the sum and is the number of non-zero singular values. The pseudoinverse yields the least-squares solution to the inverse of the discrete-to-discrete mapping.

We can solve for a new etch depth profile by using:

$$\mathbf{d}_{\text{next}} = \mathbf{H}^+(\mathbf{u}_{\text{goal}} - \mathbf{u}_{\text{int}}) + \mathbf{d}_{\text{int}} \quad (3.15)$$

We set  $\mathbf{d}_{\text{int}} = \mathbf{d}_{\text{next}}$  and repeat the process, continuing until the difference between  $\mathbf{d}_{\text{next}}$  and  $\mathbf{d}_{\text{int}}$  is small enough.

This method finds a local solution. To improve on the solution, we can repeat the process with a different random starting etch depth profile and compare the results between the two iterations. Methods to test and compare CGH designs are addressed later in this chapter.

Past algorithms have been designed to phase. If the index of refraction of the material used to manufacture the CGH is constant over the spectral region of interest, then the numerator in equation (3.4) can be treated as a single variable, and it can be used as the variable that is changed in the SVD algorithm.

Therefore, instead of designing to etch depth profile, we are designing to a phase depth. The phase depth is converted to an etch depth by using a reference

wavelength near the center of the spectrum for which the CGH is designed. Designing directly to etch depth allows the CGH to be manufactured with dispersive materials and allows the CGH to operate over a larger spectral region by not using the reference wavelength to convert the phase profile to an etch depth profile.

### 3.2. RECTANGULAR PHASELS

So far we have assumed that the CGH is just a series of point transmitters and the focal plane is also a series of points. The CGH is more accurately modeled as a series of rectangle functions, each centered on the array of points we defined above. Therefore, the more complete model of the complex amplitude transmittance of the CGH becomes:

$$t(x_1, y_1) \propto \sum_{m,n=0}^{q-1} \exp(i\Phi_{mn}) \text{rect}\left(\frac{x_1 - mx_c}{x_c}\right) \text{rect}\left(\frac{y_1 - ny_c}{y_c}\right) ** \sum_{k,l=-\infty}^{\infty} \delta\left(\frac{x_1 - kqx_c}{qx_c}\right) \delta\left(\frac{y_1 - lqy_c}{qy_c}\right) \quad (3.16)$$

where  $(x_c, y_c)$  are the real width and height of each phasel, and the \*\* operator indicates the two-dimensional convolution. The index,  $q$ , is the number of phasels in the unit cell.

The complex amplitude is then given by the Fourier transform of the transmittance equation and substituting the reduce coordinates for the transform variables:  $\xi=x/\lambda f$  and  $\eta=y/\lambda f$  in the continuous case. This gives us

$$u(x, y) \propto \sum_{m,n=0}^{q-1} \exp(i\Phi_{mn}) \exp\left[-i \frac{2\pi}{\lambda f} (mx_c x + ny_c y)\right] \times \sum_{k,l=-\infty}^{\infty} \delta\left(x - \frac{k\lambda f}{qx_c}\right) \delta\left(y - \frac{l\lambda f}{qy_c}\right) \times \text{sinc}\left(\frac{x_c x}{\lambda f}\right) \text{sinc}\left(\frac{y_c y}{\lambda f}\right) \quad (3.17)$$

where  $f$  is the focal length of the re-imaging lens. For the Fraunhofer diffraction model used here to be valid, the size of the phasel must be larger than the wavelength of light. From equation (3.17), we see that the size of the point response function of the CGH is given by the ratios inside the sinc function and are functions of the size of the CGH cell, the wavelength of the light, and the focal length of the imaging lens. The indexes  $k$  and  $l$  denote the diffraction order. There are an infinite number of diffraction orders, but the sinc envelope makes the higher orders near zero and the orders higher than the ones of interest extend outside the focal plane. The delta functions show how the light is dispersed and that the dispersion is a function of wavelength, imaging focal length, CGH cell size, and the diffraction order.

### 3.3. ETCH DEPTH QUANTIZATION

In addition to ignoring the extent of the phasel size, we have also failed to address the impact of the manufacturing process that limits the etch depth profile to a set of discrete etch depths. Up until now we have assumed that the etch depth can have a continuous value between zero and an arbitrary maximum

depth. The real CGH is composed of quantized etch depths from zero to a maximum depth. To determine the effects of this etch depth quantization, we begin with the complex amplitude transmittance of the CGH. Given the complex amplitude transmittance in the CGH plane is  $u(x,y)$ , as given in equation (3.5), the Fourier spectrum of the field is:

$$U(\xi, \eta) = A(\xi, \eta) \exp[i\Phi(\xi, \eta)] \quad (3.18)$$

where  $\Phi(\xi, \eta)$  incorporates the design phase profile at a given wavelength. We will assume that there is a point wise relation between the design phase,  $\Phi$ , and the manufactured phase,  $\varphi$ , where the manufactured phase becomes a function of the design phase,  $\varphi = \varphi(\Phi)$ . If the manufactured phase exactly matches the design manufactured phase, then a graph of  $\varphi$  verses  $\Phi$  would result in a straight line at a forty-five degree angle with the  $\Phi$  axis. When the etch depths are quantized to a discrete set, then the graph of  $\varphi$  vs  $\Phi$  has a stair step appearance (Figure 3.1).

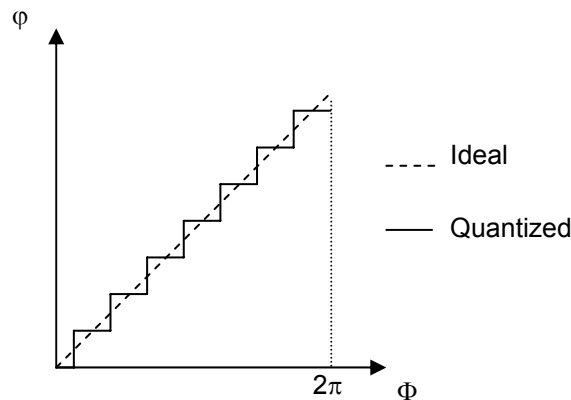


Figure 3.1: Graph of quantization of etch depth on manufactured vs ideal case

We can expand the manufactured phase function in a Fourier series:

$$\exp(i\varphi) = \sum_{m=-\infty}^{\infty} c_m \exp(im\Phi). \quad (3.19)$$

The Fourier coefficients are given by:

$$c_m = \frac{1}{2\pi} \int_0^{2\pi} \exp[i\varphi(\Phi)] \exp(-im\Phi) d\Phi. \quad (3.20)$$

Now we can rewrite the Fourier spectrum complex amplitude of the manufactured CGH as:

$$A \exp(i\varphi) = \sum_{m=-\infty}^{\infty} c_m [A \exp(im\Phi)]. \quad (3.21)$$

Any function of  $\varphi$ , which is in turn a function of  $\Phi$ , will be periodic in  $\Phi$  and piecewise constant over the same intervals of  $\varphi$  on which  $\Phi$  is constant. From the piecewise constancy we can say:

$$\exp(i\varphi) = \sum_{k=-\infty}^{\infty} \exp\left(\frac{2\pi ik}{N}\right) \text{rect}\left(\frac{\Phi}{2\pi/N} - k\right) \quad (3.22)$$

where  $N$  is the number of discrete etch depths. From equation (3.20) the Fourier coefficients are:

$$c_m = \frac{1}{2\pi} \int_0^{2\pi} \sum_{k=-\infty}^{\infty} \exp\left(\frac{2\pi ik}{N}\right) \text{rect}\left(\frac{\Phi}{2\pi/N} - k\right) \exp(-im\Phi) d\Phi. \quad (3.23)$$

We start by solving the integral portion of equation (3.23) and we have:

$$\begin{aligned}
\int_{-\frac{1}{\pi/N}}^{\frac{1}{\pi/N}} \text{rect}\left(\frac{\Phi}{2\pi/N} - k\right) \exp(-im\Phi) d\Phi &= \int_{-\infty}^{\infty} \text{rect}\left(\frac{\Phi}{2\pi/N} - k\right) \exp(-im\Phi) d\Phi \\
&= \frac{2\pi}{N} \text{sinc}\left(\frac{m}{N}\right) \exp\left[-i2\pi\left(\frac{mk}{N}\right)\right].
\end{aligned} \tag{3.24}$$

Then we have:

$$\begin{aligned}
c_m &= \frac{1}{2\pi} \sum_{k=-\infty}^{\infty} \exp\left(\frac{i2\pi k}{N}\right) \left(\frac{2\pi}{N}\right) \text{sinc}\left(\frac{m}{N}\right) \exp\left[-i2\pi\left(\frac{mk}{N}\right)\right], \\
c_m &= \text{sinc}\left(\frac{m}{N}\right) \sum_k \frac{1}{N} \exp\left[i2\pi\left(\frac{1-m}{N}\right)k\right].
\end{aligned} \tag{3.25}$$

The summation portion of equation (3.25) is zero except when  $m=1, 1+N, 1+2N, \dots, 1+nN$  for which it is unity. Now we substitute  $m=1+nN$  into equation (3.25), execute the sum. Substitute the Fourier coefficient back into equation (3.21), and we have:

$$A \exp(i\varphi) = A \sum_{n=-\infty}^{\infty} \text{sinc}\left(\frac{1}{N} + n\right) \exp[i(1+nN)\Phi]. \tag{3.26}$$

Equation (3.26) is the complex amplitude on the focal plane due to the phase quantization of the CGH,  $\hat{U}$ . To understand the results of equation (3.26), we will separate the  $n=0$  term from the rest of the sum:

$$\hat{U} = A \exp(i\varphi) = A \text{sinc}\left(\frac{1}{N}\right) \exp(i\Phi) + \sum_{n \neq 0} A \text{sinc}\left(n + \frac{1}{N}\right) \exp[i(nN+1)\Phi]. \tag{3.27}$$

From equation (3.27) we observe two related effects. The first is that the amplitude of the desired complex amplitude as specified in equation (3.18) is

reduced by the  $\text{sinc}(1/N)$ . The related effect is that the portion of the complex amplitude contained in the sum of terms can be treated as noise. As an example, if there are 16 evenly spaced quantized etch depths available during the CGH manufacturing process, then the desired complex amplitude is reduced to 99.36% of the desired complex amplitude and 98.72% of the irradiance. Therefore, when we design a CTIS system, we must account for the lost of signal and the increase of noise due to etch depth quantization.<sup>33</sup>

### **3.4. DESIGN EVALUATION**

Now that we have developed an algorithm to design the CGH, we must specify figures of merit to allow us to test and compare designs. We will use three metrics to compare designs, the average diffraction efficiency of each diffraction order averaged over all wavelengths, the total efficiency of the CGH, and the root mean squared of the difference between the diffraction efficiency of each order with the average diffraction efficiency. There are two reasons to compare designs. First, because each design starts with a random etch depth pattern, each time the design algorithm is run, we get a slightly different etch depth profile. Therefore, we need a way to pick which algorithm run gives the best results. In addition to different design results based on the different random start profiles, we also have several different design parameters that include design patterns and the number of phasels in a unit cell. We will discuss the different design patterns considered in this work in Chapter 5. There are three

different unit cell sizes, 8 x 8, 10 x 10, and 16 x 16 phasels per unit cell. The three cell sizes are chosen because the design software is already written for those sizes. Therefore, we must not only pick the best design after several algorithm runs but also pick the best design parameters for the system.

Each of the figures of merit addresses a performance parameter of the CTIS system. The average diffraction efficiency of each diffraction order is important because it will be used to determine the minimum irradiance the system can measure. To calculate the diffraction efficiency of each diffraction order, we first take the Fourier transform of the complex amplitude transmittance of a single CGH unit cell at equally spaced wavelengths within the spectral bands of interest and then take the absolute value squared. The result of the Fourier transform is the expected complex amplitude on the focal plane when the CGH is illuminated by a monochromatic plane wave and the absolute value squared gives the irradiance. We see a set of diffraction points on the focal plane. The diffraction efficiency is calculated by dividing the value of the intensity in the diffraction order of interest by the sum of all intensities on the focal plane. We do this calculation for all of the diffraction orders we want in the design and average them. Then we average the average over all wavelengths. The result is a value that will serve as a screening value for a design. For example, if the average diffraction efficiency per order is one percent and one percent of the incident irradiance on the focal plane is below the noise level, then we need to use a different CGH design.

The total efficiency of the CGH is best used to compare consecutive runs using the same design parameters. The total efficiency of the CGH is calculated by summing the diffraction efficiencies of the diffraction orders of interest at each wavelength and then averaging over all wavelengths. This figure of merit gives a measurement of the amount of usable light. The difference between the total efficiency and the average diffraction efficiency is that the total efficiency takes into account that different goal patterns will have different numbers of diffraction orders. A 5 x 5 diffraction pattern with 25 diffraction orders will have a lower average diffraction efficiency than a 3 x 3 diffraction pattern yet may have a much higher total efficiency. Therefore, the total efficiency and average diffraction order efficiency measure different parameters.

The third figure of merit is used to measure how uniformly the light is distributed among the diffraction orders of interest. The goal is that each diffraction order has the same diffraction efficiency. There are two reasons for this. The first is that if one order is much stronger than another, the stronger order may saturate before the weaker order gets above the noise. The second reason we want uniform diffraction efficiencies across all orders is that one strong order can skew the reconstruction of the data cube unless we know the relative strength of each order and account for them in the reconstruction algorithms.

To measure the uniformity of the diffraction orders, we will use the root mean squared of the difference between the diffraction efficiency of each order

with the average diffraction efficiency. At each wavelength we calculate the average diffraction efficiency of all the diffraction orders in our design pattern. We then sum the square the differences between each order and average. Finally, we average that value over all wavelengths. In the end, we get an average RMS deviation from the average diffraction efficiency at a particular wavelength. The CGH with the lower the value has a more uniform diffraction efficiency.

In Chapter 5 we describe the design process for the dual-band infrared CTIS. We apply these figures of merit to the CGHs designed for that system and use them with other design criteria to optimize the system.

## **CHAPTER 4**

### **DUAL BAND VISIBLE CTIS PROOF OF CONCEPT**

The first research objective for this work is to use a three band, commercially available camera system to demonstrate the feasibility of a dual visible spectral band hyperspectral imaging spectrometer. To achieve this objective, we integrated a professional grade color digital camera with a CGH disperser to create a CTIS system. We calibrated the system and took several test images to determine how well we can reconstruct the test scene in the blue and red spectral regions.

#### **4.1. PROOF OF CONCEPT**

To demonstrate the viability of the dual band system, we conducted two experiments. The first was designed to demonstrate that the reconstructions of two data cubes are spatially co-registered and to determine the spatial resolution of the system. The second experiment was designed to determine the spectral resolution of the system in both spectral bands.

To demonstrate the spatial co-registration of two data cubes in different spectral regions, we will use a digital camera with interwoven pixels sensitive to the red, green, and blue spectral bands, as described in Chapter 2. We can then use the clustering scheme to separate the co-registered output of the bands. After reconstructing the data cubes using MART and / or EM, we can determine

the location of spatial features present in both spectral bands and compare their locations in each data cube. If the dual band CTIS system is viable, we will find the feature in the same spatial location of both data cubes. In addition to verifying that both data cubes are spatially co-registered, we will also check the spatial resolution of the system. Based on the discussion in Chapter 2, we would only expect to resolve spatial features that are larger than the spatial extent of the voxel spread function in the zero order.

To test the spatial characteristic of the dual-band system, we will use evenly spaced black and white vertical bars and evenly spaced blue and red vertical bars as the objects to reconstruct. If the data cubes are co-registered, we should find the edges of the bars at the same location in both data cubes. To determine if the spatial resolution is at least as good as the voxel spread function, we will use bars of different widths and determine at which width we can resolve the bars.

To test the spectral characteristics of the system, we will reconstruct objects with a known spectral signature and compare the known spectral signature with the reconstructed signature. By using a laser line and a known light emitting diode, we can reconstruct the spectral signatures and compare the reconstructed spectral signatures with the measured spectral signatures.

## 4.2. EXPERIMENTAL SET-UP

The camera used in this proof-of-concept is a Fuji FinePix S1 Pro digital camera (Figure 4.1). The objective lens is a Nikkor 35-70 f/2.6D macro zoom lens. The collimating and imaging lenses are Nikkor 70-300 mm f/4-5.6D ED lenses. The CGH is a 7 x 7 disperser designed for 440 - 740 nm with a 0.75 inch clear aperture. The field stop is 5 mm square. The camera has several output formats to choose from and include JPEG, TIFF-RGB or TIFF-YC. The camera also allows us to choose the number of output pixels for each band. The three choices are 3040 x 2016, 2304 x 1536, or 1440 x 960. The focal plane array is a 23.3 x 15.6 mm first generation Super CCD with 3.4 million color filtered detectors in an interwoven pattern. The A/D conversion is 8-bit. The shutter speed can vary in non-uniform discrete steps between 1/2000 to 30 seconds.

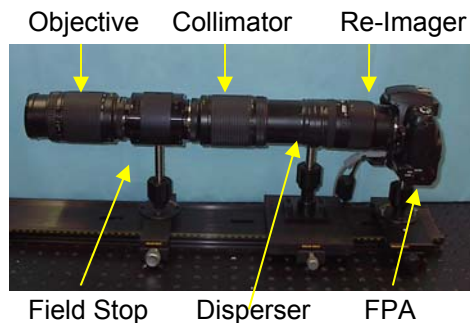


Figure 4.1: Image of dual band visible CTIS

For this work we choose TIFF-RGB in the 3040 x 2016 output format. We choose the TIFF format over the JPEG format because there is less data

compression with TIFF formats over JPEG. We choose the TIFF-RGB format over the TIFF-YC because the TIFF-RGB format output consists of three two-dimensional arrays corresponding in general to the red, green, and blue regions of the visible spectrum. The bandpass of each color region was measured by sending monochromatic light into the system and measuring the percentage of the light in each color region to the total light incident on the focal plane (Figure 4.2).

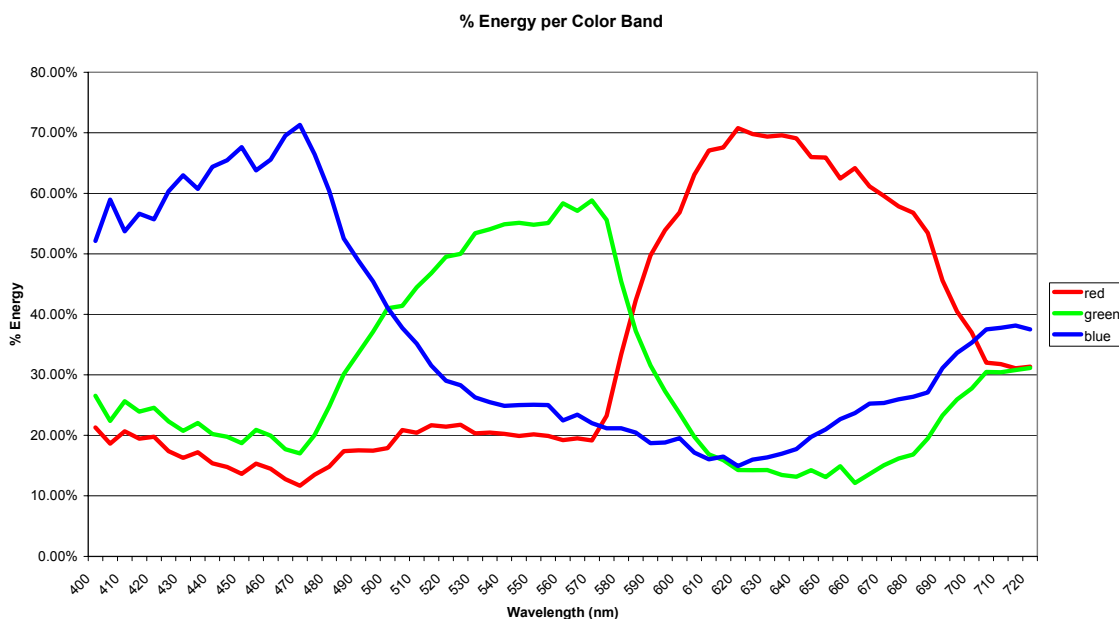


Figure 4.2: Energy distribution by band for each wavelength

The camera image processing provides more output pixels than there are detectors. The actual image processing software that maps the detector output to the TIFF output is proprietary to Fuji. The greater number of output pixels compared to the number of detectors implies that there is some type averaging

or mixing of the detector outputs to create the output arrays. We will model the system output as the actual focal plane array output. We assume that the DN in the  $m,n$  position of the red output array corresponds to the irradiance measured at a red sensitive detector at the  $m,n$  location of the detector array. Similarly the DN in the  $m,n$  position of the blue detector corresponds to the irradiance measured at the blue sensitive detector at the  $m,n$  location on the detector. This assumption supports the clustering scheme described in Chapter 2. The assumption was tested by sending a white light point source into the system and comparing the location of response in each of the red, green, and blue arrays. We found that the white light point source was in exactly the same location and had the same spatial extent in all three arrays. We will test this assumption again when we look at the spatial resolution of the system.

The calibration source is a 250 Watt halogen photo optic lamp bulb powered by a 10.4 volt power supply. The light from the source is passed into a Triax 190 monochromator and reflected off a 1198 grooves/mm blazed grating at 500 nm. The output of the monochromator is passed through a microscope objective and coupled into a 50  $\mu\text{m}$  optical fiber.

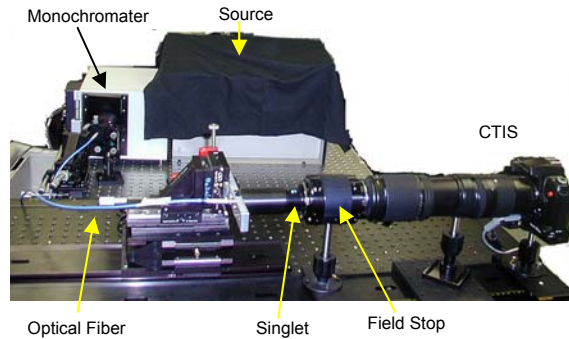


Figure 4.3 CTIS calibration set-up

The first object was a series of black and white bars. Half of the black and white bars were 6.75 mm wide while the other halves were 4.75 mm wide. The second object was the alternating red and blue bars that were the same size as the black and white. The field stop subtended an area of 105 x 105 pixels on the focal plane. In object space that same area was 16.2 x 16.2 cm. Therefore, each pixel subtended an area 1.54 mm<sup>2</sup> in object space. Then, based on the discussion in Chapter 2, we can create Table 4.1 which shows the object size we can resolve based on the voxel spatial extent.

Voxel extent (pixels)	Object extent (mm)
1 x 1	1.54 x 1.54
2 x 2	3.08 x 3.08
3 x 3	4.62 x 4.62
4 x 4	6.08 x 6.08
5 x 5	7.7 x 7.7
6 x 6	9.24 x 9.24
7 x 7	10.78 x 10.78
8 x 8	12.32 x 12.32
9 x 9	13.86 x 13.86

Table 4.1: Relation between voxel and object extent

Then we would expect that to resolve the larger bars we would need for the voxel extent to be  $5 \times 5$  or less and  $2 \times 2$  or less for the small bars.

For the spectral resolution, we must consider the spectral width of the object and the dispersion of the highest diffraction order. In Chapter 2 we saw that the spectral resolution is limited by the spectral line width of the calibration source and the change in wavelength over a single pixel at the highest diffraction order. The full-width half max of the calibration source in this system is about 5 nm (Appendix C). Examining the displacement of the spots on the outer order of the calibration images, we find that a 5 nm change in the source wavelength corresponds to the center of the spot moving about 5 pixels. Then, we can conclude that the limiting factor on the spectral resolution will be the spectral width of the calibration source. Now, based on the full-width half max of the source, we choose to step the wavelength of the calibration source at 5 nm. To verify the spectral resolution, we will reconstruct a laser spot and examine the spectral signature. We would expect to be able to reconstruct the laser line to about 5 nm.

### **4.3. CALIBRATION PROCEDURES**

As discussed in Chapter 2, the calibration procedures are critical to specifying the spatial and spectral resolution of the CTIS system as well as forming the  $\mathbf{H}$  matrix. The calibration procedures also are the source of most of the errors.

The first step of the calibration procedures is to determine the location of the zero order diffraction pattern on the focal plane and align the optics. Failure to properly align the CGH and the optics results in introducing errors in the reconstruction routine. The errors come from the  $\mathbf{H}$  matrix construction algorithm that assumes that the CGH and field stop are aligned so that the edges align vertically and horizontally with the focal plane. To achieve and verify the alignment, we illuminate a white screen with a broadband white light source without the objective lens. We repeatedly take an image and rotate the stop until the bottom edge of the zero order image of the field stop lies along a row of detectors and the vertical edge lies along a single column. Then, we place a white light near-point source in the field stop and rotate the CGH until the diffraction of the horizontal orders lie along the same row of detectors and the diffraction of the vertical orders lie along the same column of detectors.

Once we align the system, we then characterize the source. Critical to the process is balancing the spectral width of the light coupled into the fiber with the maximum amount of light. The narrower the spectral width the less total light passes through the system. We adjust the microscope objective, optical fiber and monochromator slit width to an acceptable spectral width with maximum throughput. Once the system throughput is a maximum, we measure the spectral line width using an Ocean Optics spectrometer, and we measure the strength of the light with a radiometer.

Next, we image the end of the fiber optic into the field stop. The goal is to have the image of the fiber optic in the field stop as close to a point source as possible. To achieve this goal, we image the end of the fiber optic through a 10 mm focal length singlet to the field stop. Placing the fiber optic and singlet structure on an x, y, z translation stage allows us to place the image of the fiber in the center of the field stop and at the minimum circle focus for the center wavelength of the red spectral region and for the center wavelength of the blue spectral region.

Now that the system is completely aligned, we are prepared to begin taking calibration images (Figure 4.4). We set the output of the monochromator to the calibration wavelength and acquire an image. We read the maximum digital number (DN) output of the camera and adjust the integration time until the output is a maximum without saturating. In the case for this 8-bit system, the maximum DN has to be between 230 and 254. We then take five consecutive images at that integration time and follow with five dark images at the same integration time. We step to the next wavelength and repeat. The wavelengths used in this calibration are from 400 – 500 nm in 5 nm steps and from 600 – 675 nm in 5 nm steps. We stop at 675 nm instead of 700 nm because we can not get enough signal to overcome the noise at the long integration time required. Because the available camera integration time steps are non-uniform, there are several wavelengths where the maximum DNs are outside the 230 to 254 range.

In those cases, we take the longer integration time to insure the calibration signal overcomes the noise in nearly all diffraction orders with minimum saturation.

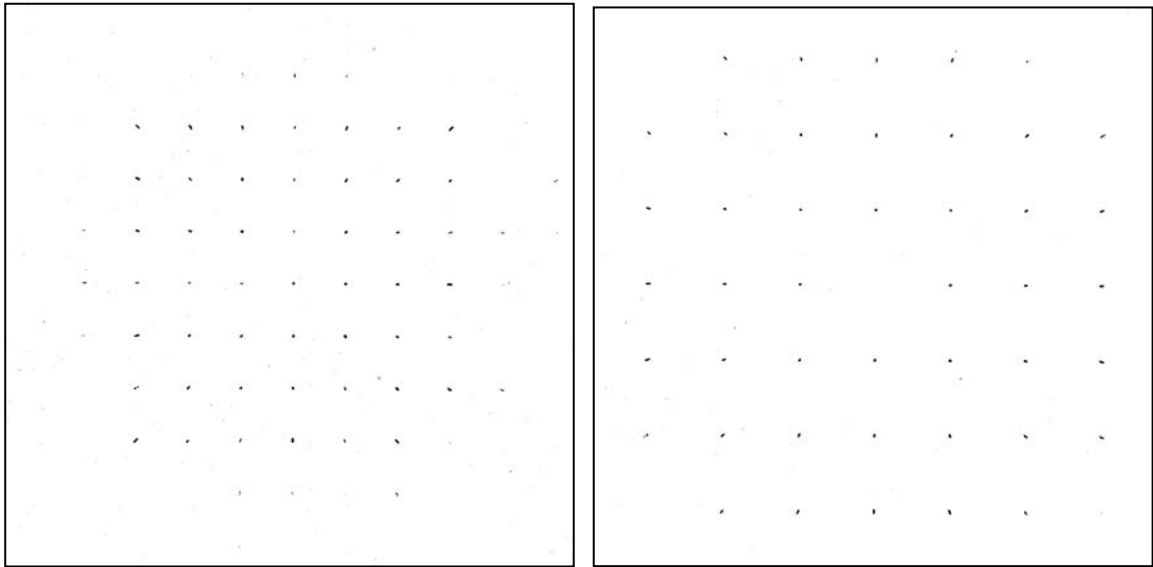


Figure 4.4. Negative calibration images at 450 nm (left) and 650 nm (right) after dark image subtraction and thresholding.

Once we take the five light images and five dark images at each wavelength of interest, we begin the processing of the images in preparation for **H**-matrix construction. To process the images, we first separate the light and dark images into the red, and blue output bands. We only keep the band that contains the wavelength of the calibration source. We average the light images and the dark images separately, then subtract the average dark images from the average light images. This five image average and dark image subtraction is designed to reduce the noise in the calibration images.

## **4.4. RESULTS**

Once the calibration is complete, we immediately acquired the images of the test objects. After acquiring all the calibration images and test images, we use the processed calibration images to create an **H**-matrix for both the red and blue data cubes. We then process the test images by separating the output bands and subtract a dark image average at the same integration time as the test image. We then reconstruct the test objects and compare the reconstructed data cubes to our predictions.

### **4.4.1. SPATIAL RESULTS**

The first object is a series of alternating black and white vertical bars (Figure 4.5). The white bars are 6.75 mm wide and separated by 6.75 mm for half the object and 4.75 mm wide separated by 4.75 mm for the other half of the object. The second object is the same except the bars are alternating red and blue. The objects are illuminated by a 75 watt white light bulb. These objects demonstrate how the spectral content of objects with components in both spectral bands of interest can be separated. The red and blue bars demonstrate the separability of objects with spectral components in only one band while the black and white bars demonstrate separability of objects with spectral components in both bands. We can determine the spatial resolution of the system by examining the reconstruction of the object along a horizontal line. We can also check the spatial co-location of the bands by identifying the location of

peaks in both bands. For the black and white bars we expect that the maximums occur in the same locations for both bands. For the blue and red bars we expect that the maximum in the blue band will fall in the minimum of the red band and vice versa.

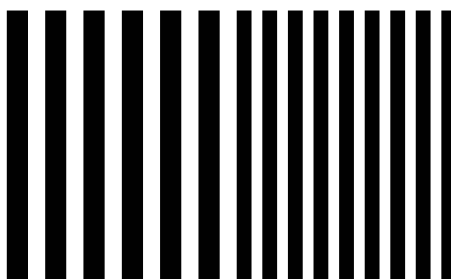


Figure 4.5: White and black bar object illuminated by 75 watt white light bulb

Figures 4.6 a-d show graphs with cuts in the data cube reconstructions of the object in Figure 4.5 in both the red and blue bands. The graphs are the relative radiometric measure along a constant  $y$  pixel at a given wavelength along the  $x$  direction. The complete set of graphs along the same constant  $y$  pixel at all sampled wavelengths is contained in Appendix C. From the graphs we can draw two conclusions. The first is that the two data cubes are co-registered to within  $\pm 2$  pixels, which is within the uncertainty of the zero order spot size. The second conclusion is that the spatial resolution of the system is better than predicted by the spot size.

The spatial co-registration conclusion is based on examining the locations of the peaks between the red and blue data cubes. In Figures 4.6 a and b, the third maximum from the right in the blue bands occurs at pixel 22. In the red

bands that peak occurs at pixel 20. In the data cubes reconstructing the red and blue bars, we expect the peaks in the blue bands to correspond to the valleys in the red band. In Figures 4.6 c and d, pixel 20 is a valley in the blue band and a peak in the red band. Combining these findings with the fact that the image of the white light point source in the zero diffraction order used during calibration is at the same x, y pixel location on the focal plane in both bands strengthens the conclusion that the system produces co-registered data cubes in both bands.

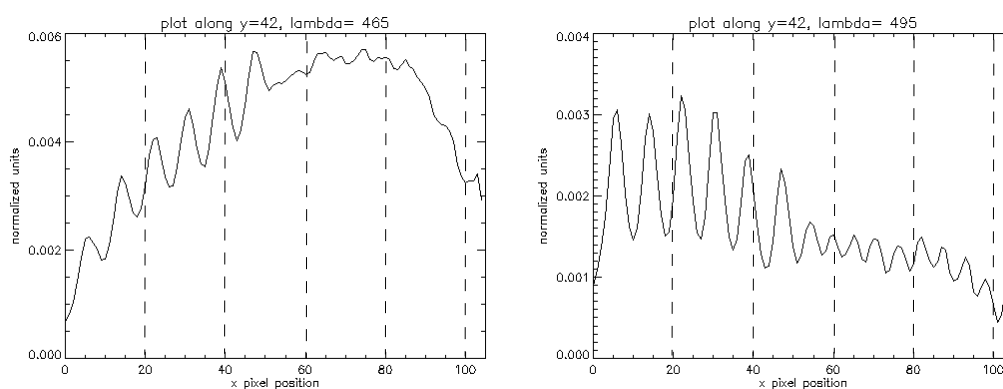


Figure 4.6a: Cut along y-pixels in white bar of blue data cube

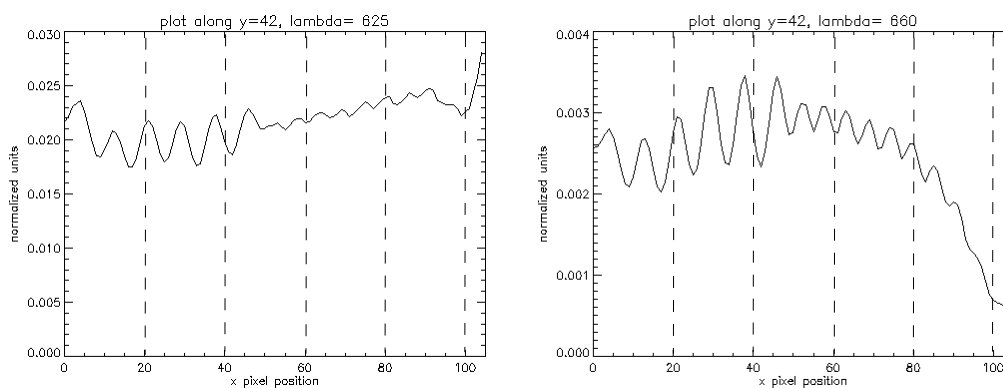


Figure 4.6b: Cut along y-pixels in white bars of red data cube

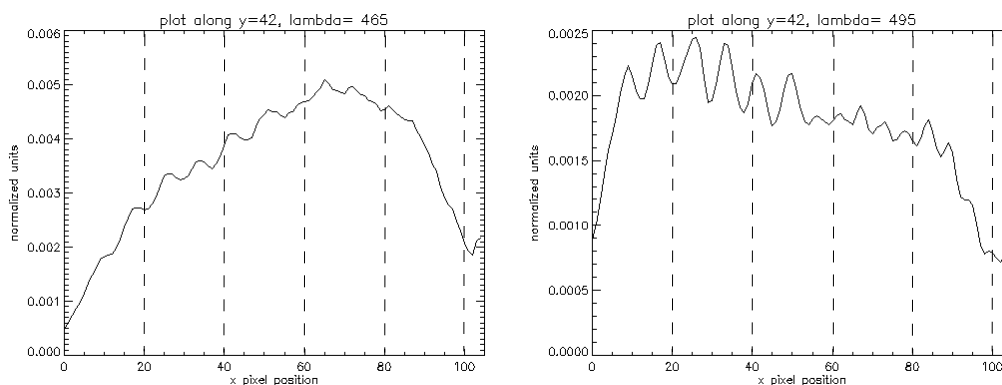


Figure 4.6c Cut along y-pixels in red and blue bars of blue data cube

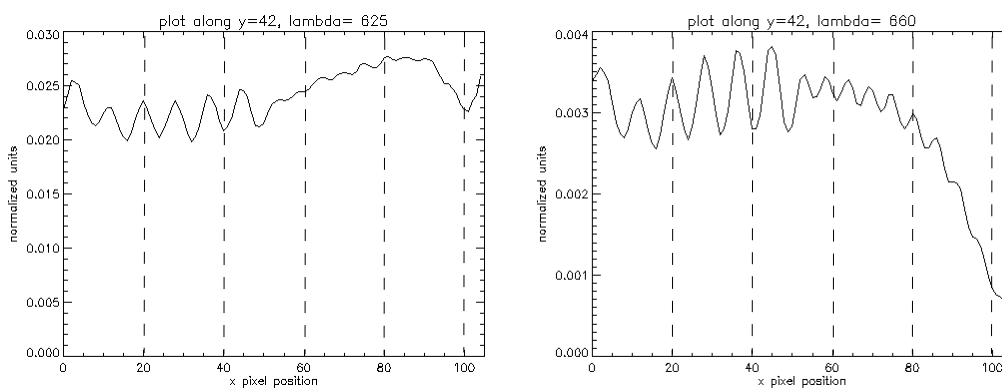


Figure 4.6d Cut along y-pixels in red and blue bars of red data cube.

The second conclusion comes from comparing the predictions in Table 4.1 with Figures 4.6. The spot size of the zero order calibration images varied between 5 x 5 and 8 x 8 pixels. Therefore, based on Table 4.1, the best resolution we could expect is a 7.7 mm object. From Figures 4.6, we can easily resolve the 6.75 mm bars and in many cases we can resolve the 4.75 mm bars. An attempt to correlate the calibration spot size to spatial resolution was unsuccessful. One thing we do see that affects the spatial resolution is the noise. Figures 4.6 a and b were reconstructions of the black and white bars while Figures 4.6 c and d were reconstructions of the red and blue bars. The

resolution is better in the black and white bar data cube than in the blue and red bar data cube. An explanation for this difference is that in the black and white case the signal in both bands is co-located. Any cross talk between bands is seen as an increased signal in the other band. In the red and blue case, because of cross talk, the signal in the blue band becomes noise in the red band and vice versa. Therefore the signal-to-noise ratio is higher in the black and white object than the red and blue object and the black and white bars have better spatial resolution than the red and blue bars.

The better spatial resolution than expected may be explained when we examine the constraint of ignoring sub-pixel effects. The conclusion that we could not reconstruct objects smaller than the voxel spatial extent in the zero order made no assumptions about the radiometric shape of the voxel. In general the voxel is close to Gaussian in the zero order. Because the voxel extent in this system covers more than one pixel, we are doing sub-voxel sampling. It is then the sub-voxel effects that are contributing to the increased spatial resolution. More work in this area is needed to characterize the expected system spatial resolution improvements.

#### **4.4.2. SPECTRAL RESULTS**

To demonstrate the dual band CTIS's ability to reconstruct the spectral signature of objects in both spectral regions, light emitting diodes and lasers are used as objects. The spectral signature of the diodes and the laser are

measured using the Ocean Optics spectrometer and that signature compared to the reconstructed spectral signature. For the red data cube, a Helium-Neon laser with a center wavelength of 633 nm is shined on a white screen. For the blue data cube, we use a blue diode with a center wavelength of around 455 nm placed on a black background. Based on the full-width half max of the calibration source, we expect to reconstruct the laser line to a 5 nm full-width half max and we would expect to reconstruct the blue diode to within 5 nm as well.

Figure 4.7 shows the reconstructed spectral signature at the center of the laser spot compared to the spectrum of the laser measured with the Ocean Optics spectrometer.

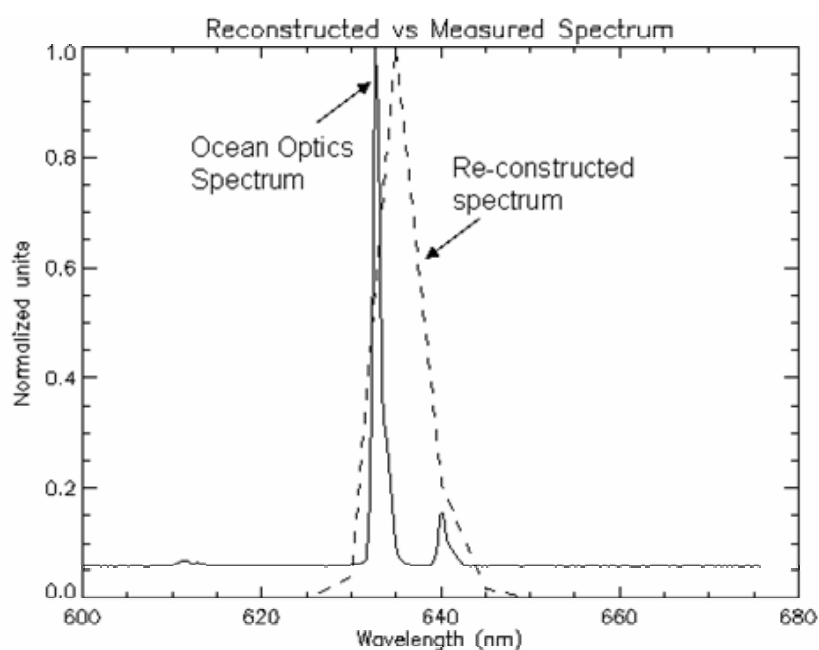


Figure 4.7: Laser spectrum reconstruction after 8 iterations of EM compared to laser spectrum measured by using the Ocean Optics spectrometer. Dashed line is the CTIS reconstruction and the solid line is measured spectrum.

From Figure 4.7, we see that the laser spectrum was reconstructed within the spectral size of the voxel. With the laser peak at 633 nm, the reconstruction could have occurred in either the 630 or 635 nm bin or both. It is probable that the small spectral feature at 640 nm drew the reconstructed peak to the 635 nm bin. We can look at Figures 4.8 a and b to examine the two reconstruction methods.

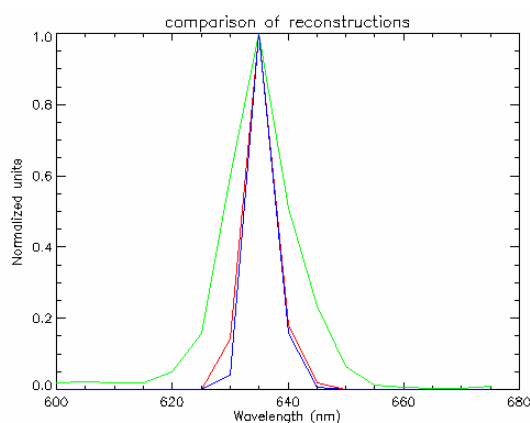


Figure 4.8a: EM reconstructions of laser

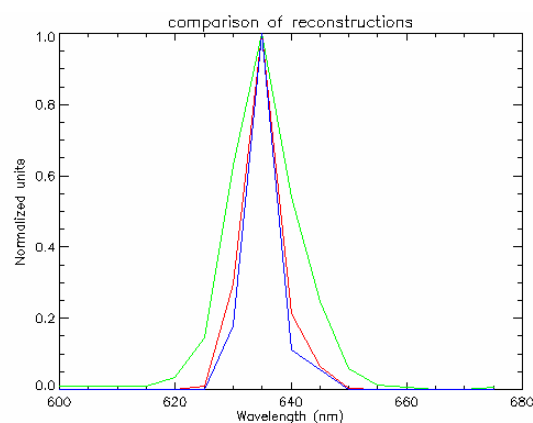


Figure 4.8b: MART reconstructions of laser

In both figures, the green line is the spectral reconstruction after one iteration, the red line is after four iterations, and the blue line is after eight iterations. In the case of the laser line, each iteration is an improvement and both techniques lead to the same conclusion about the spectral content.

Figure 4.9 shows the reconstruction of the blue diode compared to the measured spectrum at the center of the diode spot after eight iterations of EM.

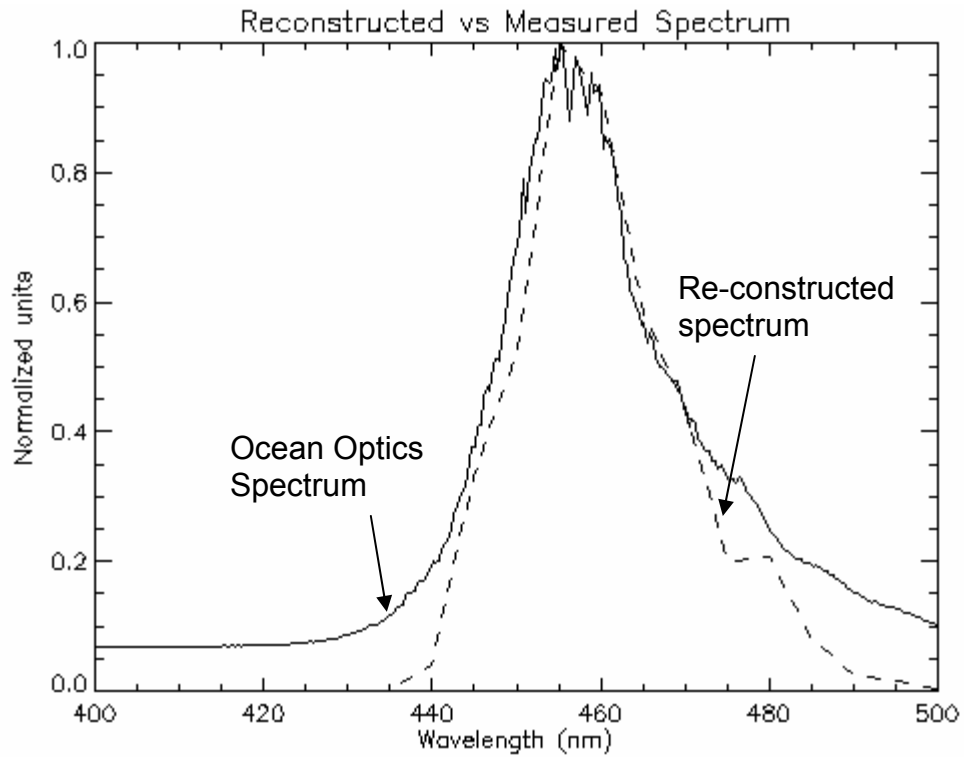


Figure 4.9: Blue diode spectrum reconstruction after 8 iterations of EM compared to spectrum measured by the Ocean Optics spectrometer. Dashed line is the reconstruction and the solid line is measured spectrum.

The reconstructed spectrum closely matches the measured spectrum of the diode. Again, we can compare the two reconstruction techniques and the number of iterations on the blue diode as we did for the laser in Figures 4.10 a and b.

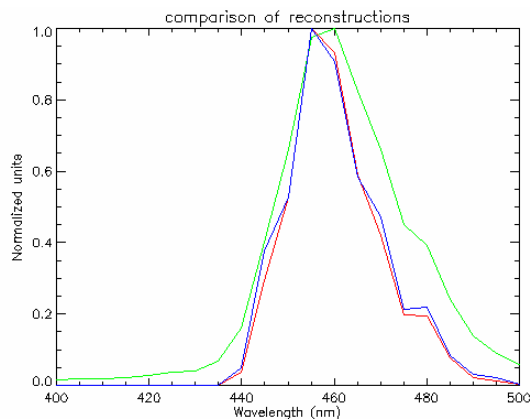


Figure 4.10a: EM reconstructions of diode

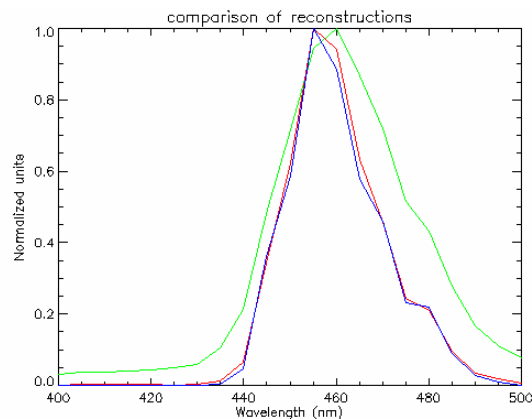


Figure 4.10b: MART reconstructions of diode

As with the laser, one iteration of the reconstruction routine is plotted in green, four iterations in red, and eight iterations in blue. For the diode reconstruction there is no improvement after four iterations of either reconstruction algorithm, and both algorithms give nearly identical results.

The goal of the spectral reconstruction was to accurately reconstruct the spectral signature of the object with 5 nm resolution. From both the laser and the diode reconstructions, we can say that they have been accurately reconstructed, but we cannot say we have 5 nm resolution. The Nyquist sampling theorem tells us that we can do no better than 10 nm. The laser in Figure 4.7 has a spectral feature at 640 nm that was included inside the reconstructed spectral signature but was not resolved. To have a chance at resolving 5 nm features we would have to take calibration images at 2.5 nm intervals or less. If there are two peak features that are separated by 5 nm, we would only see the valley between them if we sample between them. The spectral resolution is also impacted by the

relative strength of the two spectral peaks being resolved. In the case of the laser spectrum, the 640 nm peak is too weak compared to the 633 nm peak to be recognized by the reconstruction algorithms. It is fair to conclude, based on Figures 4.7 and 4.9, that the dual band CTIS system under test was able to reconstruct the spectral signatures of objects in both spectral bands within 5 nm and with a 10 nm spectral resolution.

#### **4.5. ERROR ANALYSIS**

There are not large occurrences of random and systematic errors in the spatial and spectral resolutions described above. In the spatial examples there are about a 2 pixel difference between the locations of the peaks in the black and white bars example and none in the red and blue bars example. That error can be explained by the voxel spread function being greater than 5 pixels. The two pixel error is within the size of the voxel spread function. To reduce the error, we just need to reduce the size of the voxel spread function.

In the spectral examples, we have a very accurate reconstruction and the precision of the reconstruction is limited by the sampling. In a different data set, we see a 5 nm systemic error. Figures 4.11 a and b are the reconstructions of the same laser and diode as in Figures 4.7 and 4.9. We see that the reconstructions are shifted about 5 nm to the left. There are at least two possible causes. The first is that the calibration source was putting out light 5 nm higher than expected. In fact, the spectral signatures of the calibration source, as

measured by the Ocean Optics spectrometer, had peaks in some cases 1-2 nm higher than expected (Figures C1 – C6). Also the spectral spread is not symmetrical about the peak wavelength but also skewed toward the higher wavelengths. Therefore, when we expect a 630 nm peak, we are really getting 631 or 632 nm. So when 633 nm light is present in the object, it is likely to be reconstructed as 630 nm light. The other and more probable cause of the systemic error is the alignment of the optical elements along the optical axis. During calibration, the objective lens is removed and the fiber optic from the calibration source is imaged into the field stop by a singlet. If that fiber – singlet – field stop system is aligned along an axis different from the one created by the objective and the field stop, then the calibration spread functions will be off-set from the object being reconstructed. To correct for this systematic error, we need only use a test object with a known spectral signature and reconstruct. A spectral off-set can be added to the system, and the systematic error corrected.

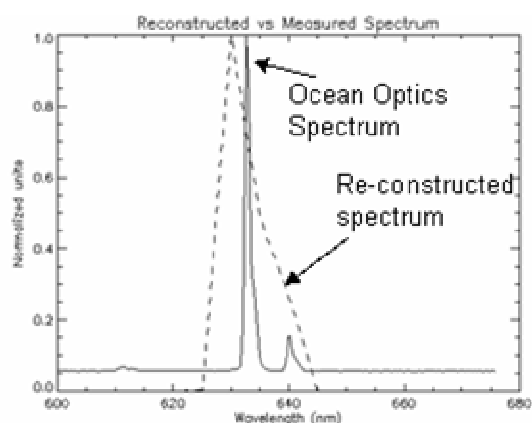


Figure 4.11a: Laser spectrum reconstruction with a systematic error

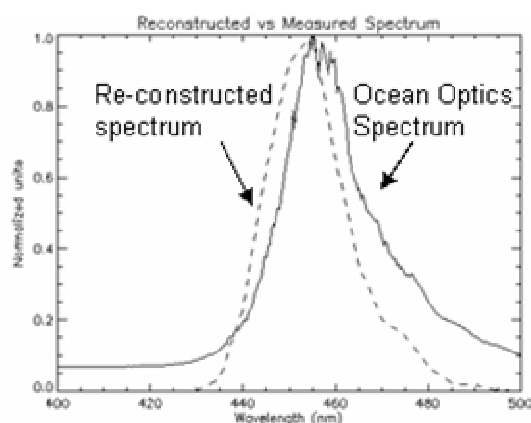


Figure 4.11b: Diode spectrum reconstructed with a systematic error

An additional source of error and uncertainty in the system is the effect of the unknown image processing that occurs within the camera. The voxel spread function is the key element in creating the  $\mathbf{H}$ -matrix and the data cube reconstruction. Because we do not know what type of imaging processing occurs within the camera, we do not know the effects of the imaging processing on the voxel spread function. The assumption that the red and blue bands are co-registered has been validated. But, assumptions about how the voxel spread function varies with radiometric strength could not be made and, therefore, not accounted for in the calibration or reconstruction. We could not characterize the cross talk between the spectral bands as a result of the image processing. Treating this cross talk as noise was the only option.

Throughout the development in Chapter 2, we ignored noise and the effects of noise on the system. The only experimental steps we used to address the noise were averaging calibration images and dark image subtraction. It was best to attempt to minimize the noise in the calibration process because the noise in the  $\mathbf{H}$ -matrix is amplified for every iteration of the reconstruction algorithms. The noise in the system did prevent the reconstruction of the data cube at wavelengths greater than 680 nm because the noise at those calibration images overwhelmed the signal.

#### **4.6. CONCLUSIONS**

From the work with the dual band visible system we can bring three things forward to the infrared system. First, using a camera with a focal plane consisting of detectors sensitive to two different spectral bands in an interwoven pattern, it is possible to reconstruct two spatially co-registered data cubes. Second, by using sub-voxel sampling, we can get better spatial resolution than the spatial extent of the voxel spread function used during calibration. Finally, the quality of the calibration is critical to accurate data cube reconstruction. The spatial reconstruction experiment demonstrated the spatial co-registration of the data cubes and showed that we can get better spatial resolution than what was predicted. The spectral reconstruction experiment shows the spectral signature of an object can be accurately reconstructed and the importance of the calibration on system performance.

## **CHAPTER 5**

### **DUAL BAND INFRARED CTIS DESIGN**

#### **5.1. DESIGN APPROACH / ASSUMPTIONS**

Now that we have demonstrated that a dual band computed tomographic imaging spectrometer is possible using an interwoven color filter visible CCD array, the next step is to extend the principle to the infrared regions of the spectrum. The bands of interest are the atmospheric transmission windows in the MWIR and the LWIR. To design a dual band IR CTIS, the three components of the optical system we have to specify are the optics, the CGH, and the focal plane array. The optics include the objective, collimating, and re-imaging components. The optical components need to be achromatized over both bands and the field dependent aberrations need to be balanced to zero to maintain shift-invariance. The basic design approach will be to first specify the focal plane parameters and geometry based on a survey of recent dual band IR focal plane technology. Then we will design the CGH and optics to achieve the design specifications with the chosen focal plane.

#### **5.2. DESIGN SPECIFICATIONS**

The design for the dual band infrared CTIS will have the following specifications:

- 1) Spectral regions of interest: MWIR and LWIR atmospheric transmission windows
- 2) System field of view:  $\pm 3$  degrees
- 3) Spatial resolution:  $1/32$  of the system field of view
- 4) Spectral resolution:  $1/30^{\text{th}}$  of the bandpass of each band or 133 nm for the LWIR band and 67 nm for the MWIR band.

The results of these specifications are that we expect to reconstruct two data cubes, one in the MWIR and the other in the LWIR. Each data cube will consist of at least  $32 \times 32 \times 30$  voxels subtending a  $\pm 3$  degree field of view.

### **5.3. DUAL BAND INFRARED FOCAL PLANE ARRAYS**

There are two types of dual band infrared focal planes that can meet the requirements for the CTIS system. The first type we will examine is the quantum well infrared photodetector (QWIP) and the second is a mercury-cadmium-telluride photodetector. Several research groups have manufactured and tested dual-band focal planes using both types. In this section we will summarize the basic physics underlying both types and the current reported state-of-the-art. We will then compare the two types of focal planes against each other. Finally, we will specify the focal plane and its parameters to be used for the remaining design of the dual IR CTIS.

### 5.3.1. QUANTUM WELL INFRARED PHOTODETECTORS (QWIP)

Quantum well infrared photodetectors (QWIPs) are photoconductive infrared detectors that use a superlattice of semiconducting materials. To better understand how and why the QWIPs work, we will start with a single quantum well. Consider a thin layer of GaAs sandwiched between two pieces of AlGaAs. A potential well is formed for the electrons in the GaAs (Figure 5.1a). Within that potential well, there are several energy states the electron can occupy as determined by the Schrödinger equation. If we add a second layer of GaAs and a third of AlGaAs, we have two potential wells side by side (Figure 5.1b). If the center barrier of AlGaAs is thin enough, then the energy states in each well split into two. Now, if we have several alternating layers of AlGaAs and GaAs, the original energy states turn into energy bands similar to that which occurs in crystals with a periodic band structure (Figure 5.1c). By applying a bias across the structure, the potential levels slope as shown in Figure 5.1d. As a photon with energy matching the separation of bands is incident on the device, an electron in the ground state band absorbs the photon and is excited to the higher state band. Because of the bias, that electron is promoted to the conduction zone and becomes part of the photocurrent.

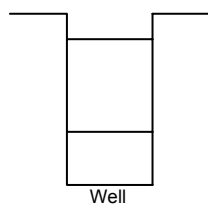


Figure 5.1a Allowed energy levels in a single quantum well

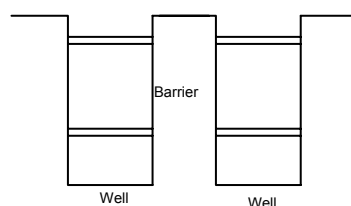


Figure 5.1b Energy level splitting due to two quantum wells in close proximity

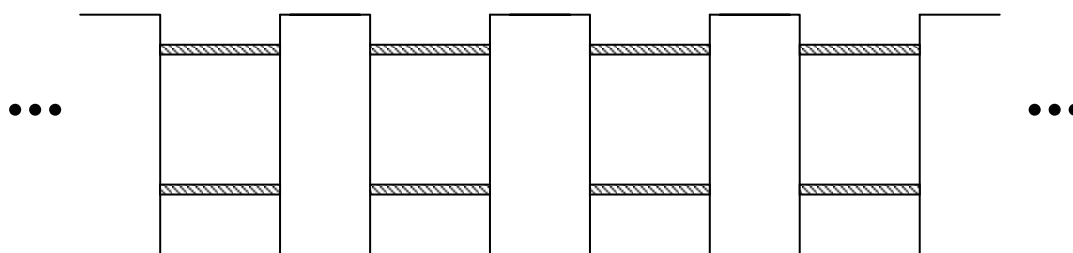


Figure 5.1c Energy banding due to a series of quantum wells in close proximity

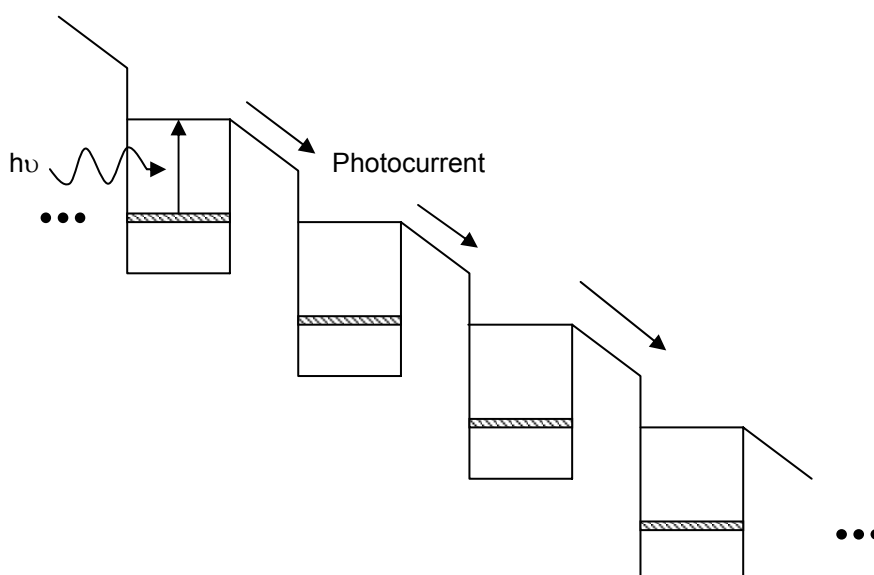


Figure 5.1d Photocurrent produced by light incident on biased QWIP structure

Controlling the spectral region for which the QWIP detector is sensitive is one of the challenges for the dual-band CTIS design. The spectral peak and cutoff of QWIP are controlled by varying the layer thickness to control the quantum well depth and changing the barrier composition to control the barrier height. The wavelength flexibility also depends on the material used to construct the well.

Dual band QWIPs have been designed and built by placing a mid-wave QWIPs on top of a long-wave QWIP structure. The dual-band QWIP is

constructed by epitaxially depositing the LWIR QWIP on a semi-insulating GaAs substrate. The detector common is placed on top of the LWIR layers and then the MWIR QWIP layers are deposited on top of the detector common. A grating is grown on top of the MWIR layer because normally incident light is not absorbed due to quantum selection rules. Finally, Indium bumps are added to connect to the readout integrated circuit (ROIC) (Figure 5.2).<sup>34</sup>

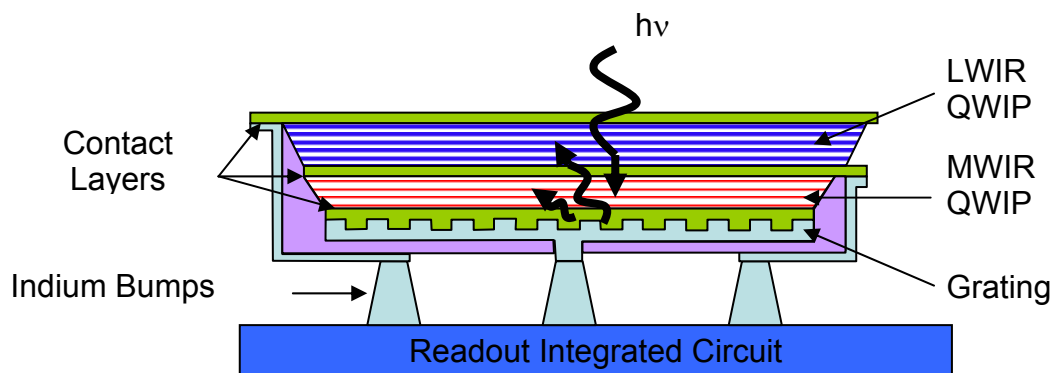


Figure 5.2 Schematic of dual band QWIP structure

As an example of some of the capabilities of QWIP arrays, JPL has developed 1064 x 1064 QWIP focal planes in both the LWIR and MWIR separately. The MWIR focal plane is reported to have a noise equivalent temperature difference (NETD) of 19 mK at 95 K operating temperature and  $f/2.5$  optics at 300 K. The LWIR focal plane NETD is 13 mK at 70 K with the same optical system as the MWIR. Both focal planes are reported to have background limited performance (BLIP) at 90 K and 70 K operating temperatures. The FPA pitch is 19.5  $\mu\text{m}$  with a 17.5 x 17.5  $\mu\text{m}$  pixel size.<sup>35</sup> AIM reports QWIP arrays in

the LWIR that are 640 x 512 with NETD less than 10 mK for an  $f/2$  system. The FPA has a 40  $\mu\text{m}$  pitch.<sup>36</sup>

Dual band QWIP focal planes have been described by QWIP Technologies Inc. for dual LWIR bands. QWIP Technologies and JPL report a 320 x 256 co-registered dual band FPA with 40  $\mu\text{m}$  pitch. The spectral peaks are at 9.2 and 12  $\mu\text{m}$ .<sup>37</sup> AIM reports a dual band QWIP covering the MWIR and the LWIR in a 384 x 288 x 2 format with 40  $\mu\text{m}$  pitch, NETD < 35 mK at  $f/2$  for both peak wavelengths (4.8  $\mu\text{m}$  and 8.0  $\mu\text{m}$ ).<sup>38</sup>

### 5.3.2. HgCdTe DETECTORS

The other type of detector that has proven effective in the MWIR and LWIR spectral regions is a detector made of Mercury-Cadmium-Telluride. HgCdTe is an intrinsic direct band semi-conductor that can be used to manufacture either a photovoltaic or photoconductive detector. In both the photoconductive and photovoltaic detectors, the incident light with energy equal to the band gap of the semiconductor promotes an electron in the valence band to the conduction band. In the photovoltaic detector, the electron transition produces a current or a voltage in the readout circuit. In the photoconductive detector, the electron transition changes the resistance or conductance of the readout circuit. HgCdTe is a good detector in the infrared because its band gap energy can vary by controlling the mole fraction of Cadmium to Mercury in  $\text{Hg}_{1-x}\text{Cd}_x\text{Te}$  and the temperature. The energy band gap is given by

$$\mathcal{E}_g(x,T) = -0.302 + 1.93x + (5.35 \times 10^{-4})(1-2x)T - 0.810x^2 + 0.832x^3 \quad (5.1)$$

where  $x$  is the mole fraction of Cadmium and  $T$  is temperature in Kelvin.

Equation (5.1) is valid for  $0 \leq x \leq 0.6$  and  $x = 1$  and for  $4.2 \text{ K} < T \leq 300 \text{ K}$ .<sup>39</sup> We should note that as the band gap energy is decreased, corresponding to higher cut-off wavelengths, the amount of Cadmium decreases and the amount of Mercury increases. The increase in the number of Mercury atoms tends to increase the number lattice vacancies making focal plane difficult to produce with uniform response past a cut-off wavelength of  $14 \mu\text{m}$ .<sup>40</sup>

Like the QWIPs, dual band HgCdTe detectors are manufactured by placing a detector sensitive to the MWIR spectral region on top of a detector sensitive to the LWIR spectral region. There are several different HgCdTe dual band designs. The MWIR sensitive layer is grown on top of the substrate followed by a barrier layer and then the LWIR sensitive layer is added. Indium bumps connect the detector assembly to the ROIC. Figure 5.3 shows a cross sectional view of a published HgCdTe design.<sup>41</sup>

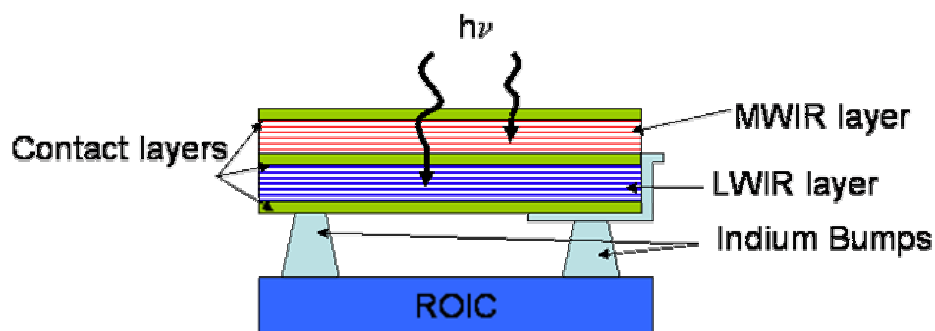


Figure 5.3: An HgCdTe dual band detector design.

As an example of some of the dual band HgCdTe dual band capabilities, Lockheed Martin reported in 1998 a 64 x 64 dual band array. The MWIR band had an average cut-off wavelength of 4.27  $\mu\text{m}$ , an average quantum efficiency of 79%, a NETD of 20 mK for a 295 K scene with a  $f/2.9$  system, a 2.2 ms integration time, and a 77 dB dynamic range. Their LWIR band had a 10.1  $\mu\text{m}$  wavelength cut-off, 67% quantum efficiency, 7.5 mK NETD and a 75 dB dynamic range under the same conditions as the MWIR.<sup>42</sup> The Dual Band FPA Manufacturing program sponsored by Army Night Vision Lab is designing a focal plane with 1280 x 720 pixel array format. The design pixel pitch is 20  $\mu\text{m}$ . The spectral regions are 3.5 – 5.0  $\mu\text{m}$  in the MWIR and 7.8 – 10.5  $\mu\text{m}$  in the LWIR. The NETD is 25 mK for both the MWIR and LWIR bands with an  $f/3.5$  at 300 K and 28 mK for both bands with  $f/6.5$  at 300 K.

There are several characteristics of QWIP arrays that make them a great choice for dual band IR focal planes. Because we control the number of stacks, the barrier height and barrier thickness, we can tune the peak wavelength from 3 – 16  $\mu\text{m}$  and we can tune the spectral width within limits. QWIPs also have a narrow spectral response with little cross talk.<sup>43</sup> QWIPs are manufactured from III-V materials which have a mature growth and processing techniques. As a result of the mature growth and processing techniques, QWIP detectors have high operability with uniform pixel-to-pixel response and lower cost.<sup>44</sup> The drawbacks of QWIP detectors are low quantum efficiency and high dark currents

requiring cooling to 65 K or lower. QWIPs also cannot absorb normally incident light because of selection rules, so they need a grating to couple the light into the detector. Although the spectral width of the QWIP is tunable, it is limited to about 1/10 of the peak wavelength ( $\Delta\lambda/\lambda \approx 1/10$ ). At 5  $\mu\text{m}$  this means the full-width-half-max of QWIP is only about 0.5  $\mu\text{m}$ . This limit is prohibitive in the CTIS system.

The HgCdTe dual band FPAs also demonstrate characteristics that make them a great choice for the dual band CTIS system. First, they can cover the IR spectrum to 14  $\mu\text{m}$  effectively. Because they are an intrinsic semiconductor, they have near unity quantum efficiency and a very low dark current. The disadvantages of HgCdTe detectors stem from the relatively poor manufacturing and processing techniques for II-VI materials. As a result, there are a high number of material defects that lead to non-uniform pixel-to-pixel response.

Both detector types show promise for dual band imaging systems. The QWIP devices need to overcome the low quantum efficiency and high dark current to be the technology of choice. The HgCdTe detectors need to improve the manufacturing process to get a uniform pixel-to-pixel response. Based on current focal plane technologies, we will design the CTIS system assuming a 1280 x 720 pixel focal plane array with a 20  $\mu\text{m}$  pitch. We also assume that the MWIR detector is stacked on top of the LWIR sensitive detector. This results in a 25.6 mm x 14.4 mm focal plane. The MWIR spectral region will be from 3.5 - 5.0  $\mu\text{m}$  and the LWIR spectral region will be from 7.8 - 10.5  $\mu\text{m}$ .

#### 5.4. CGH DESIGN

Now that we have specified the focal plane geometry, we can design a CGH using the algorithm described in Chapter 3 to achieve the design goals. The design variables we have to choose from are the CGH material, the CGH unit cell size, and the design diffraction pattern. To insure the CGH design remains in the Fraunhofer limit we will use square phasels that are  $24\ \mu\text{m}$  a side.

The first design variable we will address is which material to use for the CGH. There are two basic options, Silicon and Germanium. These two materials are considered viable options because they are transparent in the infrared, they have a relatively constant index of refraction over the entire spectral region, and the manufacturing techniques are fairly mature. Figure 5.4 contains the index of refraction curves for these materials. From the figure, we see that the index of refraction for Silicon varies less than 0.5% over the entire spectrum and Germanium varies about 1%. Then, because we can assume that the index of refraction for both materials is a constant over both spectral regions, we can design the CGH etch depth profile for either and scale the profile for the other material. The final decision on which material to use depends on which material is less expensive to purchase and manufacture. We will design the CGH for Silicon because its index of refraction varies the least.

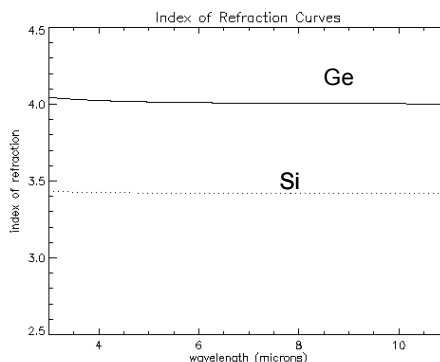


Figure 5.4 Index of refraction curves for CGH materials in the infrared<sup>45</sup>

There are three basic diffraction patterns available for a dual band IR system. The three options, as shown in Figure 5.5, are the Uniform3, the Hybrid, and the Ring patterns. The Uniform3 pattern consists of the  $\pm$  first diffraction orders in both bands with equal diffraction efficiency in all orders. The Hybrid pattern consists of  $\pm$  first and second diffraction orders in the MWIR with the outer orders having a higher diffraction efficiency than the inner orders and only the  $\pm$  first orders in the LWIR band with uniform efficiency in all orders. We strengthen the diffraction efficiency of the outer orders when we have two or more diffraction orders to balance the effects of the sinc envelope caused by the rectangular shape of the phasels. The Ring diffraction pattern is the same as the Hybrid except the first diffraction order of the MWIR band is suppressed leaving only the zero order and  $\pm$  second orders. In addition to the Uniform3, Ring and Hybrid patterns designed using the algorithm described in Chapter 3, we will also evaluate a uniform 3 pattern designed using the algorithm for single band CTIS systems described by Volin.<sup>46</sup>

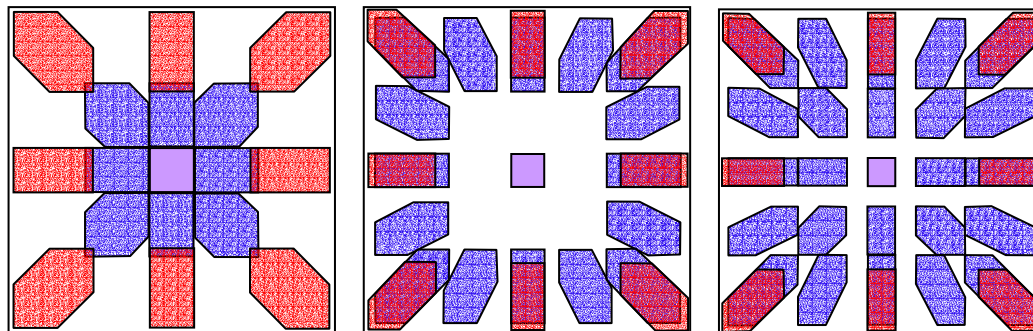


Figure 5.5 CGH Design patterns. From left to right, Uniform 3, Ring, and Hybrid. The Purple section is the zero order. The blue is the MWIR regions and the red is the LWIR regions

The next design decision is to choose the size of the CGH unit cell. The options we considered were the 8 x 8, 10 x 10 and 16 x 16 phasel unit cells. These sizes were chosen for purely historical reasons in that the existing CGH design algorithms were limited to these three choices. There are several competing design effects that must be balanced. First, the more a unit cell is replicated the more punctile the resulting diffraction points from a quasi-monochromatic, quasi-point source. The larger the unit cells, the fewer replications of the unit cell are possible over the same CGH area. So the smaller the unit cells the better. Also, the more phasels in the unit cell, the smaller the overall diffraction pattern is on the focal plane for the same optical components. For a simple demonstration of this effect, consider Figures 5.6a and 5.6b. Figure 5.6a is the projected diffraction pattern for a CGH with  $\pm$  two diffraction orders and with an 16 x 16 phasel unit cell designed over the MWIR (3.5-5.0  $\mu\text{m}$ ) for a 720 x 720 pixel FPA with 20  $\mu\text{m}$  pitch. The effective imaging lens focal length is 120 mm, the collimating lens effective focal length is 480 mm and the field stop is

5 mm. Figure 5.5b is the projected diffraction pattern for the exact same system except the CGH unit cell is an 8 x 8.

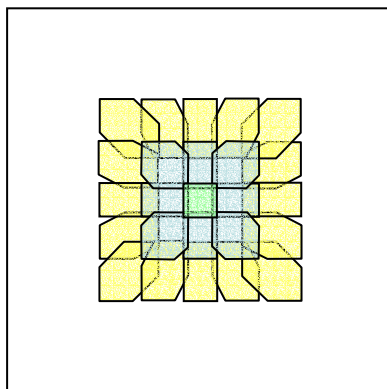


Figure 5.6a: Diffraction pattern on FPA from 16x16 CGH unit cell

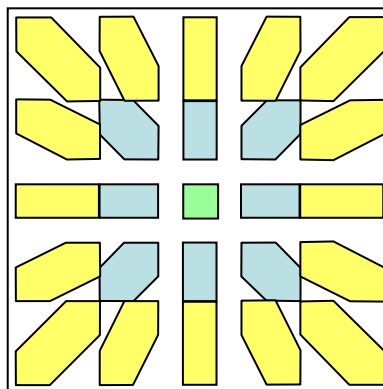


Figure 5.6b: Diffraction pattern on FPA from 8x8 CGH unit cell

Comparing the figures we see that the 16 x 16 unit cell occupies a small area on the focal plane, and also suffers from order overlap. In the 16 x 16 unit cell case, the first diffraction order overlaps almost 8 linear pixels of the zero order in each direction and the second order overlaps 31 linear pixels of the first order in each direction. The spectral dispersion for the 16 x 16 CGH cell is 17.45 nm per pixel in the first order and 13.71 nm per pixel in the second order whereas the 8 x 8 CGH unit cell has a 13.71 nm per pixel in the first order and 9.60 nm per pixel dispersion in the second order. The advantage of the 16 x 16 CGH unit cell is that there are more degrees of freedom for assigning etch depths. Table 5.1 contains the diffraction efficiencies for the different diffraction patterns and the different unit cells.

### Comparison of design stats averaged over 10 designs

Mask	Cell Size	MWIR	MWIR	MWIR	LWIR	LWIR	LWIR	SUM	SUM
		Order	Total		Order	Total			
		Mean	Mean	Max	Mean	Mean	Max	Mean	Max
Old	8x8	4.40	39.64	45.63	4.52	40.66	47.09	80.29	92.72
Old	10x10	4.34	39.09	56.88	4.52	40.71	56.86	79.80	113.73
Old	16x16	4.41	39.72	44.57	4.48	40.28	43.78	79.99	88.36
Uniform3	8x8	4.61	41.53	54.16	4.78	43.02	53.23	84.55	107.39
Uniform3	10x10	4.22	38.00	48.94	4.36	39.23	49.09	77.22	98.03
Uniform3	16x16	3.86	34.73	42.36	3.95	35.54	42.68	70.27	84.62
Ring	8x8	3.15	53.50	59.91	2.60	23.36	27.24	76.86	85.12
Ring	10x10	2.73	46.36	51.61	2.28	20.51	25.67	66.86	77.28
Ring	16x16	2.43	41.30	46.21	2.12	19.10	22.12	60.40	68.33
Hybrid	8x8	2.33	58.23	61.90	2.05	18.48	21.73	76.71	81.84
Hybrid	10x10	1.84	46.00	51.46	1.73	15.53	17.00	61.54	68.47
Hybrid	16x16	1.49	37.21	44.86	1.49	13.41	15.59	50.62	60.45

Table 5.1 Comparison of mean diffraction efficiencies for the different CGH cell sizes and diffraction patterns

The order mean columns for the MWIR and LWIR bands contain the average diffraction efficiency of all desired diffraction orders over all wavelengths in the band for ten designs run at 60 iterations each. The MWIR and LWIR total mean columns are the sum of the diffraction efficiencies of all orders of interest averaged over all wavelengths in the band. The sum mean column is the sum of the MWIR and LWIR total mean columns. The max columns give the highest trial value for each design. To determine these efficiencies, we calculate the irradiance at the focal plane by taking the absolute value squared of the fast Fourier transform of transmittance of the CGH at each wavelength. Then we divided the irradiance in each desired diffraction order by the total irradiance at each wavelength. We then averaged the diffraction efficiency of all desired diffraction orders and averaged that over all wavelengths in the band. This gave

the order mean value. We then multiplied the order mean value by the number of desired diffraction orders to get the total mean values. From the Table 5.1, we see that for all design patterns the smaller the unit cell, the more light falls in the desired diffraction orders. We can explain this when we consider that the fast Fourier transform we used to calculate the irradiance pattern is a point-to-point mapping. The point-to-point nature means that if the unit cell is  $8 \times 8$ , then there are 64 points for the irradiance pattern to occupy. For the  $16 \times 16$  there are 256 locations the light can go. Then, even if a very small amount of light goes into each of the undesired locations of the  $16 \times 16$  unit cell, it is adding up to a greater percentage than the light going into the undesired locations of the  $8 \times 8$  unit cell. The other explanation is that the additional degrees of freedom from the larger CGH unit cells are used to make the diffraction efficiencies between the orders more uniform. We see evidence of this effect when we look at the root-mean-square (RMS) deviation from average of the diffraction efficiencies of each order. Table 5.2 shows the RMS deviation from average for each of the diffraction orders of interest averaged over all wavelengths. We see that as the unit cell size increases, the RMS deviation in both bands decreases except for the ring pattern  $16 \times 16$  unit cell in the LWIR.

Mask	Cell Size	MWIR RMS	LWIR RMS
Old	8x8	3.03	2.51
Old	10x10	2.02	1.85
Old	16x16	1.66	1.49
Uniform3	8x8	3.50	3.33
Uniform3	10x10	2.94	2.85
Uniform3	16x16	2.48	2.40
Ring	8x8	9.65	2.46
Ring	10x10	8.08	1.95
Ring	16x16	7.11	2.10
Hybrid	8x8	4.06	1.87
Hybrid	10x10	2.88	1.33
Hybrid	16x16	2.17	1.29

Table 5.2: RMS deviation from average diffraction efficiency averaged over all wavelengths

From Table 5.1 we see that the Uniform3 design using the old algorithm puts more light into the desired orders on average than the other designs. This is most likely because the design patterns for both spectral bands are the same. Further evidence to support this conclusion comes from examining the plots of the diffraction efficiency of each diffraction order as a function of wavelength. Figures 5.7 a – c are the diffraction efficiency plots for the best 8 x 8 unit cell trial results for each design pattern. Appendix B contains similar plots for the best design for each unit cell and pattern.

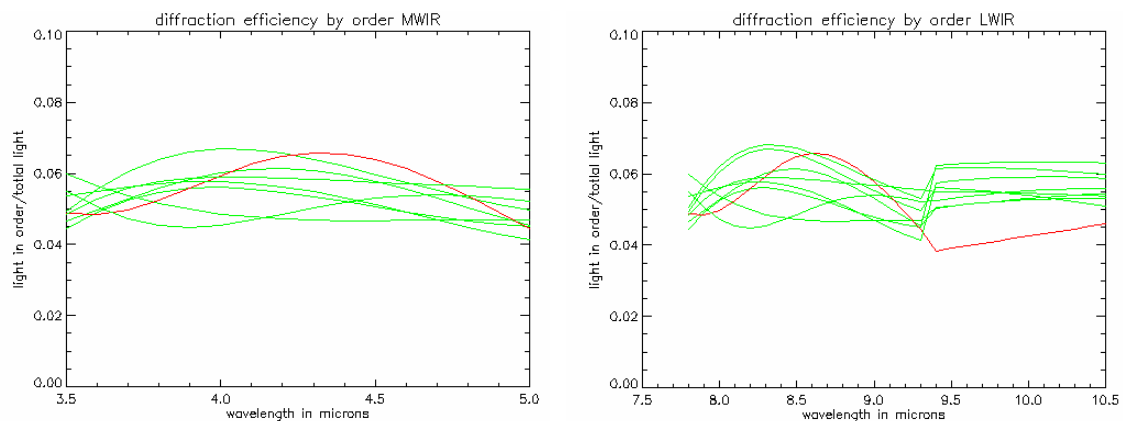


Figure 5.7a MWIR and LWIR diffraction efficiency for Uniform3 pattern. Red plot is the zero order.

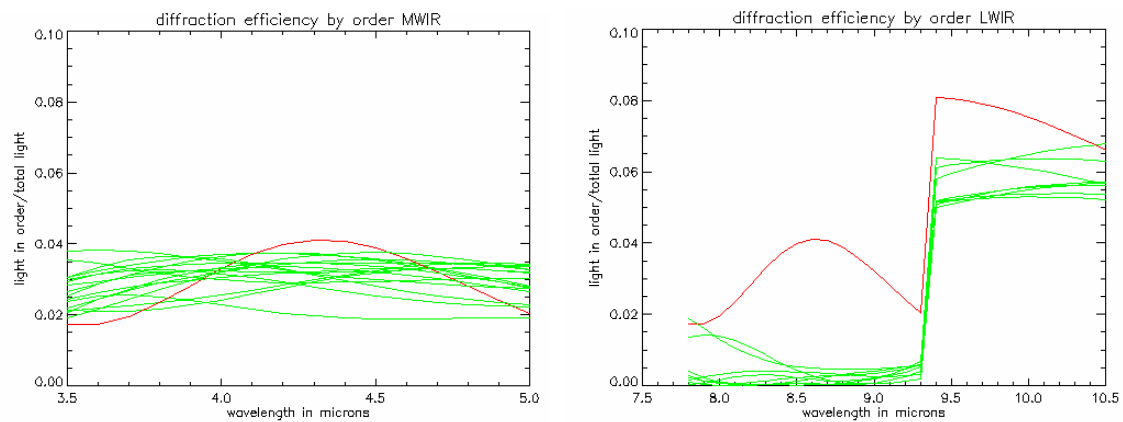


Figure 5.7b MWIR and LWIR diffraction efficiency for Ring pattern. Red plot is the zero order.

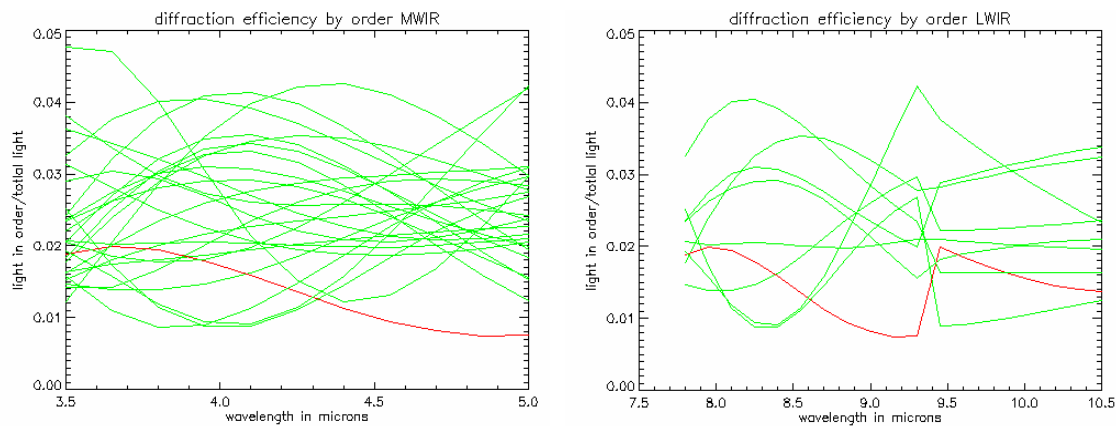


Figure 5.7c MWIR and LWIR diffraction efficiency for Hybrid pattern. Red plot is the zero order.

In all design patterns there is a discontinuity near  $9.4 \mu\text{m}$ . This effect was also present in similar work by Jim Scholl.<sup>47</sup> One possible explanation for the discontinuity is the change in the diffraction pattern between the bands. During the design process, we specified the design pattern for each band. For each spectral band we designed at  $0.15 \mu\text{m}$  wavelength interval within the bands,  $0.5 \mu\text{m}$  between the two spectral bands. The break between bands occurred at  $6.5 \mu\text{m}$ . We would expect the discontinuity to occur at  $10 \mu\text{m}$  because it is an integral multiple of the end of the MWIR band where we have relaxed some of the constraints on the system. This discontinuity deserves further investigation.

## 5.5. OPTICAL DESIGN

Before we can decide on the CGH design, we must consider the remaining optical components and their effects on the farfield irradiance pattern. In particular, we were most concerned about the field stop size and the focal lengths of the imaging and collimating lenses. The imaging lens determined the spectral dispersion of the CGH. The ratio of the imaging lens and collimating lens focal lengths determined the system magnification. The system magnification combined with the field stop size determined the zero order size and thus the system spatial resolution.

We start by considering how the spectral dispersion is related to the imaging lens focal length. Recall from equation (3.17) that the complex amplitude on the focal plane is given by:

$$u(x, y) \propto \sum_{m,n=0}^{q-1} \exp(i\Phi_{mn}) \exp\left(-i \frac{2\pi}{\lambda f} (mx_c x + ny_c y)\right) \times \sum_{k,l=-\infty}^{\infty} \delta\left(x - \frac{k\lambda f}{qx_c}\right) \delta\left(y - \frac{l\lambda f}{qy_c}\right) \text{sinc}\left(\frac{x_c x}{\lambda f}\right) \text{sinc}\left(\frac{y_c y}{\lambda f}\right). \quad (5.2)$$

Here it is the delta functions that describe the spectral dependence of the diffraction pattern. We can calculate where the light of a given wavelength will strike the focal plane by:

$$x = \frac{k\lambda f}{qx_c} \quad (5.3)$$

where  $x$  is the distance from the zero order to the  $k^{\text{th}}$  diffraction order,  $\lambda$  is the wavelength of interest,  $q$  is the number of phasels on a side of the CGH unit cell,  $x_c$  is the actual width of a phasel, and  $f$  is the effective focal length of the re-imaging lens. We can also use this equation to determine the spectral resolution of the system. By looking at the differential change in  $x$  with a differential change in  $\lambda$  we have:

$$\Delta x = \Delta \lambda \frac{kf}{qx_c}. \quad (5.4)$$

Then by setting  $\Delta x$  equal to the pixel size of the focal plane, we specify the spectral resolution of that order given the other parameters. We can also solve for the re-imaging focal length by solving equation (5.4) for  $f$  using the required spectral resolution,  $\Delta \lambda$ , and pixel size,  $\Delta x$ .

Once we specify the re-imaging lens focal length, we can specify the collimating lens focal length and field stop size using the magnification equation:

$$m = -\frac{f_i}{f_c} \quad (5.5)$$

where  $f_i$  is the re-imaging lens focal length and  $f_c$  is the collimating lens focal length. Given the size of the field stop, the zero order will subtend an area the size of the field stop times the magnification factor.

For CGH designs that use the second diffraction orders, we must also be concerned about order overlap between the first and second orders in that spectral band. Using equation (5.3) we can calculate the position of the second order spot from the lowest wavelength by:

$$x = \frac{2\lambda_{\min}f_i}{qx_c} \quad (5.6)$$

To calculate the order overlap we let  $x = 0$  at the left side of the zero order. The position of the first order diffraction spot for the highest wavelength in the band from the right side of the zero order is then given by:

$$x = \frac{\lambda_{\max}f_i}{qx_c} + \left(\frac{f_i}{f_c}\right)x_{field} \quad (5.7)$$

where  $x_{field}$  is the width of the field stop. The second term accounts for the magnification in the system and the size of the zero order. If the value for  $x$  in equation (5.7) is greater than or equal to the  $x$  in equation (5.6), then there is order overlap.

To design the optical system we iterate equations (5.3) thru (5.7) until we optimize the system. To optimize the system, we attempt to maximize the percentage of the focal plane used and meet the minimum resolution requirements. During the system optimization we will also look ahead to the optical component design and attempt to make the imaging and collimating components have the same focal lengths. This way we are invoking symmetry to try and minimize the aberrations. Because the pixel pitch of our focal plane is 20  $\mu\text{m}$ , a good goal is a 100 x 100 pixel zero order. This leads to a 2 mm stop size. Using this 2 mm stop as the starting point, we can now compare resolution and percentage of the focal plane used between the different design masks and unit cell sizes. Tables 5.3a and b show the results of optimizing the focal plane usage.

Mask	Cell Size	Collimating Focal Length (mm)	Imaging Focal Length (mm)	Stop Size (mm)
Uniform3	8x8	110	110	2.0
Uniform3	10x10	140	140	2.0
Uniform3	16x16	225	225	7.0
Ring	8x8	600	115	7.5
Ring	10x10	660	140	6.5
Ring	16x16	1150	225	7.0
Hybrid	8x8	720	120	7.5
Hybrid	10x10	720	150	6.0
Hybrid	16x16	950	239	5.0

Table 5.3a Optimal component focal lengths and field stop size for each diffraction pattern and CGH cell size

Mask	Cell Size	Zero Order Size (pixels)	MWIR Spectral Resolution 1st order (nm)	MWIR Spectral Resolution 2nd order (nm)	LWIR Spectral Resolution (nm)	% MWIR Pixels Used	% LWIR Pixels Used
Uniform3	8x8	100	10.5	-	15.2	21.1	21.6
Uniform3	10x10	100	10.4	-	15.1	21.9	23.8
Uniform3	16x16	100	10.4	-	15.1	21.9	23.8
Ring	8x8	71.9	-	9.3	17.0	35.4	12.7
Ring	10x10	68.9	-	9.6	17.6	32.9	11.7
Ring	16x16	68.5	-	9.6	17.6	32.6	11.6
Hybrid	8x8	62.5	13.7	9.6	17.8	39.2	10.2
Hybrid	10x10	62.5	13.7	9.6	17.8	39.2	10.2
Hybrid	16x16	62.9	13.7	9.6	17.8	39.4	10.3

Table 5.3b Optimal spectral and spatial resolution and focal plane usage for each diffraction pattern and CGH cell size

From Table 5.3a we see that we can use a magnification of unity for the Uniform3 diffraction pattern. When there is more than one diffraction order in the diffraction pattern, we must increase the size of the field stop and demagnify the image of the field stop on the focal plane. When there is no demagnification of the field stop, the adjacent diffraction orders in the second order overlap in corners as shown in Figure 5.8. Figure 5.8 is the pattern on the focal plane for the hybrid pattern with a 2 mm field stop, 110 mm effective focal lengths for both the collimator and re-imager, and an 8 x 8 unit cell. The darker areas are the areas of overlap between adjacent diffraction orders.

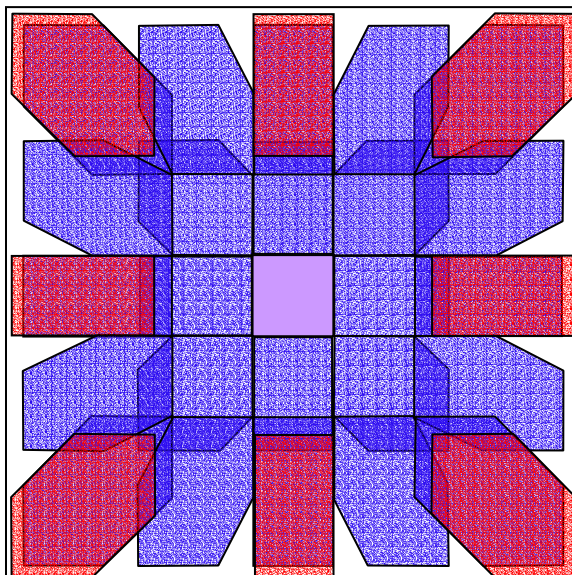


Figure 5.8. Diffraction pattern for hybrid design pattern with a 2 mm field stop, 110 mm effective focal lengths for both the collimator and re-imager, and an 8 x 8 unit cell

The first criteria we will use to determine the optimal CGH and optics design is whether or not the design spectral and spatial resolution can be achieved on the given focal plane. From Table 5.3b, we see that all of the designs easily meet the minimum design criteria. The hybrid design is the only design that does not allow us to at least double the minimum number of pixels per edge, but it is only short by just over one pixel. This is because in the MWIR band the corner first diffraction order at the upper end of the band began to overlap the diffraction orders just off the corner from the second order (Figure 5.5). For the ring and uniform patterns there is not much improvement in the spectral resolution of the system in the MWIR. The ring and hybrid patterns do have the advantage of more projections through the data cube which will improve the reconstruction effort. From Table 5.3b, we also see that in the LWIR, the

spectral resolution of each design is similar. This is because the LWIR band is the limiting factor in keeping the diffraction pattern on the focal plane. The ring pattern was designed to suppress the first order of the MWIR so the second MWIR orders could be brought in closer to the zero order and increase the spectral resolution of the system. The Hybrid and the Ring pattern try to take greater advantage of the dual band focal plane by including the second order of the MWIR; but, as we saw in Table 5.1, this occurs at the expense of the diffraction efficiency. We would prefer to use shorter focal length optics which favor the designs that use 8 x 8 unit cells.

Everything so far assumes that the system is diffraction limited. For the CTIS system, this means that during the calibration process the zero order spot size of the calibration source fits inside a single pixel. To insure the diffraction limit we use:

$$D=2.44\lambda f/\# \quad (5.8)$$

where  $D$  is the diameter of the Airy pattern, and  $f/\#$  is the f-number of the lens given, and  $\lambda$  is the longest wavelength to be used. Using the pixel pitch of 20  $\mu\text{m}$  as the Airy disk diameter and the maximum wavelength of 10.5  $\mu\text{m}$ , the required  $f/\#$  is 0.78. Because we were able to get at least 64 pixels in the zero order of all but the hybrid pattern, we can relax the diffraction limit to two pixels across and use a  $D$  of 40  $\mu\text{m}$ . As a result, we can use a slower system and allow the  $f/\#$  to

go as high as 1.5 and still get 32 square voxels per wavelength in our reconstruction.

Based on the total diffraction efficiency, the spatial and spectral resolution capabilities, and that the collimating and re-imaging components are symmetrical, we choose the Uniform3 diffraction pattern. Based on balancing the smaller required focal lengths, the increased puntility of the diffraction pattern due to the greater number of replications of smaller CGH unit cells, and the advantage that larger unit cells result in more uniform diffraction efficiencies between diffraction orders, we choose the 10 x 10 phasel unit cell. These choices lead to a 2 mm field stop and 140 mm effective focal length collimating and re-imaging components at  $f/2$ . The recommended etch depth profile is in Appendix D.

### **5.5.1. OPTICAL COMPONENTS**

Now that we have specified the effective focal lengths of the collimating and imaging lens, we must design the objective optics and choose the elements that will achieve the design focal lengths while minimizing aberrations. First, we specify the objective effective focal length. Then, we pick the optical elements that will achieve the design effective focal lengths in an efficient manner.

To determine the effective focal length of objective optics, we need the field stop size and the design field of view. Figure 5.9 shows the portion of the CTIS system that includes the objective and the field stop. From the Figure 5.9,

we see that the effective focal length is half the field stop divided by the tangent of the half angle field of view.

$$f_o = \frac{x_s}{\tan \theta} \quad (5.9)$$

For  $\theta$  equal to 3 degrees and  $x_s$  equal to 1 mm, we find that the effective focal length of the objective is 19.1 mm.

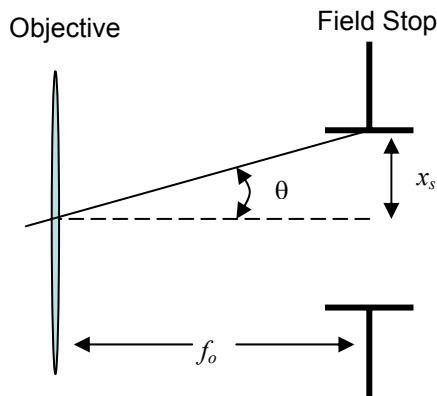


Figure 5.9: Objective and field stop of CTIS system

### 5.5.2. OPTICAL DESIGN

For the optical design of the dual IR band CTIS, we perform a first order design of a reflective and refractive system. We specify the criteria to help determine which optical design is best and discuss options to improve the first order design.

The first design criterion is that each of the three optical components meets the effective focal length and  $f/\#$  requirement. Although this seems trivial,

it is possible, while in the design loop, to allow these parameters to slip. The second criterion is the minimization of noise due to “hot” components. As the components warm-up, their blackbody emissions in the spectral regions of interest will begin to become significant and contribute to the noise. The two factors we need to consider in minimizing the thermal noise are the overall size of the system that needs to be cooled, how to thermally couple the elements to facilitate uniform cooling, and how to create a vacuum environment for the optical components. The third criterion is the minimization of aberrations in the system.

Now that we have established the criteria for choosing an optical design, we start by exploring whether the system should be reflective or refractive. In general, we prefer to use a reflective system because there are no chromatic aberrations in a reflective system and reflective systems are also easier to cool and maintain a vacuum seal. It is easier to cool a reflective system because we can access the backside of the entire surface for thermal couplers, but in a refractive system we can access only the edges of the lenses. The problem with a reflective system is that the CTIS system cannot have a central obscuration. Therefore, a reflective system needs to be an off-axis system. At  $f/2$ , the off-axis angle can be severe to prevent obscuration.

In order to minimize the negative effects of an off-axis system, the objective for the off-axis reflective system is refractive. The system then consists of a lens as the objective and off-axis parabolic mirrors as the collimator and re-imager as in Figure 5.10.

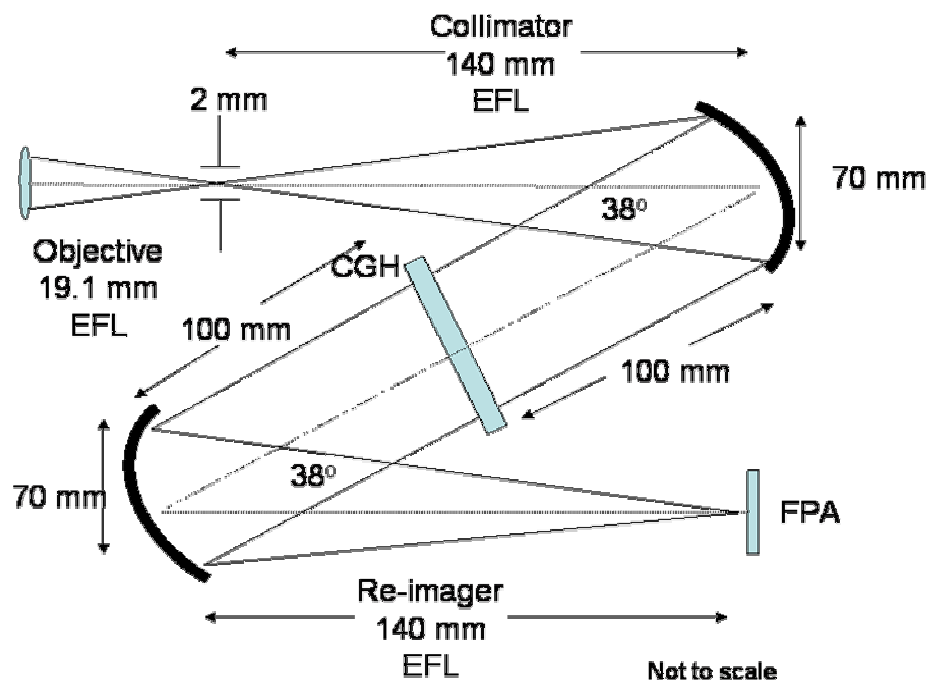


Figure 5.10: Sketch of refractive CTIS design.

Using ray trace techniques of the marginal and chief rays, we find the minimum deviation of the optical axis is around  $38^\circ$  for both the collimator and re-imager. For this design the CGH needs to be about 70 mm in diameter. If we compare this with a refractive system also composed of only one lens for each of the optical components, we find the diameter of the collimated space is also about 70 mm.

Typically the dominant aberration in an off-axis parabolic system is astigmatism. The fact that the collimating and re-imaging mirrors are symmetric allows for some balancing of the astigmatism between the two mirrors. Another

method to reduce the astigmatism is to add a cylindrical lens to the system to balance the power between the horizontal and vertical meridians. The drawback of using the cylindrical lens is that we are adding another optical element, and we are giving-up the advantages of the reflective system.

When considering a refractive system, we have two concerns to address. The first concern is that there is an inherent reflection off the air-lens interfaces. The lens material considered for these designs is Silicon because it is readily available and has low dispersion across the spectral region. The index of refraction of Silicon is around 3.4. Therefore, at the air-Silicon interface the reflectance is around 30%. Adding an anti-reflectance thin film coating to the lenses mitigates the reflection losses. We cannot design a perfect anti-reflection coating covering the large spectral region of the dual band CTIS, but we can design one that reduces the reflectance at each interface to a couple of percent.<sup>48 49</sup>

The other concern we have to address for the refractive system is the dispersion inherent in the lens material that causes chromatic aberrations. To address the chromatic aberrations in the IR region, we can achromatize the system in a manner similar to that used in the visible spectrum. To balance chromatic aberrations in the visible portion of the spectrum, we use the Abbe number of the lens material to calculate the focal lengths of two different material lenses for a doublet. In the visible portion of the spectrum, the Abbe number is defined as the refractivity divided by the principal dispersion and is calculated by:

$$v = \frac{n_d - 1}{n_F - n_C} \quad (5.10)$$

where  $v$  is the Abbey number,  $n_d$  is the index of refraction of the material at the Helium line of 587.6 nm,  $n_F$  is the index of refraction of the material at the Hydrogen line of 468.1 nm, and  $n_C$  is the index of refraction for the material at the other Hydrogen line at 656.3 nm. The Abbey number is used to create an achromatic doublet by combining two lenses of different material so that the  $F$  and  $C$  wavelengths come to focus at the same lateral position. These two wavelengths come to the same focus when:

$$f_a = f \left( \frac{v_a - v_b}{v_a} \right) \quad \text{and} \quad f_b = f \left( \frac{v_b - v_a}{v_b} \right) \quad (5.11a \text{ and } b)$$

where  $f$  is the desired lens focal length,  $f_a$  and  $f_b$  are the focal lengths of the constituent doublets, and  $v_a$  and  $v_b$  are the Abbey numbers of the  $a$  and  $b$  lens materials. To make a positive achromatic doublet, we can combine a positive low Abbey number material with a negative high Abbey number material. For a negative achromatic doublet, we combine a negative low Abbey number material and positive low Abbey number material. To apply this concept to the infrared spectrum of this CTIS system, we will define an infrared Abbey number as:

$$v_{IR} = \frac{n_7 - 1}{n_3 - n_{11}} \quad (5.12)$$

where the subscript on the index of refraction refers to the wavelength in microns of the index of refraction.<sup>50</sup>

The materials that are readily available to manufacture infrared lenses are Germanium, Silicon, Zinc Selenide, and Zinc Sulfide. Table 5.4 contains the indices of refraction and calculated IR Abbey number for each.

	Ge	Si	ZnSe	ZnS
11 $\mu\text{m}$	4.003	3.416	2.398	2.185
7 $\mu\text{m}$	4.007	3.419	2.400	2.230
3 $\mu\text{m}$	4.045	3.432	2.438	2.257
$v_{\text{IR}}$	70.753	151.188	35.354	17.083

Table 5.4 IR lens material properties

We have chosen to use Silicon and Germanium to create the achromatic doublets because those two materials are readily available, and they have nearly a factor of two difference in Abbey numbers for ease of calculations.

Our refractive design consists of three achromatically balanced doublets as in Figure 5.11.

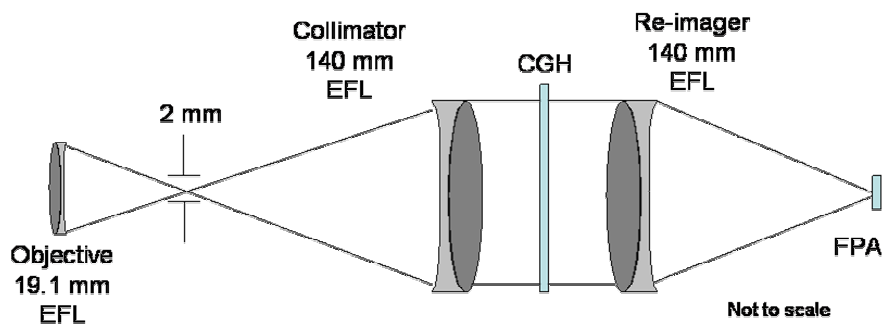


Figure 5.11: Sketch of refractive CTIS optical design

Using the symmetry of the design behind the field stop again provides an opportunity to balance aberrations. We could also add more elements to try to balance aberrations; but that would increase the cost and the reduction of the light passing through the system does not outweigh the benefits.

Comparing the refractive and reflective systems, we find there will be similar aberrations in both cases. The low  $f/\#$  leads to significant pupil dependent aberration with spherical aberrations and astigmatism leading the way. Even with the aberrations, the systems as designed are viable but with degraded performance. Based on the field dependent aberrations such as astigmatism and coma, we cannot assume that the system will be linearly shift independent. Because the reflective system is folded over on itself, it is more compact and easier to cool. The reflective system does not suffer from chromatic aberrations. The refractive system will be easier to align and collimate as off-axis parabolas, can be more difficult because they are not rotationally symmetric. Based on the ease of cooling and the absence of chromatic aberrations, the reflective system is the design of choice.

Both designs above are first order designs; that is, aspheres and diffractive optical elements were not considered. As mentioned above, it is also possible to add additional optical elements to each of the components to give an additional degree of freedom and reduce the effects of aberrations. The drawback with adding elements is increased cost, increased difficulty to cool the

system, and a reduction of the transmitted light through the system. The optical component specifications using Code V<sup>®</sup> are located in Annex D.

The true limit on the performance of this system is the very low  $f/\#$ . Recall the  $f/2$  limit came from spatial resolution requirement. We want to use the rule of thumb that the number of voxels along a spatial axis is given by the length of the zero order image of the field stop on the focal plane, divided by the diameter of the diffraction limited Airy disk. From the visible dual band system, we saw we could get better resolution than the length of the field stop image divided by the spot size in the zero order. But that spot size is more equivalent to RMS spot diameter from the spot diagram. So our rule of thumb to use the Airy disk diameter instead of the RMS spot diameter, balances the sub-voxel sampling effects. A method to improve the system is to increase the  $f/\#$ , but, to maintain the spatial resolution, we have to also increase the size of the zero order. To increase the size of the zero order, we need a bigger focal plane. So, although the dual IR band CTIS system is possible given the design requirements, to improve the overall CTIS system performance, the dual IR band focal planes need to double the number of pixels so we can go to an  $f/4$  system. Doubling the number of pixels on the focal plane is not out of the question. Mega-pixel single band IR focal planes are being manufactured and tested. It is only a matter of time or a need such as the dual IR band CTIS, to drive the dual IR band focal planes into the mega-pixel regime.

## CHAPTER 6

### CONCLUSIONS AND FUTURE WORK

#### 6.1. CONCLUSIONS

Both objectives of this work were achieved. We demonstrated the feasibility of a dual visible spectral band hyperspectral imaging spectrometer, and we designed a similar hyperspectral imaging spectrometer for the MWIR and LWIR spectral bands.

The dual band hyperspectral imaging spectrometer is possible given a focal plane of interwoven or stacked detectors sensitive to each band of interest. We demonstrated this by using a professional grade digital camera in the visible spectrum as part of a CTIS system. The dual band system can extend the one octave limit on CTIS or can be used for two widely separate spectral bands. During the proof of concept in the visible system, we showed that sub-voxel sampling improves the system resolution.

We have demonstrated that we can design a CGH that can cover the MWIR and LWIR regions. In general, designs that use the same number of diffraction orders in both bands perform better than mixed designs like the Ring and Hybrid patterns. We have also shown that instead of designing a CGH to phase as we have in the past, it is possible to design the CGHs to etch depth. The advantage of this technique is that we can begin using materials that have an index of refraction that is not constant over the entire spectrum.

Applying the lessons learned from the visible dual band system, we have shown that a dual band infrared system is also possible. The HgCdTe dual band IR focal planes being developed today are a perfect technological fit for this problem. Dual band QWIP arrays may be able to fill the need, as well, if there are improvements in the quantum efficiency of the detectors. The proposed dual band IR CTIS design is at the limit of current technology and plagued with aberrations. To reduce the aberrations, the state of the art dual band focal planes need to double the number of pixels to allow the system to relax from  $f/2$  to  $f/4$ .

## 6.2. FUTURE WORK

In Chapter 5 we identified discontinuities in the diffraction efficiencies of the CGH designs in LWIR (Figure 5.7). We were unable to explain these discontinuities but we noted that Jim Scholl had similar results in his work.

The next logical step after this work is to build, test, and characterize a dual IR band CTIS system. As a part of the building and testing, a second order optical design is needed to limit aberrations and shrink the system spot size. A cost analysis between a reflective and refractive design is needed and should be used as a part of the final design decision.

In addition to continuing the design and testing of a dual IR band system, there are three major areas that can significantly improve the system performance. The first of these is the use of centroiding to improve the system

calibration and **H**-matrix construction. Using sub-voxel sampling is a start on the way to centroiding. Centroiding involves characterizing the voxel spread function not only by its spatial extent in all diffraction orders but also characterizing its radiometric shape. We had assumed that the irradiance of the spots on the focal plane was uniform over the entire spot; but the spots really have a Gaussian irradiance pattern. By characterizing the shape of each spot in each diffraction order at each wavelength, we can specify the centroid of the spots. Using this centroid and the parameters of the Gaussian shape, we can reduce the voxel size during **H**-matrix construction and improve the overall spectral and spatial resolution of the system.

The second area of improvement related to the centroid issue is the radiometric characterization of the system. The value in each voxel of the reconstructed data cube is related to the radiometric strength of the object at that wavelength at that location. The only attempt to account for the radiometric strength of the measurement occurs during the calibration process. During calibration, we measure the strength of the calibration source at each wavelength with a radiometer and attempt to assign a radiometric value to each digital number output from the focal plane. At best, this gives a relative radiometric difference between voxels. A detailed radiometric sensitivity study of the CTIS system could help provide more significance to the value of each voxel. This would require the use of a traceable blackbody source and extensive knowledge of the focal plane.

The final area of improvement is the reconstruction routines. The EM and MART routines used in this work take on the order of minutes for each reconstruction iteration. Both reconstruction routines will multiply the noise in the  $\mathbf{H}$ -matrix for each iteration. The advantage of the CTIS system over other imaging spectrometer systems is that it is able to acquire the entire data cube in a single integration time. This makes the CTIS system perfect for dynamic scenes. The problem is we cannot get the reconstructed data cube out of the CTIS system to make it useful for most dynamic scenes. Once data cube reconstruction is possible on the order of a few seconds, the CTIS system will begin replacing conventional systems.

The systems tested and designed in this work were done so for the purpose of understanding the dual band CTIS problem. The dual IR band CTIS design presented is a good first order general use design. For a particular use of the dual IR band CTIS, the design parameters can be modified and engineering trade-offs used to optimize the system for its designed purpose. For example, the spatial resolution, spectral resolution, and field of view specifications were arbitrary. The work done to achieve those parameters and the criteria used to optimize the system given those design parameters should be re-evaluated when designing a follow-on system.

## APPENDIX A

### LINEAR SHIFT INVARIANCE

During the  $\mathbf{H}$ -matrix construction, we assume that the voxel spread function is linear and shift invariant with respect to the source placement inside the field stop. We must examine under what conditions that assumption is valid. We start with the Fraunhofer approximations for a clear aperture, then place an ideal lens in the aperture, and finally add aberrations to the lens.

We start the discussion by considering a monochromatic plane wave normally incident on an open aperture. The aperture is in the plane  $z = 0$ . We denote the complex amplitude of electric field distribution with the lower case  $u$  (e.g.  $u(\mathbf{r}) = E_x(\mathbf{r})$ ). Then, by invoking the Kirchhoff boundary conditions, we can say that the complex amplitude in the plane of the aperture is the complex amplitude of the field incident on the aperture multiplied by the aperture function,  $t_{ap}(\mathbf{r})$ .

$$u_0(\mathbf{r}) = u_{inc}(\mathbf{r})t_{ap}(\mathbf{r}) \quad (\text{A.1})$$

The aperture function is equal to one for the clear aperture and zero where the light is blocked. In an observation plane  $z$ , where  $z \gg a^2/\lambda$  when  $a$  is the radius of the circle that encompasses the clear aperture, we express the electric field complex amplitude as:

$$u(\mathbf{r}_z) \approx \frac{\exp(ikz)}{i\lambda z} \exp\left(i\pi \frac{r^2}{\lambda z}\right) \mathcal{F}_2\{u_0(\mathbf{r}')\}_{\rho=r/\lambda z} \quad (\text{A.2})$$

where  $k = 2\pi/\lambda$  and  $\mathcal{F}_2$  is the two dimensional Fourier transform. We replace the Fourier frequency space variables by  $\boldsymbol{\rho} = \mathbf{r}_z/\lambda z$  to get the transform back to the space domain. We use the subscript  $z$  for vectors in the observation plane and  $\mathbf{r}$  with no subscript is the vector in the aperture plane. We use the subscript 0 for vectors in the object plane and  $\mathbf{r}'$  is the variable of integration or transform variable. Equation (A.2) is referred to as the Fraunhofer diffraction model.

Now, place an ideal lens in the same aperture. We model the effect of the lens as changing the phase of the incident light without changing the light's amplitude. Therefore, we write the complex amplitude transmittance of an ideal lens as:

$$t_{ideal}(\mathbf{r}) = \exp[i\Phi_{ideal}(\mathbf{r})]t_{ap}(\mathbf{r}). \quad (\text{A.3})$$

An ideal lens takes an incoming plane wave propagating parallel to the optical axis and changes it to a spherical wave that converges to a point. The point the incident plane waves converges to is the focal length,  $f$ , of the lens. The focal length of the lens is then also the radius of curvature of the converging spherical wave. This allows us to rewrite equation (A.3) as:

$$t_{ideal}(\mathbf{r}) = \exp(-ikR_f)t_{ap}(\mathbf{r}) \quad (\text{A.4})$$

where  $R_f = \sqrt{r^2 + f^2}$ . We expand  $R_f$  as:

$$R_f = \sqrt{r^2 + f^2} = f + \frac{r^2}{2f} - \frac{r^4}{8f^3} + \dots \quad (\text{A.5})$$

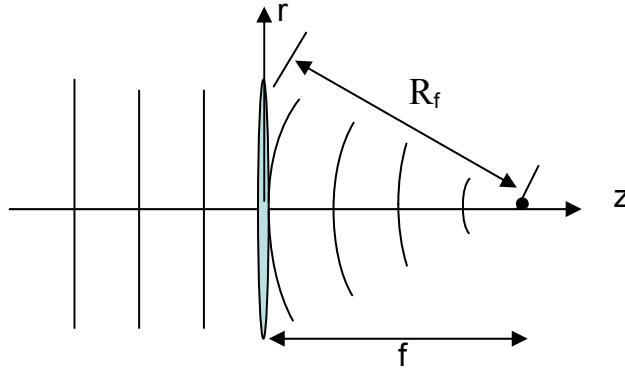


Figure A.1: Plane wave incident on an ideal lens produces a spherical wave with radius  $R_f$  that converges at the focal point of the lens

Because  $R_f$  is a phase term, it is not good enough to ignore factors based on relative size but to consider the strength of the term relative to zero. Therefore, we should only keep terms in the expansion that are much less than  $\pi/4$ . In order to ignore the quadratic term:

$$\frac{kr^4}{8f^3} \ll \frac{\pi}{4} \Rightarrow \frac{kr}{64} \left( \frac{1}{f/\#} \right)^3 \ll \frac{\pi}{4} \Rightarrow f/\# \gg \left( \frac{kr}{16\pi} \right)^{1/3} \quad (\text{A.6})$$

where  $f/\#$  is the focal length divided by the diameter of the entrance pupil.

Equation (A.4) then becomes:

$$t_{ideal}(\mathbf{r}) \approx \exp(-ikf) \exp\left(-i\pi \frac{r^2}{\lambda f}\right) t_{ap}(\mathbf{r}). \quad (\text{A.7})$$

From equation (A.7), we see that an ideal lens adds a quadratic phase factor to the aperture. For the remainder of this discussion, we ignore the first exponential

phase factor because it is a constant and will have no impact on the remaining discussion. We then define an ideal lens phase factor as:

$$\Phi_{ideal} = -\pi \frac{r^2}{\lambda f}. \quad (\text{A.8})$$

To determine whether or not the system is shift invariant, consider the effects of monochromatic point sources imaged through the system. We start by placing a monochromatic point source on axis at a point  $z = -p$ . We place the observation plane at a point  $z = q$ , where  $p$  and  $q$  are related by the lens makers' equation:

$$\frac{1}{p} + \frac{1}{q} = \frac{1}{f}. \quad (\text{A.9})$$

Propagating the spherical wave from the source to the lens, the electric field is:

$$u_{inc}(\mathbf{r}) = \frac{A}{R_p} \exp(ikR_p) \quad (\text{A.10})$$

where  $A$  is the strength of the source and  $R_p = \sqrt{r^2 + p^2}$ . Again, we expand  $R_p$  as in equation (A.5). We keep the first two terms of the expansion in the exponential if:

$$\frac{kr^4}{8p^3} \ll \frac{\pi}{4}. \quad (\text{A.11})$$

We let  $R_p \approx p$  in the denominator of equation (A.10) and rewrite equation (A.10) as:

$$u_{inc}(\mathbf{r}) = \frac{A}{p} \exp(ikp) \exp\left(i\pi \frac{r^2}{\lambda p}\right) \quad (\text{A.12})$$

Then the complex amplitude just after the ideal lens is the incident complex amplitude times the transmittance of the lens:

$$u_{ideal}(\mathbf{r}) = \frac{A}{p} \exp(ikp) \exp\left(i\pi \frac{r^2}{\lambda p}\right) \exp\left(-i\pi \frac{r^2}{\lambda f}\right) t_{ap}(\mathbf{r}). \quad (\text{A.13})$$

By using the lens maker's equation we simplify equation (A.13) to:

$$u_{ideal}(\mathbf{r}) = \frac{A}{p} \exp(ikp) \exp\left(-i\pi \frac{r^2}{\lambda q}\right) t_{ap}(\mathbf{r}). \quad (\text{A.14})$$

By using the Fraunhofer diffraction model of equation (A.2) where  $u_0$  is now  $u_{ideal}$ , we determine the complex amplitude at the image plane  $z = q$ .

$$u(\mathbf{r}_{z=q}) = \frac{1}{i\lambda q} \exp(ikq) \exp\left(-i\pi \frac{r^2}{\lambda q}\right) \left[ \mathcal{F}_2 \left\{ \exp\left(i\pi \frac{r'^2}{\lambda q}\right) u_{ideal}(\mathbf{r}') \right\} \right]_{\mathbf{p}=\mathbf{r}/\lambda q} \quad (\text{A.15})$$

By making the substitution of equation (A.14) into (A.15) we see that the quadratic phase term inside the Fourier transform exactly cancel and we have:

$$u(\mathbf{r}_{z=q}) = \frac{A}{i\lambda pq} \exp(ik(p+q)) \exp\left(i\pi \frac{r_{z=q}^2}{\lambda q}\right) \mathcal{T}_{ap} \left( \frac{\mathbf{r}_{z=q}}{\lambda q} \right). \quad (\text{A.16})$$

where  $\mathcal{T}_{ap}$  is the two-dimensional Fourier transform of the aperture function  $t_{ap}$ .

Now consider a point source off-axis in the plane  $z = -p$  at the point  $\mathbf{r}_0$ .

The complex amplitude at the point  $\mathbf{r}$  incident on the lens from a point source at point  $\mathbf{r}_0$  is:

$$u_{inc-off}(\mathbf{r}) = \frac{A}{R_p} \exp\left(2\pi i \frac{R_p}{\lambda}\right). \quad (\text{A.17})$$

Again, we expand  $R_p$  and if:

$$\frac{k|\mathbf{r} - \mathbf{r}_0|^2}{8p^3} \ll \frac{\pi}{4} \quad (\text{A.18})$$

we approximate:

$$R_p \approx p + \frac{|\mathbf{r} - \mathbf{r}_0|^2}{2p} + \dots \quad (\text{A.19})$$

We keep the first order approximation for  $R_p$  in the denominator of the amplitude and both the first and second order term in the phase following the assumption in equation (A.6) as shown in (A.18). If we incorporate the first order phase term into the amplitude,  $A$ , then equation (A.17) becomes:

$$u_{inc-off}(\mathbf{r}) = \frac{A}{p} \exp\left(i\pi \frac{|\mathbf{r} - \mathbf{r}_0|^2}{\lambda p}\right). \quad (\text{A.20})$$

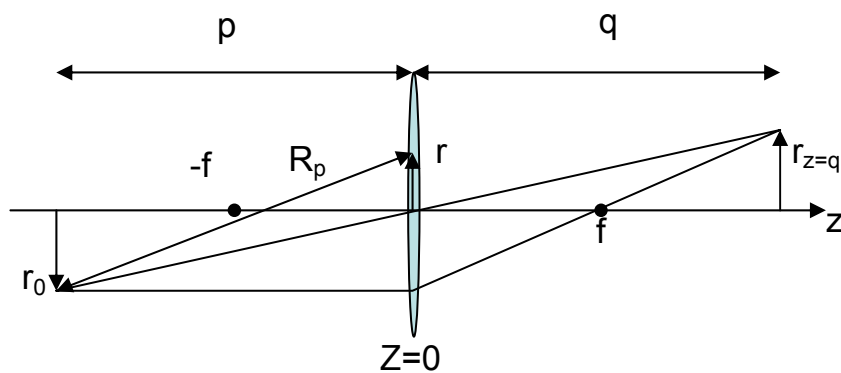


Figure A.2: Ideal lens imaging a point source in the plane  $z = -p$  at the off-axis position  $r_0$  imaged to plane  $z = q$

The complex amplitude transmittance on the image side of the ideal lens becomes:

$$u_{ideal-off}(\mathbf{r}) = \frac{A}{p} \exp\left(i\pi \frac{|\mathbf{r} - \mathbf{r}_0|^2}{\lambda p}\right) \exp\left(-i\pi \frac{r^2}{\lambda f}\right) t_{ap}(\mathbf{r}). \quad (\text{A.21})$$

Next, we expand the absolute value term and use the lens makers' equation, equation (A.9) to get:

$$u_{ideal-off}(\mathbf{r}) = \frac{A}{p} \exp\left(i\pi \frac{r_0^2 - 2\mathbf{r} \cdot \mathbf{r}_0}{\lambda p}\right) \exp\left(-i\pi \frac{r^2}{\lambda q}\right) t_{ap}(\mathbf{r}). \quad (\text{A.22})$$

Applying the Fraunhofer model by substituting equation (A.22) into equation (A.15) for  $u_{ideal}$ , we calculate the complex amplitude at the image plane  $z = q$ :

$$u_{off}(\mathbf{r}_{z=q}) = \frac{1}{i\lambda q} \exp(ikq) \exp\left(i\pi \frac{r_{z=q}^2}{\lambda q}\right) [\mathcal{F}_2 \left\{ \exp\left(i\pi \frac{r'^2}{\lambda q}\right) u_{ideal-off}(\mathbf{r}') \right\}]_{\rho=\mathbf{r}/\lambda q}. \quad (\text{A.23})$$

Substituting equation (A.22) into equation (A.23) we have:

$$u_{off}(\mathbf{r}_{z=q}) = \frac{A}{i\lambda p q} \exp(ikq) \exp\left(i\pi \frac{r_{z=q}^2}{\lambda q}\right) \exp\left(i\pi \frac{r_0^2}{\lambda p}\right) \\ \times [\mathcal{F}_2 \left\{ \exp\left(-i\pi \frac{2\mathbf{r}' \cdot \mathbf{r}_0}{\lambda p}\right) \exp\left(+i\pi \frac{2\mathbf{r}' \cdot \mathbf{r}_0}{\lambda p}\right) \exp\left(i\pi \frac{r'^2}{\lambda q}\right) t_{ap}(r') \right\}]_{\rho=\mathbf{r}/\lambda q} \quad (\text{A.24})$$

Again, the quadratic phase factor inside the Fourier transform cancels. Using the shift theorem of the Fourier transform and combining the constant phase factor and  $i$  in the denominator into the constant  $A$ , we have:

$$u_{off}(\mathbf{r}_{z=q}) = \frac{A}{\lambda pq} T_{ap} \left( \frac{\mathbf{r}_{z=q}}{\lambda q} + \frac{\mathbf{r}_0}{\lambda p} \right). \quad (\text{A.25})$$

By using the lateral magnification of an ideal lens:

$$m = -\frac{q}{p}. \quad (\text{A.26})$$

we rewrite equation (A.25) as:

$$u_{off}(\mathbf{r}_{z=q}) = \frac{A}{\lambda pq} T_{ap} \left[ \frac{1}{\lambda q} (\mathbf{r}_{z=q} - m\mathbf{r}_0) \right]. \quad (\text{A.27})$$

What we see from an off-axis point source is the exact same pattern as for the on-axis point source but shifted by a distance  $m\mathbf{r}_0/\lambda q$  as long as the assumption in equation (A.18) is valid. We can rewrite equation (A.18) as:

$$|\mathbf{r} - \mathbf{r}_0|^4 \ll \lambda p^3 \quad (\text{A.28})$$

and we conclude that an ideal lens is shift invariant with respect to the source position in the object plane.

Now consider a lens with aberrations. For this work, we only consider the Seidel aberrations in examining our shift invariant assumption for the CTIS system. We have stated that an ideal lens has the effect of adding a quadratic phase term to the incident wave front. Aberrations add another, possibly undesired, phase term to the wavefront. We can model the phase imparted by an aberrated lens as:

$$\Phi_{lens}(\mathbf{r}, \mathbf{r}_0) = \Phi_{ideal}(\mathbf{r}) + kW(\mathbf{r}, \mathbf{r}_0) \quad (\text{A.29})$$

where  $\Phi_{ideal}$  is defined in equation (A.8),  $k$  is the wavenumber, and  $W$  is wavefront error due to the aberrations. The aberrations are a function of both the field coordinates of the source,  $\mathbf{r}_0$ , and the pupil coordinates,  $\mathbf{r}$ . The wavefront errors for each of the Seidel aberrations are:

Field Curvature:  $W(\mathbf{r}, \mathbf{r}_0) = w_{220} r_0^2 r^2$

Distortion:  $W(\mathbf{r}, \mathbf{r}_0) = w_{311} r_0^3 r \cos(\theta - \theta_0) = w_{311} r_0^2 (\mathbf{r} \cdot \mathbf{r}_0)$

Spherical:  $W(\mathbf{r}, \mathbf{r}_0) = w_{040} r^4$

Coma:  $W(\mathbf{r}, \mathbf{r}_0) = w_{131} r_0 r^3 \cos(\theta - \theta_0) = w_{311} r^2 (\mathbf{r} \cdot \mathbf{r}_0)$

Astigmatism:  $W(\mathbf{r}, \mathbf{r}_0) = w_{222} r_0^2 r^2 [\cos(\theta - \theta_0)]^2 = w_{222} (\mathbf{r} \cdot \mathbf{r}_0)^2$

The  $w$  coefficients are signed constants that represent the strength of each aberration.

Consider the lens phase with only field curvature aberrations. The phase imparted by a lens with only field curvature gives:

$$\Phi_{lens}(\mathbf{r}, \mathbf{r}_0) = \Phi_{ideal}(\mathbf{r}) + k w_{220} \mathbf{r}^2 \mathbf{r}_0^2 \equiv -\frac{\pi r^2}{\lambda f_{eff}(r_0)} \quad (\text{A.30})$$

where  $f_{eff}$  is an effective focal length of the aberrated lens. We now solve for the inverse of the effective focal length:

$$\frac{1}{f_{eff}(r_0)} = \frac{1}{f} - 2w_{220} r_0^2. \quad (\text{A.31})$$

Using the lens makers, equation, equation (A.9), we can relate the image and object plane. Equation (A.32) shows that the image plane has a field dependence:

$$\frac{1}{f_{eff}(r_0)} = \frac{1}{p} + \frac{1}{q(r_0)}. \quad (\text{A.32})$$

Solving equation (A.32) for the image plane,  $q$ , yields:

$$q = \frac{fp}{p-f} \quad (\text{A.33})$$

and the lateral magnification from equation (A.26) can be rewritten as:

$$m = \frac{f}{f-p}. \quad (\text{A.34})$$

Then, using  $f_{eff}$  in equation (A.34) we have an effective magnification:

$$m_{eff} = \frac{1 - 2fw_{220}r_0^2}{pf - 1 + 2fw_{220}r_0^2}. \quad (\text{A.35})$$

We now substitute the effective lateral magnification from equation (A.35) into equation (A.27) and solve for the electric field in the image plane due to an off-axis monochromatic point source:

$$u_{off}(\mathbf{r}_{z=q}) = \frac{A}{\lambda pq} T_{ap} \left[ \frac{1}{\lambda q} \left( \mathbf{r}_{z=q} - \left( \frac{1 - 2fw_{220}r_0^2}{pf - 1 + 2fw_{220}r_0^2} \right) \mathbf{r}_0 \right) \right]. \quad (\text{A.36})$$

For an ideal lens, we saw that the magnification is a constant value. For a lens with field curvature, the lateral magnification is not constant for points in locations in the object plane. Therefore, a lens with field curvature is not shift invariant.

Now consider the lens with only spherical aberration. We repeat the process with the phase of the lens with spherical aberration given as:

$$\Phi_{lens}(\mathbf{r}, \mathbf{r}_0) = \Phi_{ideal}(\mathbf{r}) + kw_{040}r^4 \quad (\text{A.37})$$

Setting the phase equal to  $\frac{\pi r^2}{\lambda f_{eff}}$  and solving for  $1/f_{eff}$  we have:

$$\frac{1}{f_{eff}(r)} = \frac{1}{f} - \frac{k\lambda w_{040} r^2}{\pi} \quad (\text{A.38})$$

and

$$m_{eff} = \frac{\pi - kf\lambda w_{040} r^2}{pf\pi - \pi + f\lambda w_{040} r^2}. \quad (\text{A.39})$$

Notice that for spherical aberrations there is no field dependence and the lateral magnification is a constant value, as it was for an ideal lens. Therefore, we see that a lens with only spherical aberrations is shift invariant.

If we repeated this development for the other Seidel aberrations, we would find that the aberrations that have field dependence are not, in general, shift invariant. If we start balancing aberrations, it is possible to specify field regions where there is shift invariance. If we return to the expansion and assumptions we made in equation (A.6), we set phase terms that were much less than  $\pi/4$  equal to zero and ignored them. Therefore, if we have a lens that has all of the Seidel aberrations, the phase of the lens would be:

$$\begin{aligned} \Phi_{lens}(r, r_0) = & -\frac{\pi r^2}{\lambda f} + k w_{220} r_0^2 r^2 + k w_{311} r_0^2 (r \cdot r_0) + k w_{040} r^4 \\ & + k w_{311} r^2 (r \cdot r_0) + k w_{222} (r \cdot r_0)^2. \end{aligned} \quad (\text{A.40})$$

Because each  $w$  coefficient is a signed value, we can combine two or more to sum to near zero and make the lens shift invariant.<sup>51</sup>

To apply what we have learned above to the CTIS system, we must look at the phase applied to the wavefront passing through the CGH. As we will see in Chapter 3, the CGH we use in a CTIS system is a phase only CGH and imparts a phase:

$$\Phi_{CGH} = \frac{2\pi d}{\lambda}(n_\lambda - 1) \quad (\text{A.41})$$

where  $d$  is the etch depth of the CGH and  $n_\lambda$  is the wavelength dependant index of refraction of the CGH material. From equation (A.41), we see that the phase imparted by the CGH does not have any field dependence. Therefore, the CTIS system is shift invariant as long as the optical elements have balanced the field dependent aberrations.

## APPENDIX B: CGH DESIGN RESULTS

This annex contains the plots of the diffraction efficiency of each of the desired diffraction orders as a function of wavelength. The MWIR and LWIR spectrum are plotted separately. The red line in each plot is the diffraction efficiency of the zero order.

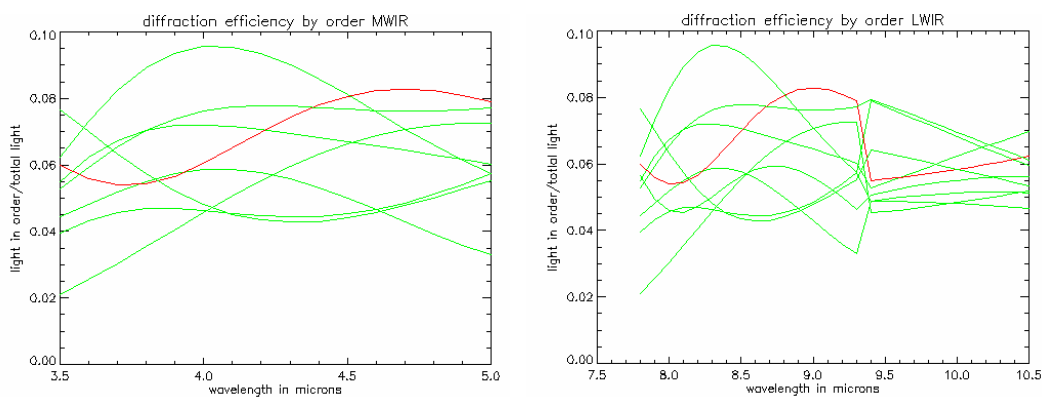


Figure B.1: Uniform 3 design pattern, 8x8 Unit Cell

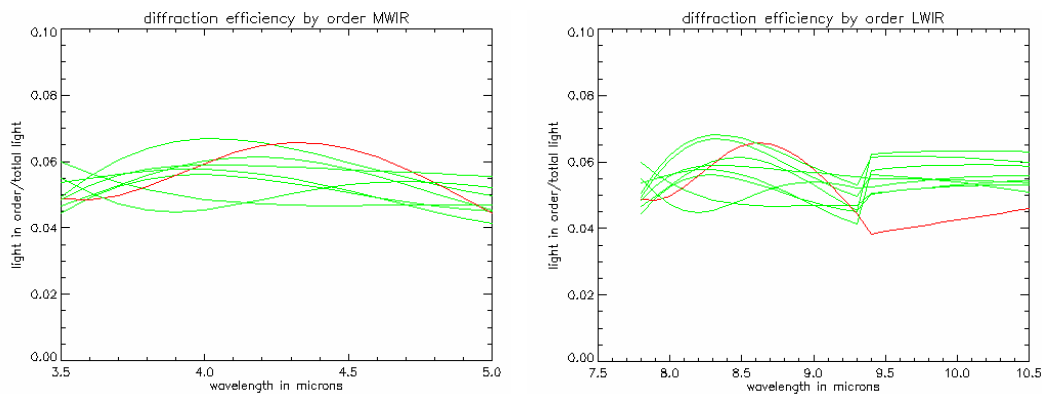


Figure B.2: Uniform 3 design pattern, 10x10 Unit Cell

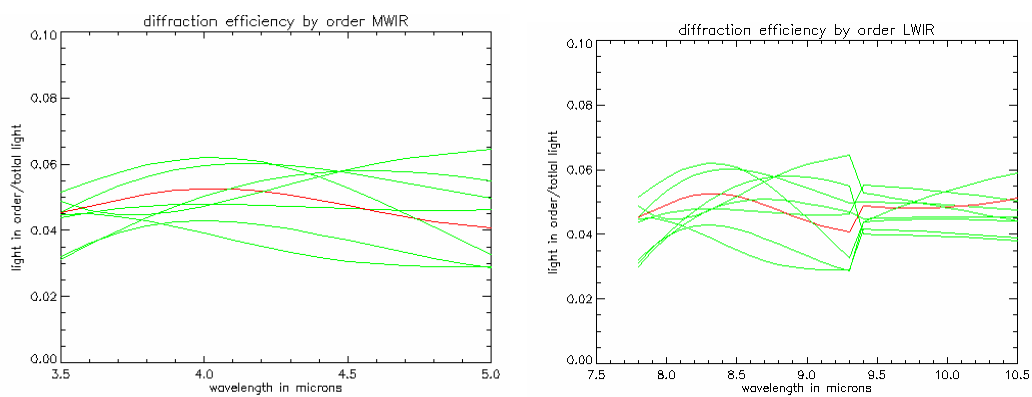


Figure B.3: Uniform 3 design pattern, 16x16 Unit Cell

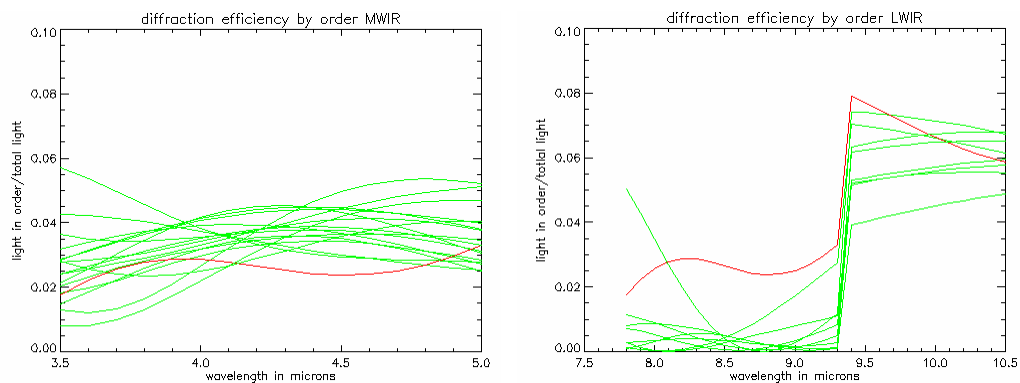


Figure B.4: Ring design pattern, 8x8 Unit Cell

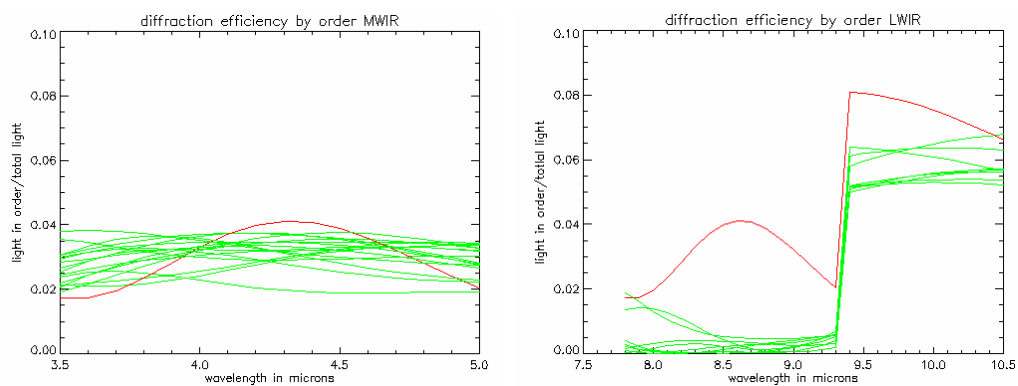


Figure B.5: Ring design pattern, 10x10 Unit Cell

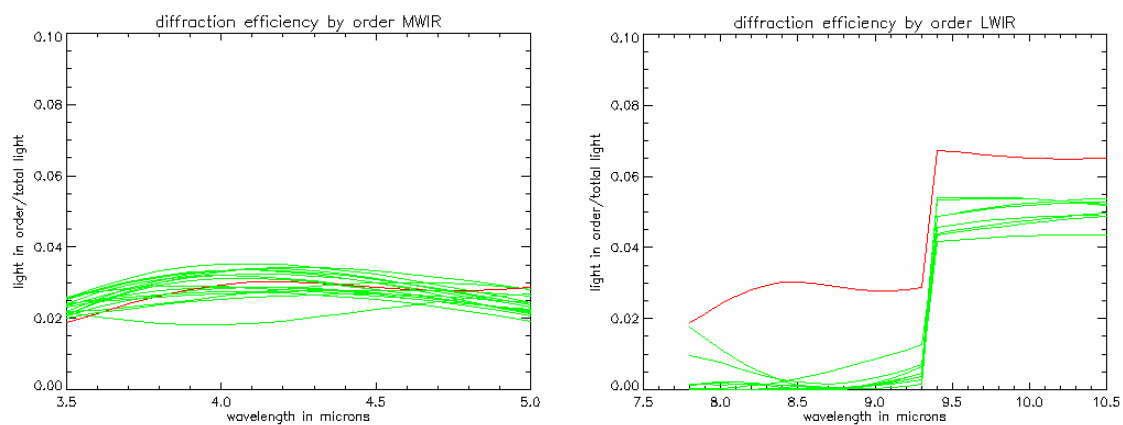


Figure B.6: Ring design pattern, 16x16 Unit Cell

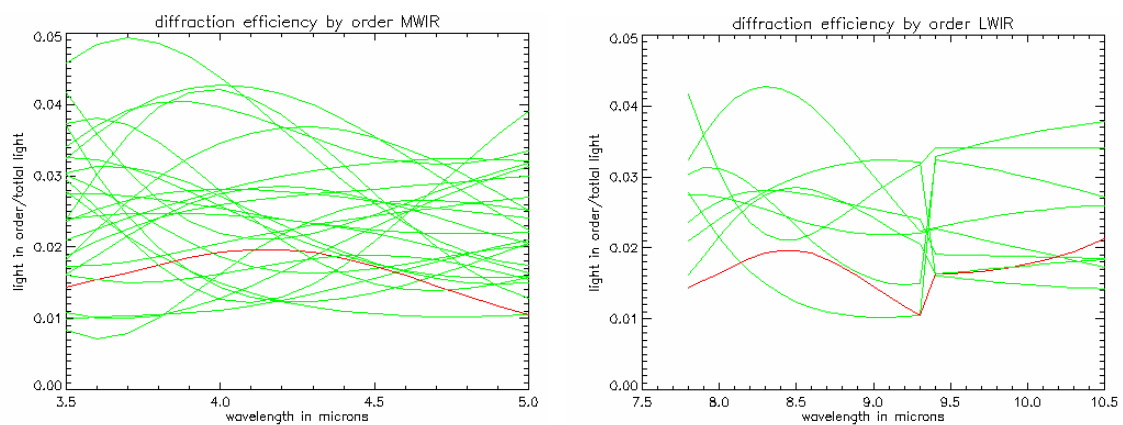


Figure B.7: Hybrid design pattern, 8x8 Unit Cell

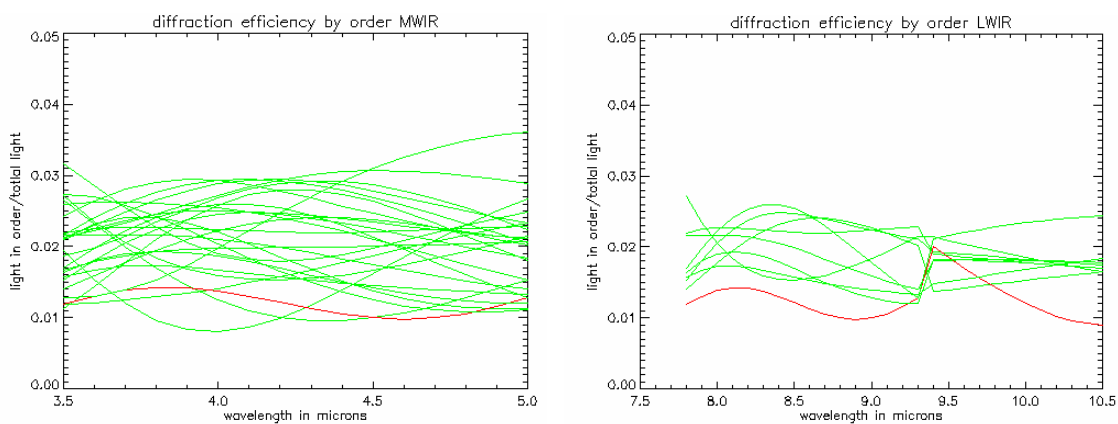


Figure B.8: Hybrid design pattern, 10x10 Unit Cell

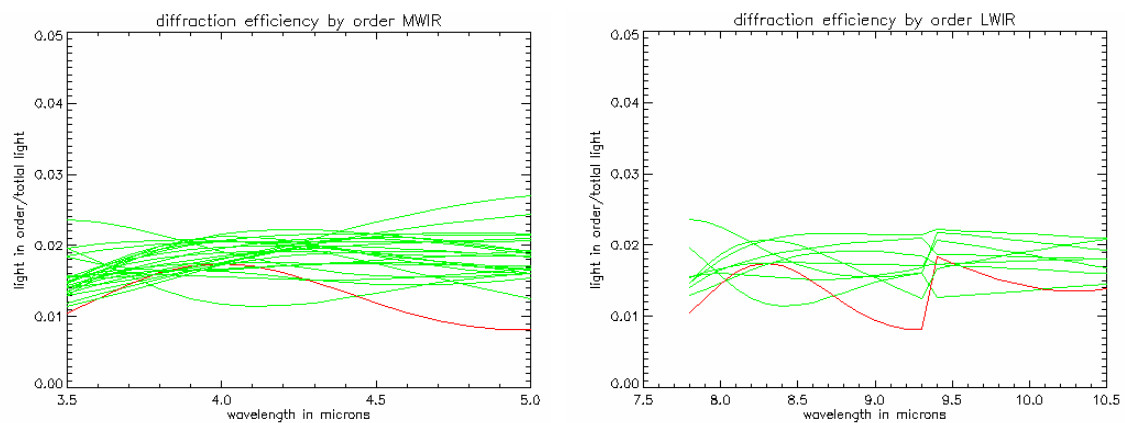


Figure B.9: Hybrid design pattern, 16x16 Unit Cell

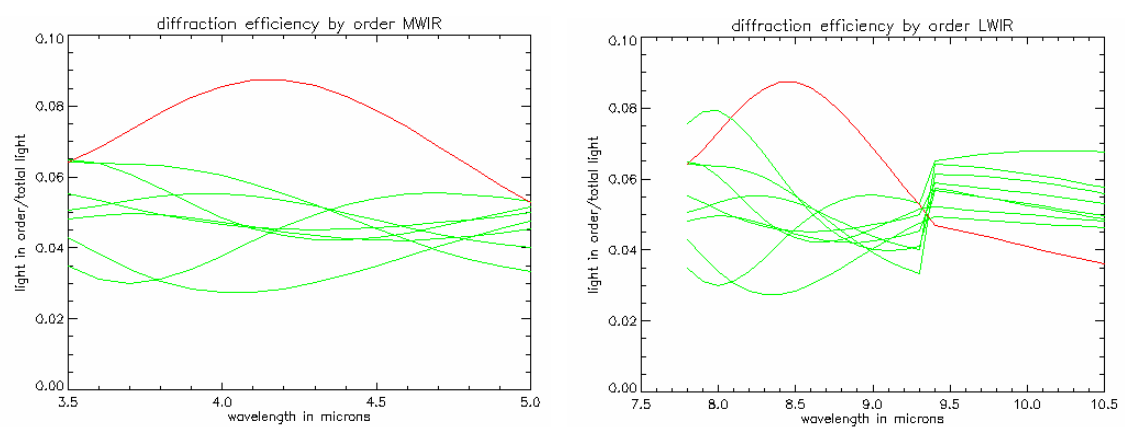


Figure B.10: Old design pattern, 8x8 Unit Cell

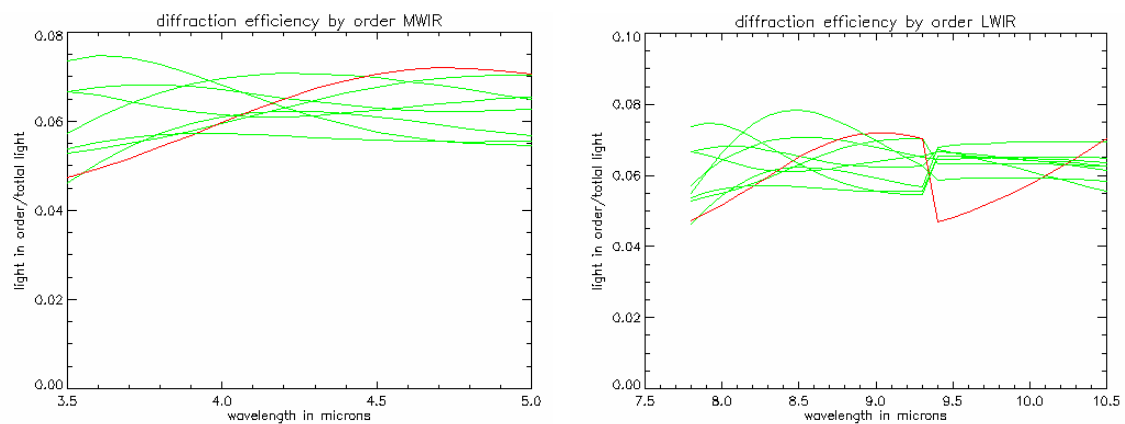


Figure B.11: Old design pattern, 10x10 Unit Cell

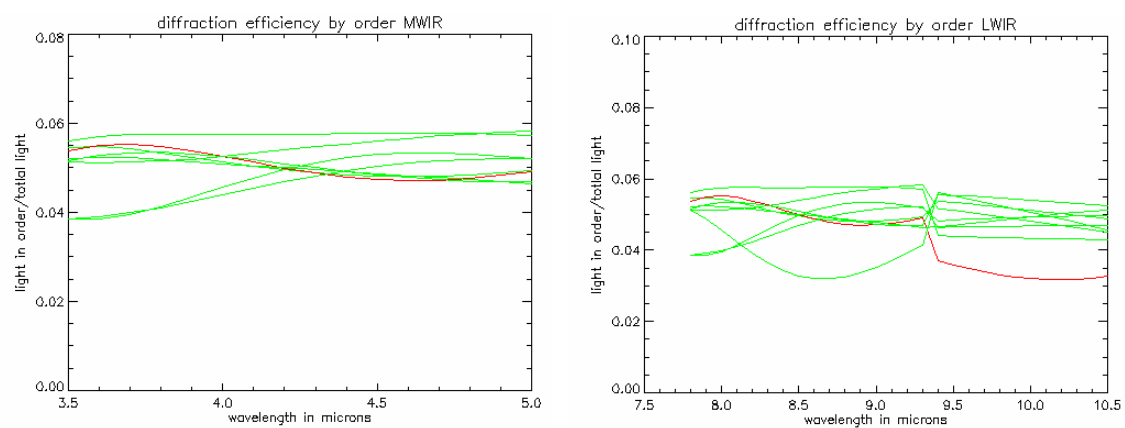


Figure B.12: Old design pattern, 16x16 Unit Cell

## APPENDIX C: VISIBLE CTIS RESULTS

Spectral output of calibration source:

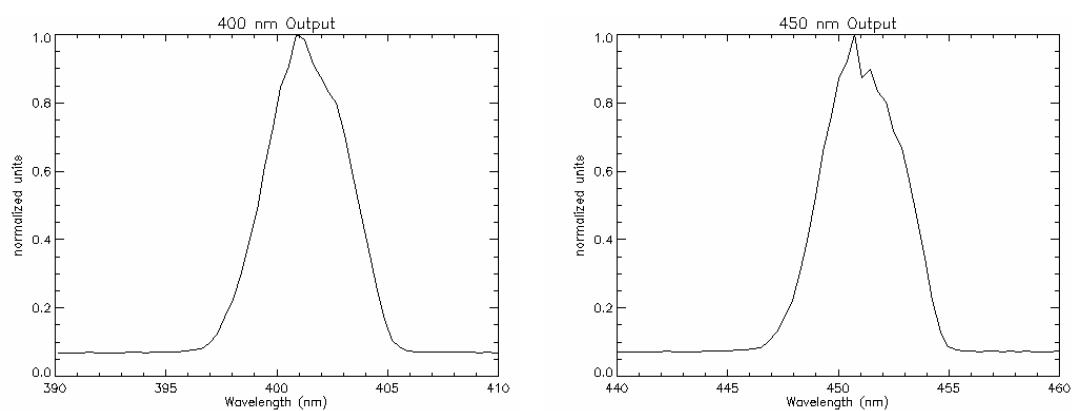


Figure C1: Calibration Source output at 400 nm. Figure C2: Calibration Source output at 450 nm

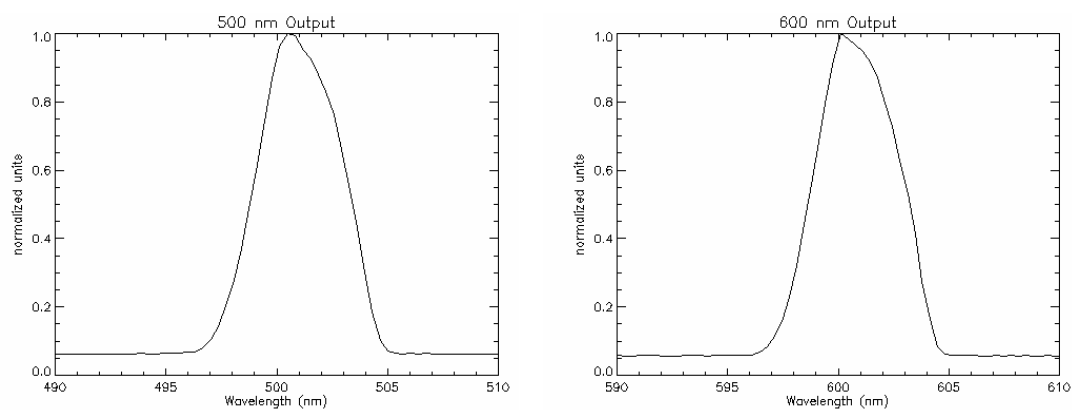


Figure C3: Calibration Source output at 500 nm. Figure C4: Calibration Source output at 600 nm

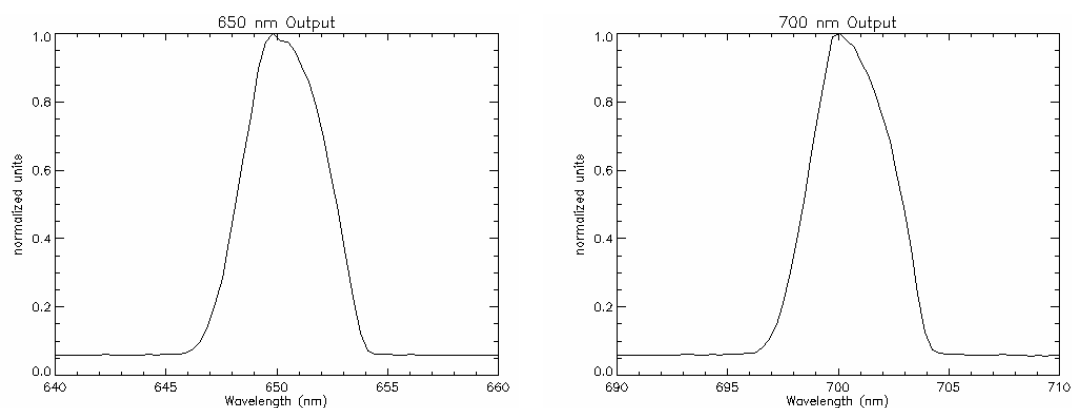


Figure C5: Calibration Source output at 650 nm. Figure C6: Calibration Source output at 700 nm

The following plots are cuts along the reconstructed data cube of the white and black bars after 4 iteration of EM. The cut is along the x-direction at  $y=42$ .

Each plot is for a given wavelength.

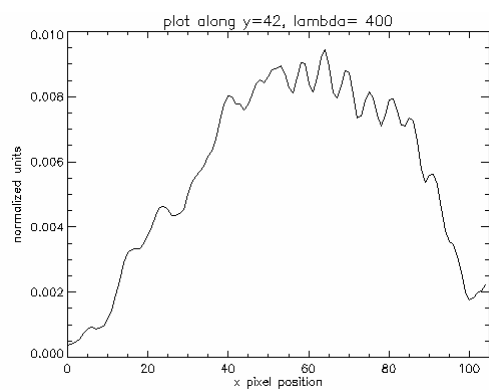


Figure C7: Black and white bars at 400 nm

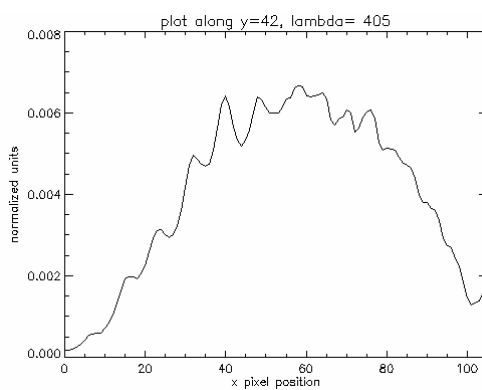


Figure C8: Black and white bars at 405 nm

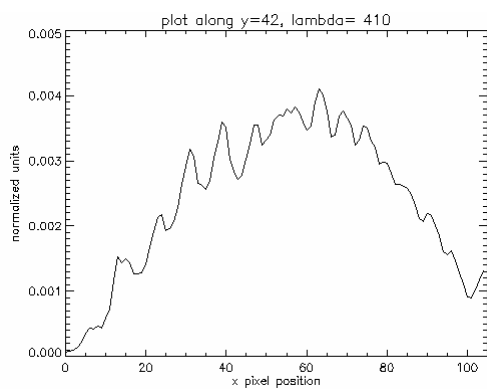


Figure C9: Black and white bars at 4100 nm

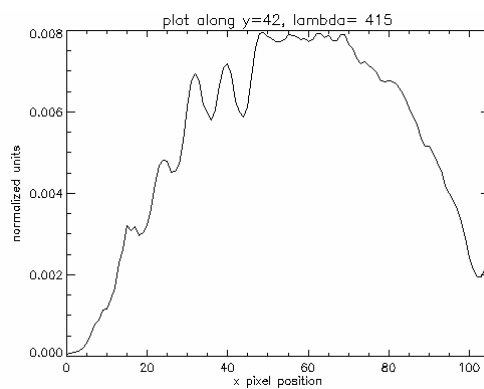


Figure C10: Black and white bars at 415 nm

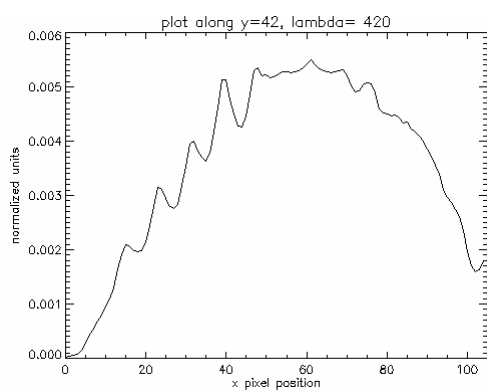


Figure C11: Black and white bars at 420 nm

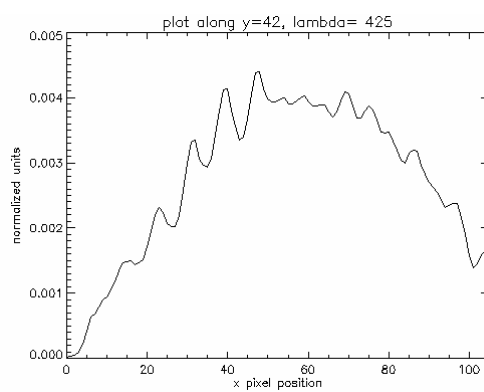


Figure C12: Black and white bars at 425 nm

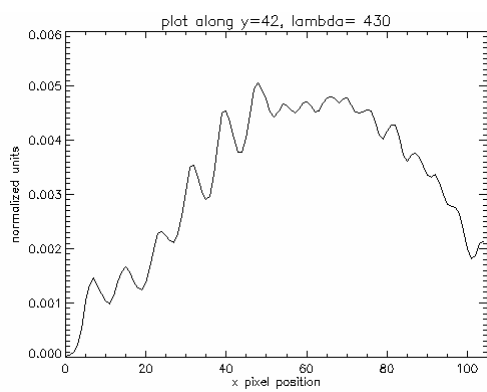


Figure C13: Black and white bars at 430 nm

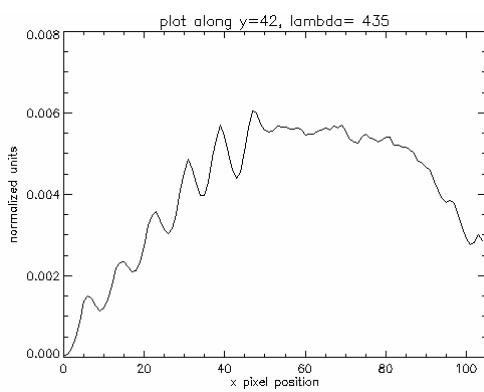


Figure C14: Black and white bars at 435 nm

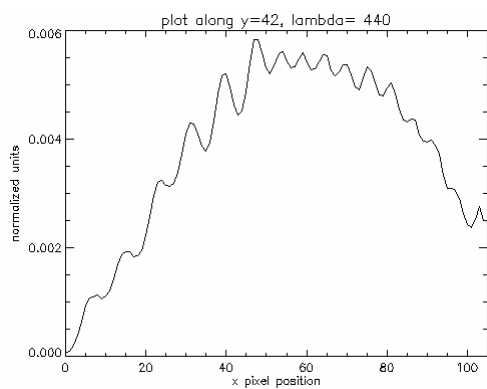


Figure C15: Black and white bars at 440 nm

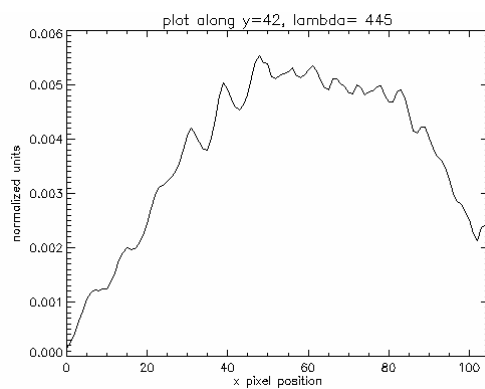


Figure C16: Black and white bars at 445 nm

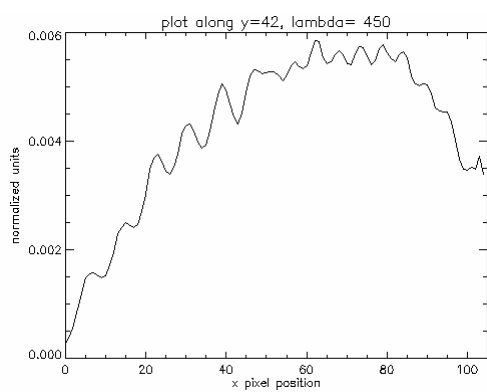


Figure C17: Black and white bars at 450 nm

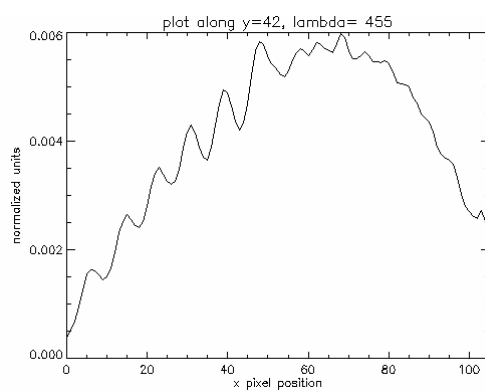


Figure C18: Black and white bars at 455 nm

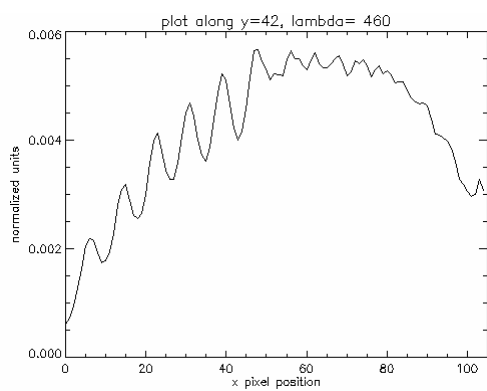


Figure C19: Black and white bars at 460 nm

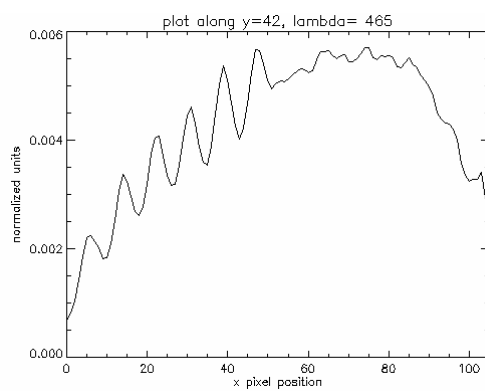


Figure C20: Black and white bars at 465 nm

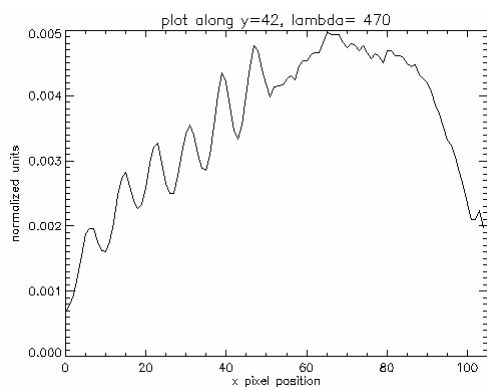


Figure C21: Black and white bars at 470 nm

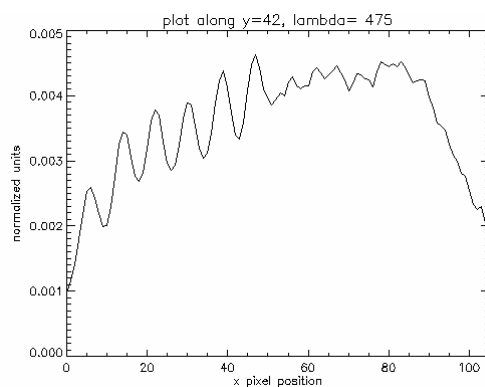


Figure C22: Black and white bars at 475 nm

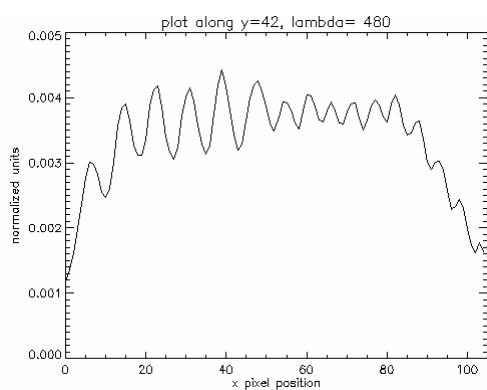


Figure C23: Black and white bars at 480 nm

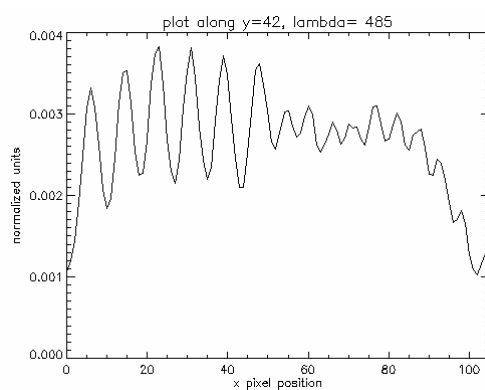


Figure C24: Black and white bars at 485 nm

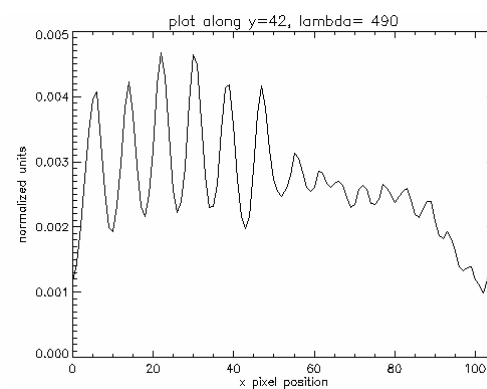


Figure C25: Black and white bars at 490 nm

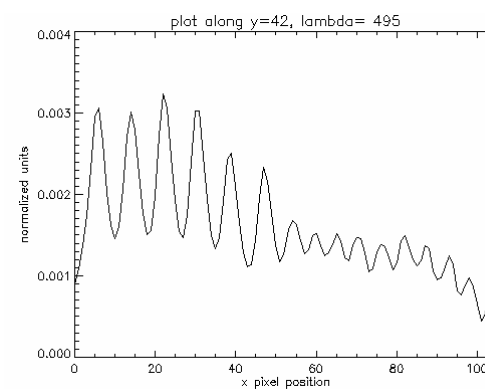


Figure C26: Black and white bars at 495 nm

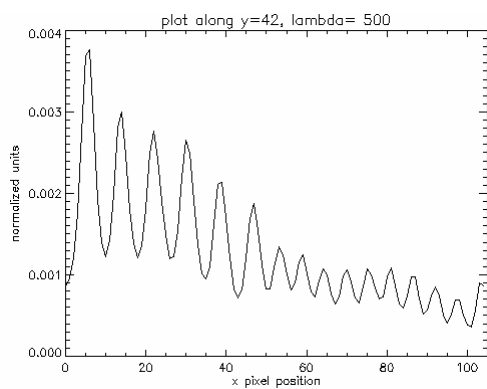


Figure C27: Black and white bars at 500 nm

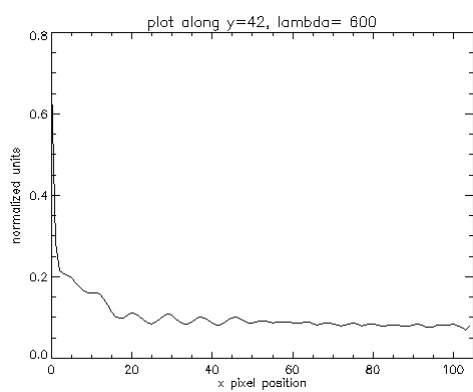


Figure C28: Black and white bars at 600 nm

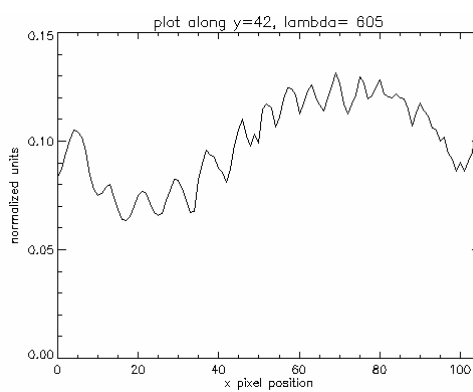


Figure C29: Black and white bars at 605 nm

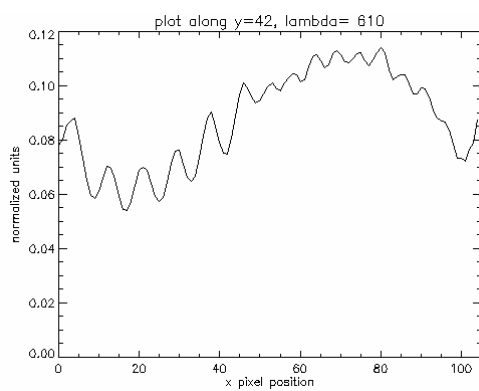


Figure C30: Black and white bars at 610 nm

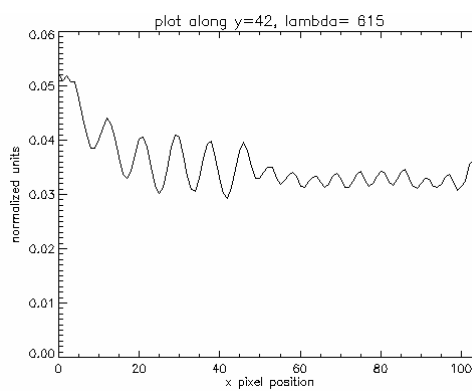


Figure C31: Black and white bars at 615 nm

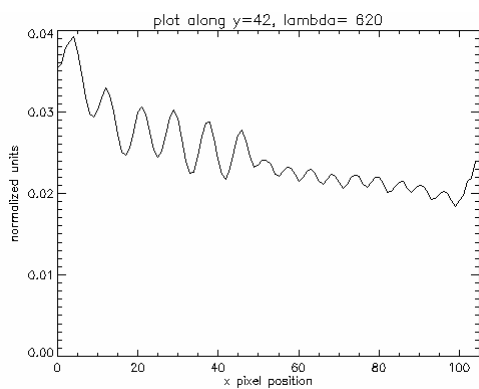


Figure C32: Black and white bars at 620 nm

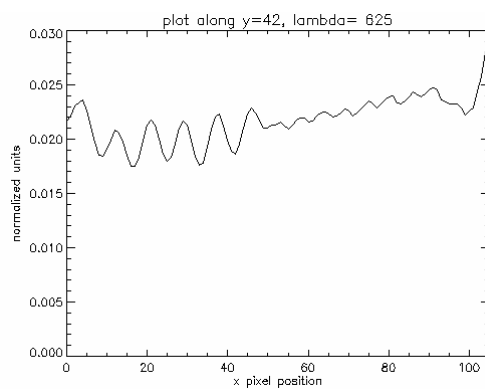


Figure C33: Black and white bars at 625 nm

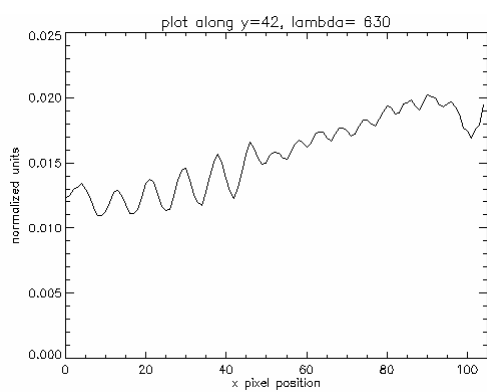


Figure C34: Black and white bars at 630 nm

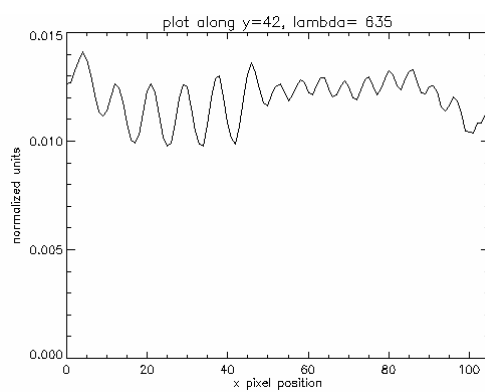


Figure C35: Black and white bars at 635 nm

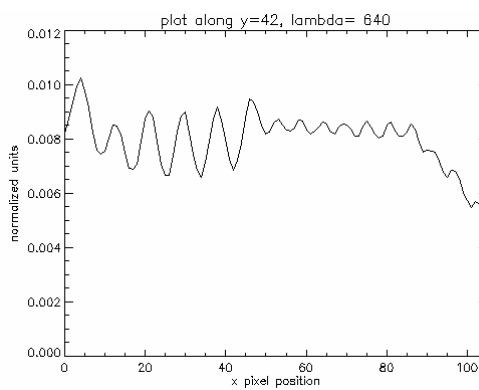


Figure C36: Black and white bars at 640 nm

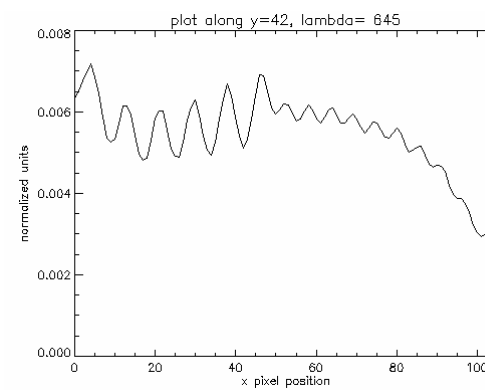


Figure C37: Black and white bars at 645 nm

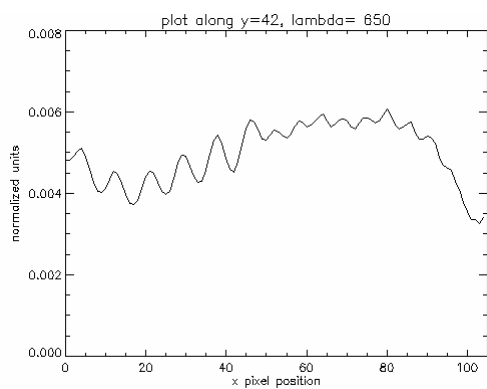


Figure C38: Black and white bars at 650 nm

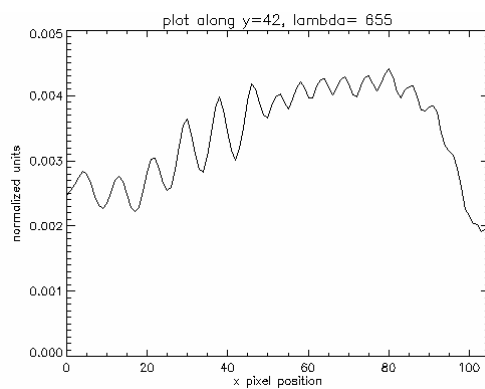


Figure C39: Black and white bars at 655 nm

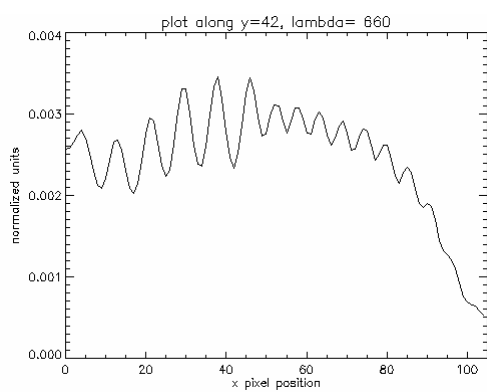


Figure C40: Black and white bars at 660 nm

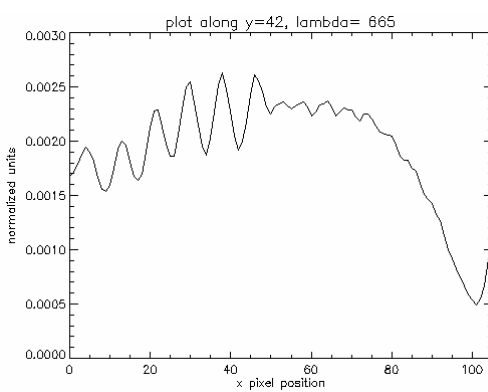


Figure C41: Black and white bars at 665 nm

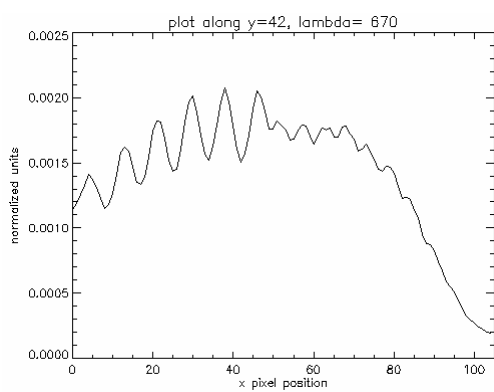


Figure C42: Black and white bars at 670 nm

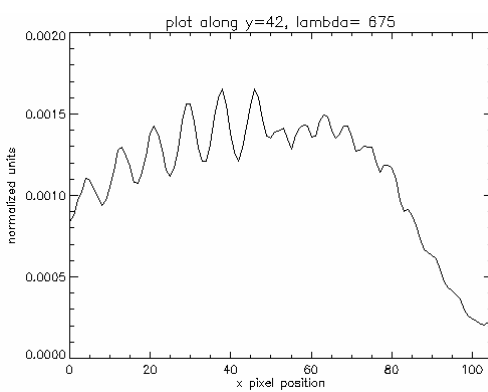


Figure C43: Black and white bars at 675 nm

The following plots are cuts along the reconstructed data cube of the red and blue bars after 4 iteration of EM. The cut is along the x-direction at  $y=42$ .

Each plot is for a given wavelength.

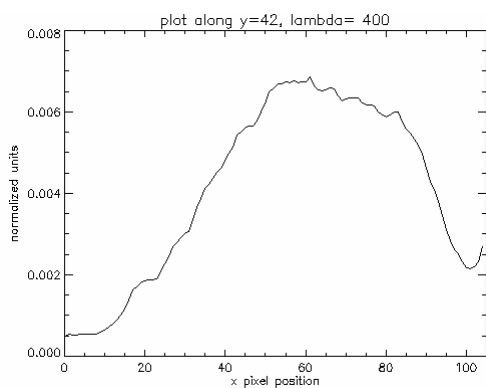


Figure C44: Red and blue bars at 400 nm

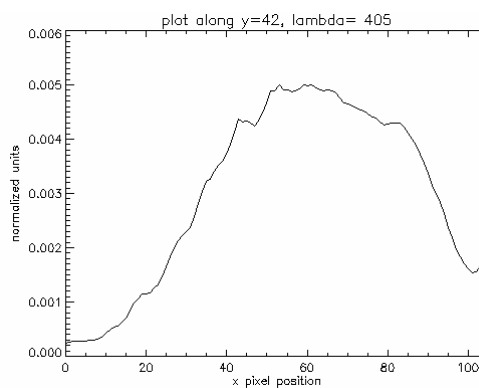


Figure C45: Red and blue bars at 405 nm

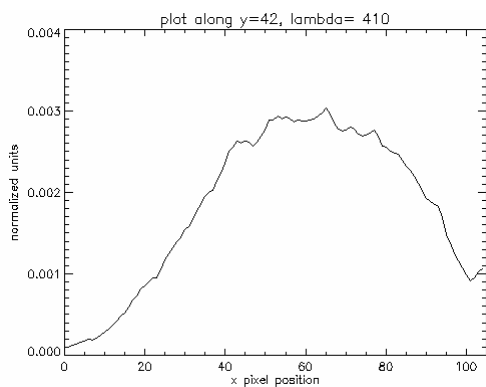


Figure C46: Red and blue bars at 410 nm

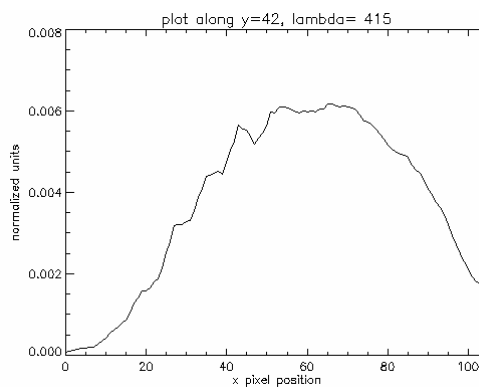


Figure C47: Red and blue bars at 415 nm

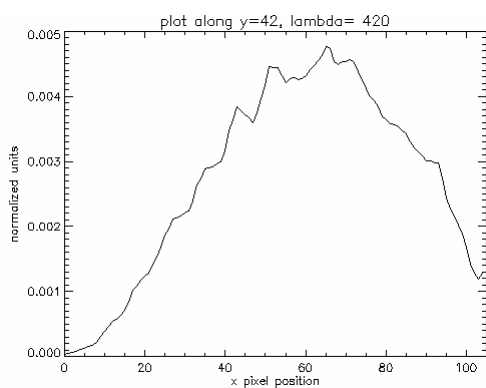


Figure C48: Red and blue bars at 420 nm

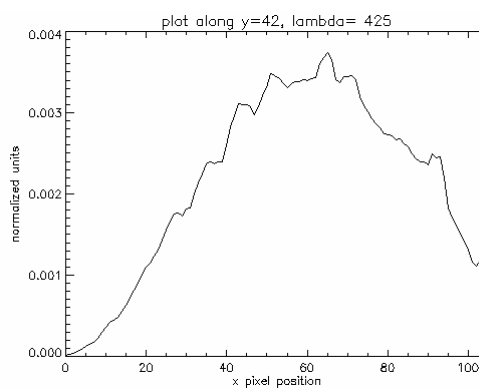


Figure C49: Red and blue bars at 425 nm

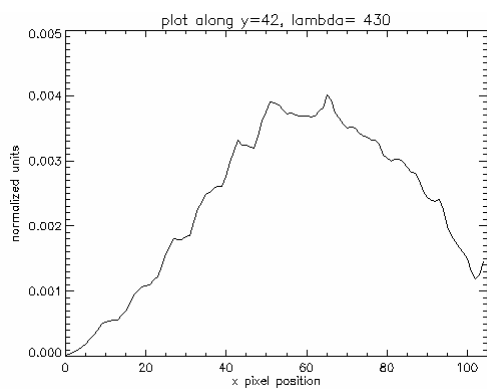


Figure C50: Red and blue bars at 430 nm

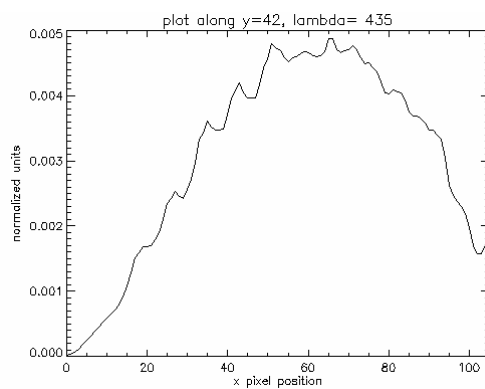


Figure C51: Red and blue bars at 435 nm

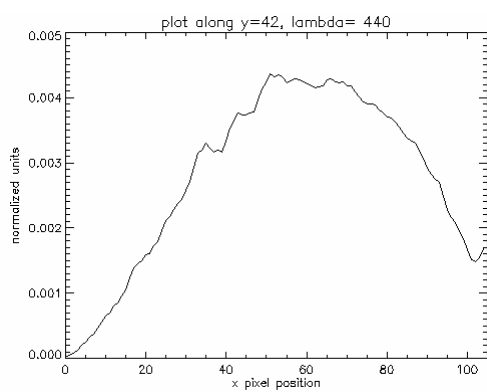


Figure C52: Red and blue bars at 440 nm

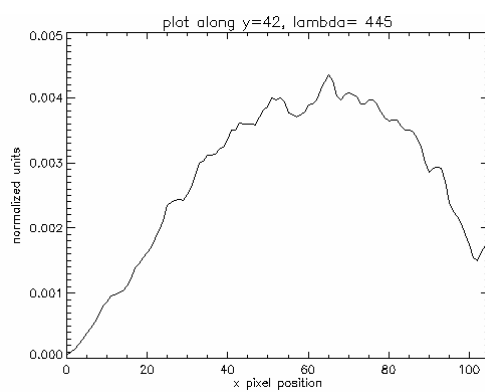


Figure C53: Red and blue bars at 445 nm

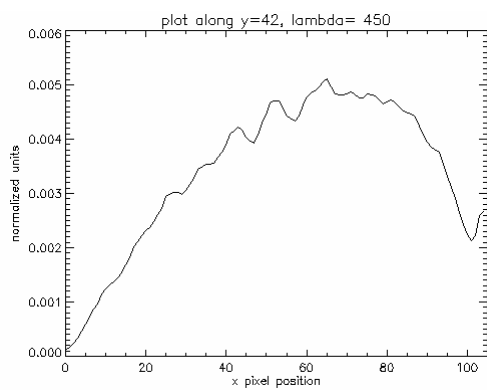


Figure C54: Red and blue bars at 450 nm

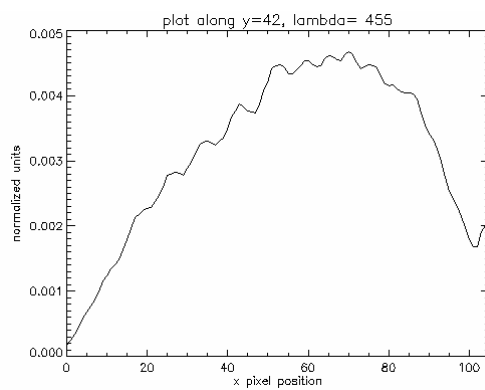


Figure C55: Red and blue bars at 455 nm

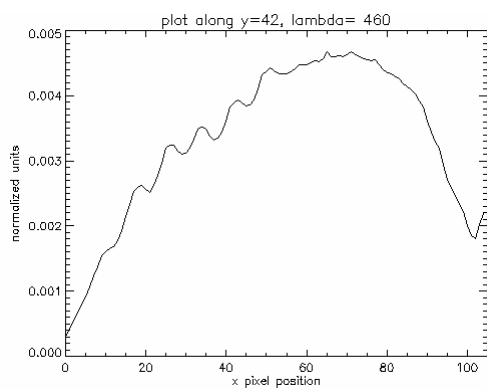


Figure C56: Red and blue bars at 460 nm

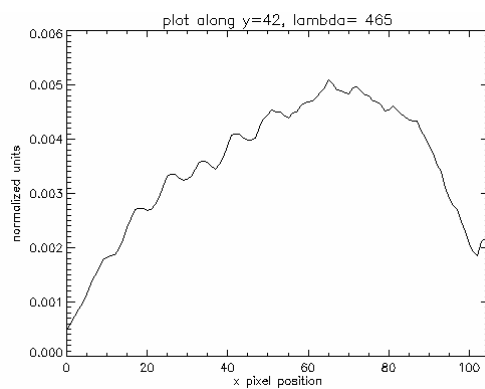


Figure C57: Red and blue bars at 465 nm

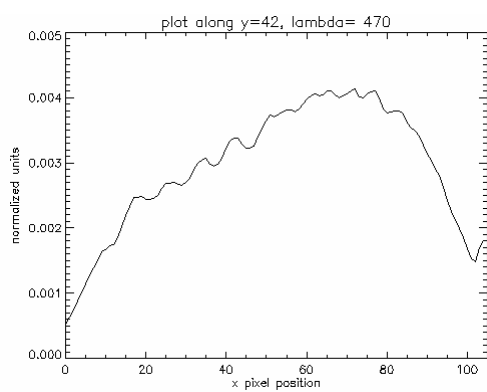


Figure C58: Red and blue bars at 470 nm

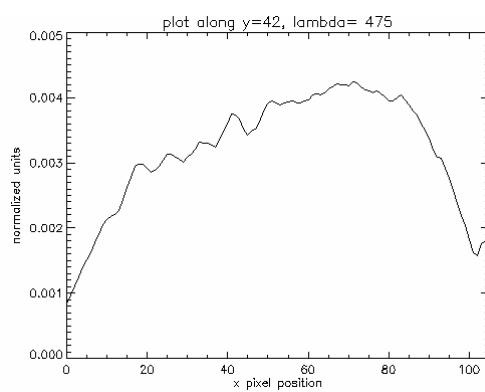


Figure C59: Red and blue bars at 475 nm

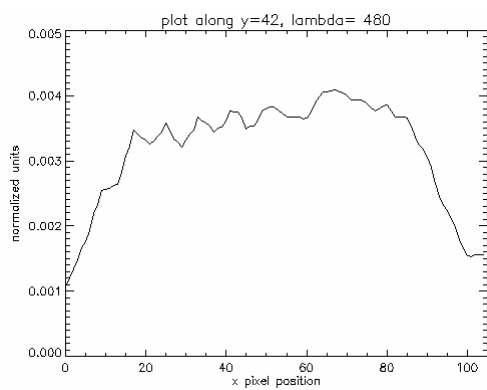


Figure C60: Red and blue bars at 480 nm

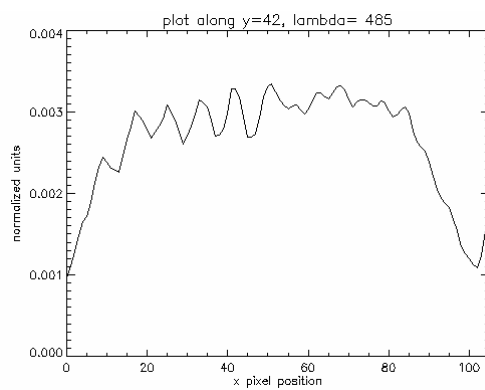


Figure C61: Red and blue bars at 485 nm

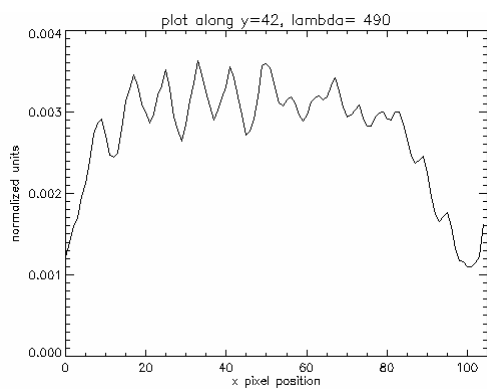


Figure C62: Red and blue bars at 490 nm

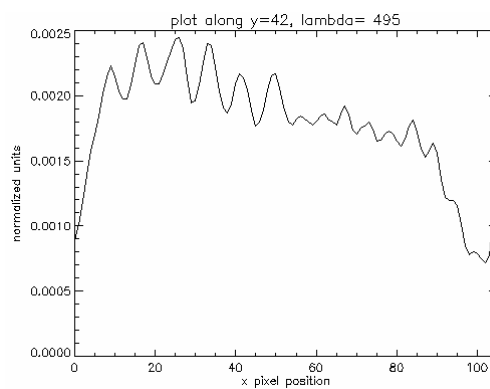


Figure C63: Red and blue bars at 495 nm

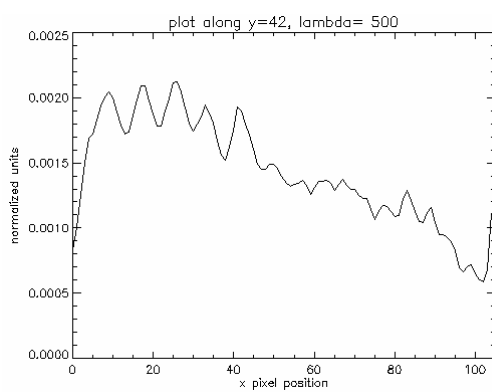


Figure C64: Red and blue bars at 500 nm

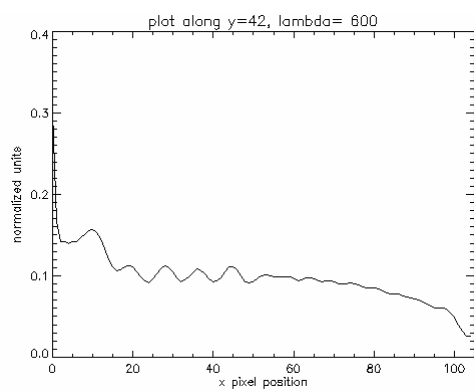


Figure C65: Red and blue bars at 600 nm

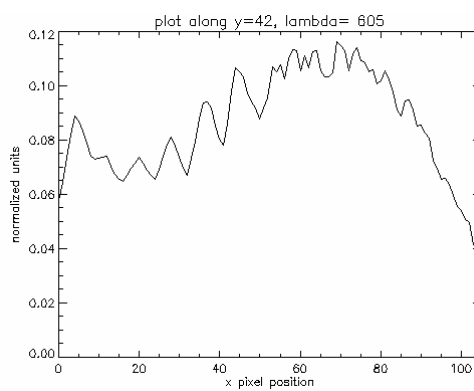


Figure C66: Red and blue bars at 605 nm

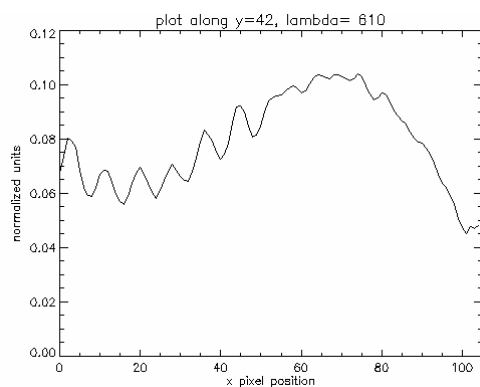


Figure C67: Red and blue bars at 610 nm

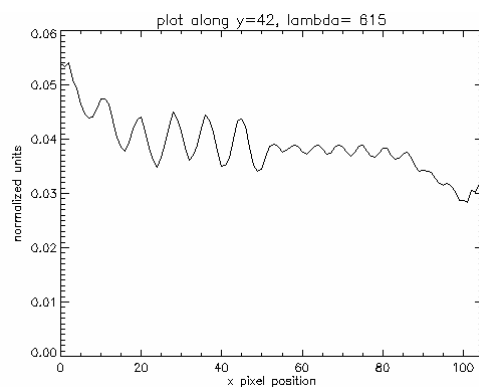


Figure C68: Red and blue bars at 615 nm

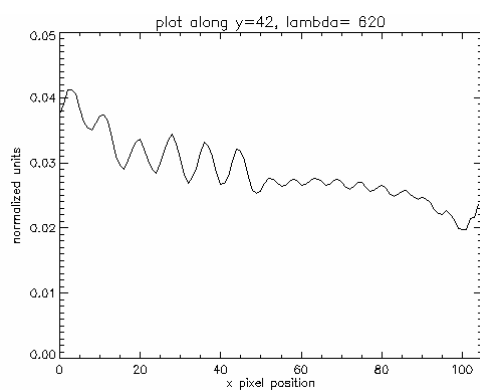


Figure C69: Red and blue bars at 620 nm

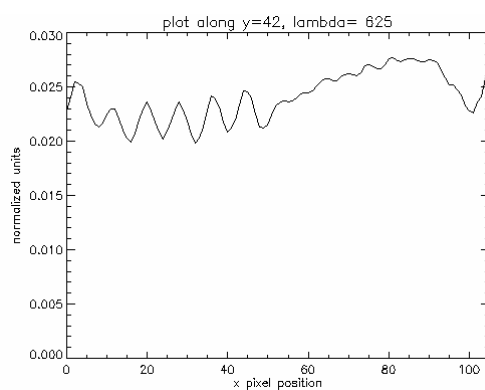


Figure C70: Red and blue bars at 625 nm

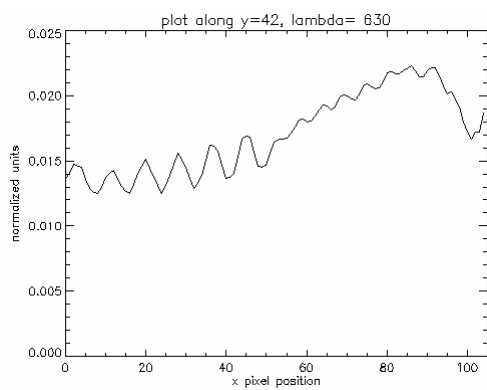


Figure C71: Red and blue bars at 630 nm

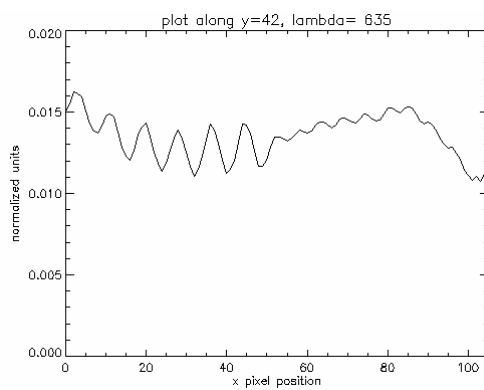


Figure C72: Red and blue bars at 635 nm

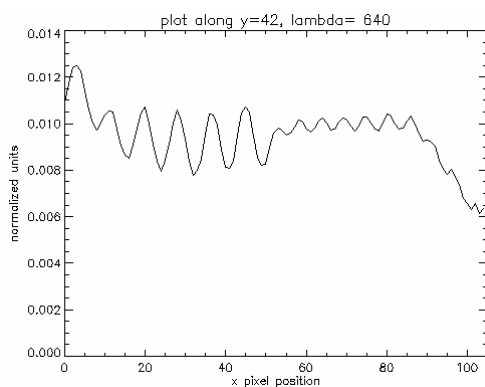


Figure C73: Red and blue bars at 640 nm

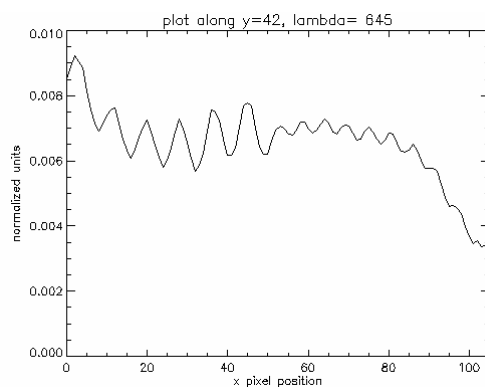


Figure C74: Red and blue bars at 645 nm

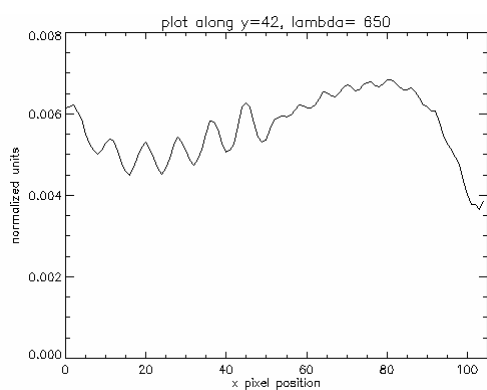


Figure C75: Red and blue bars at 650 nm

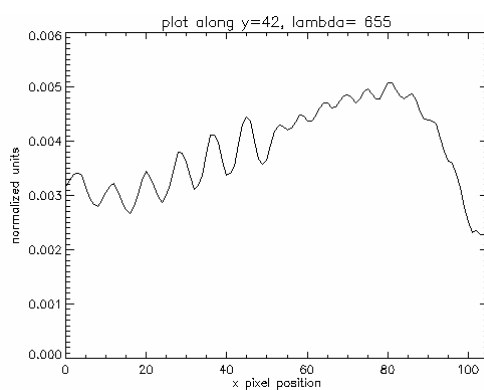


Figure C76: Red and blue bars at 655 nm

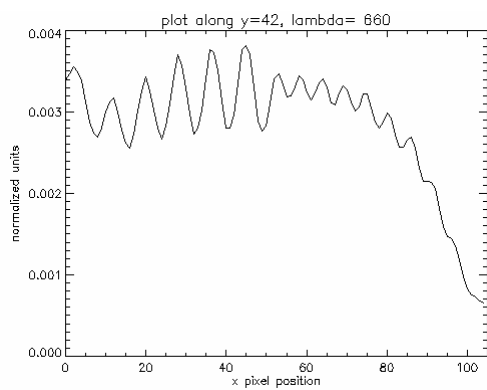


Figure C77: Red and blue bars at 660 nm

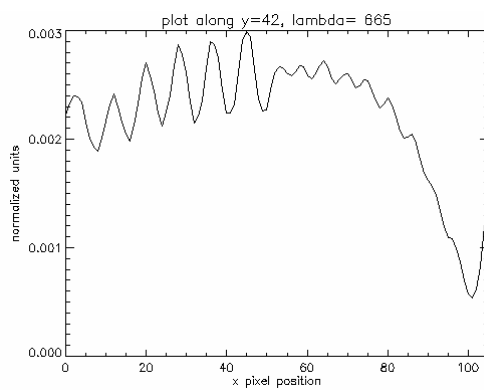


Figure C78: Red and blue bars at 665 nm

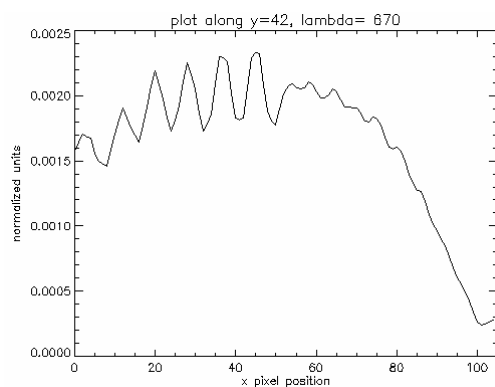


Figure C79: Red and blue bars at 670 nm

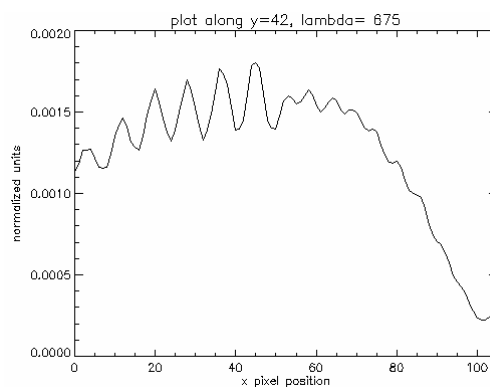


Figure C80: Red and blue bars at 675 nm

The following plots are the spectral signature reconstructions of the HeNe laser line after increasing iterations of either EM or MART reconstruction algorithms.

1 iteration of EM

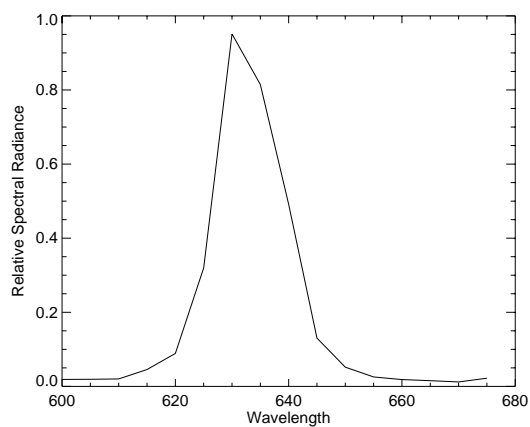


Figure C81: Laser line after 1 EM iteration

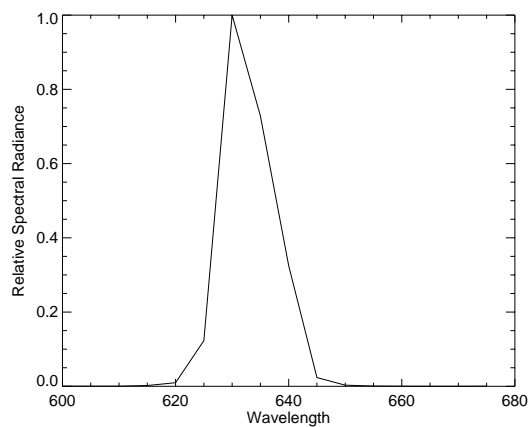


Figure C82: Laser line after 2 EM iterations

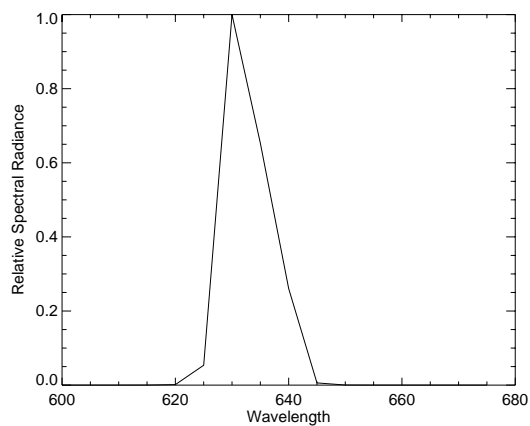


Figure C83: Laser line after 3 EM iterations

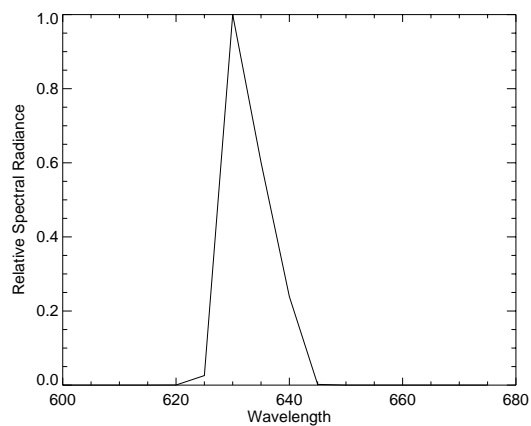


Figure C84: Laser line after 4 EM iterations

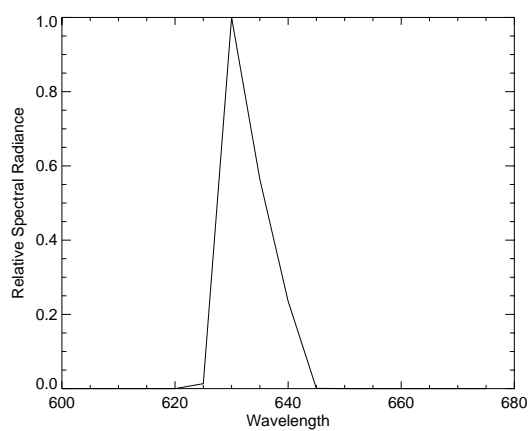


Figure C85: Laser line after 5 EM iterations

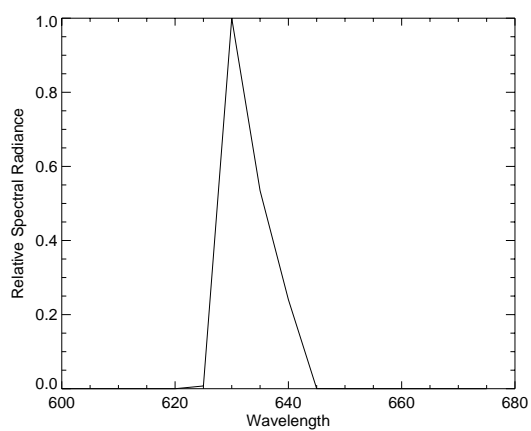


Figure C86: Laser line after 6 EM iterations

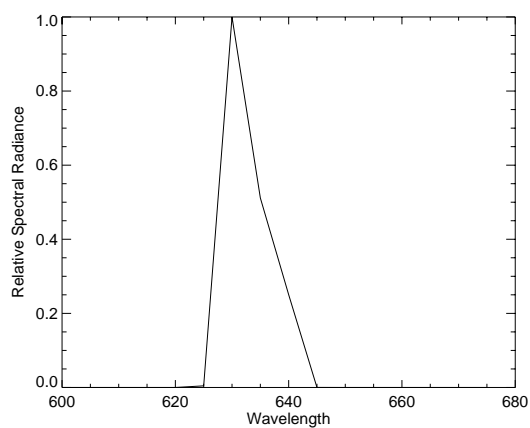


Figure C87: Laser line after 7 EM iterations

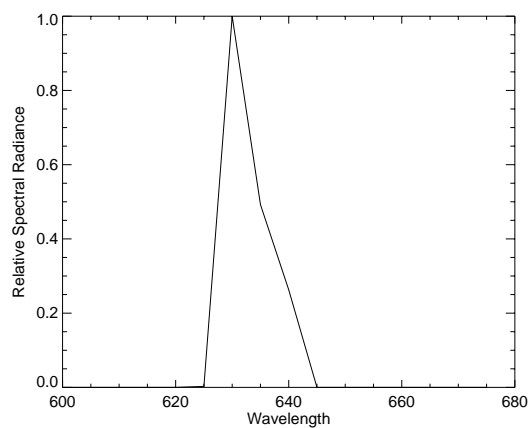


Figure C88: Laser line after 8 EM iterations

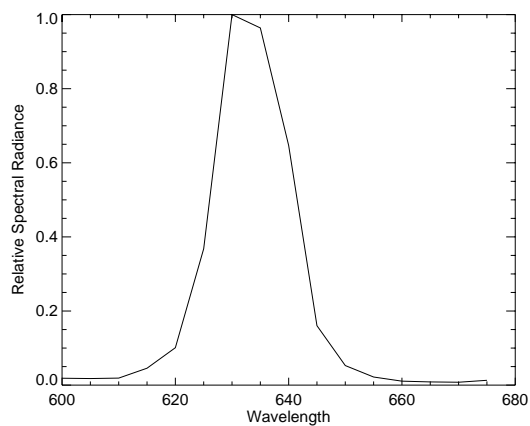


Figure C89: Laser line after 1 MART iteration

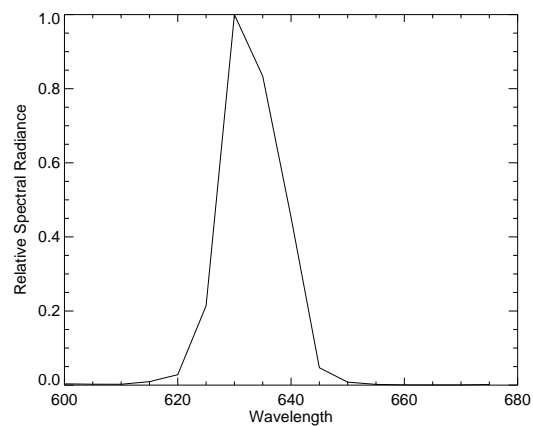


Figure C90: Laser line after 2 MART iterations

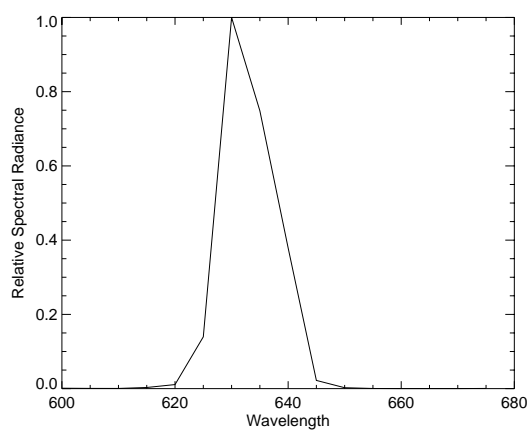


Figure C91: Laser line after 3 MART iterations

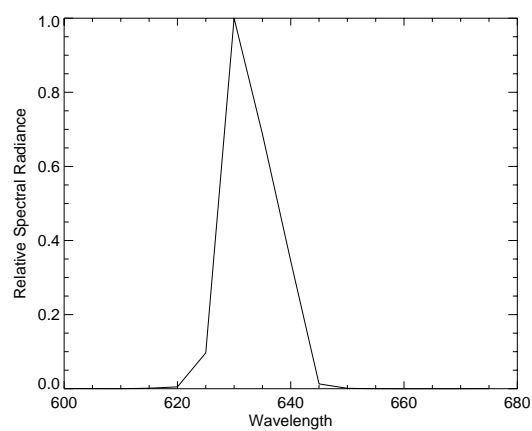


Figure C92: Laser line after 4 MART iterations

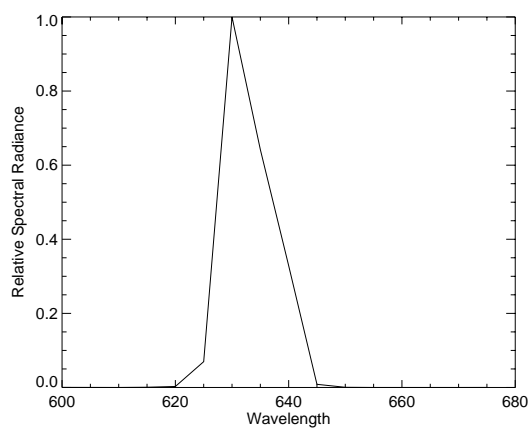


Figure C93: Laser line after 5 MART iterations

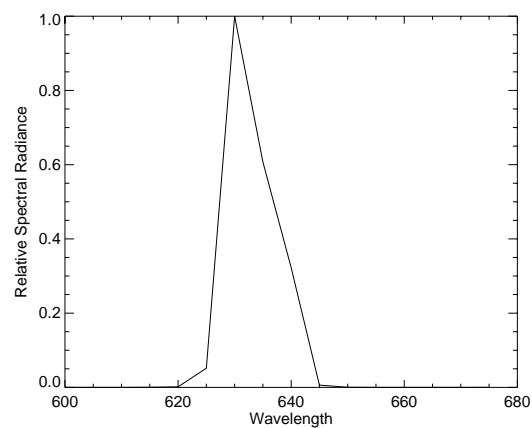


Figure C94: Laser line after 6 MART iterations

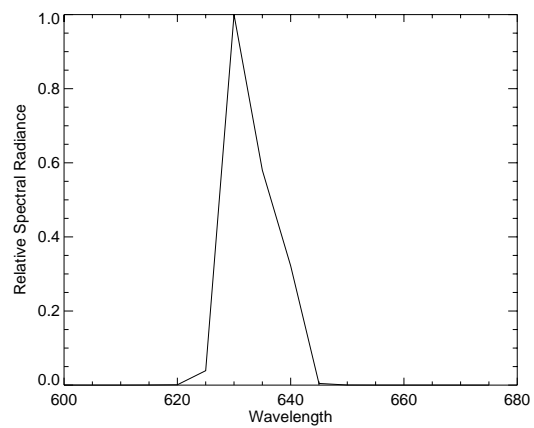


Figure C95: Laser line after 7 MART iterations

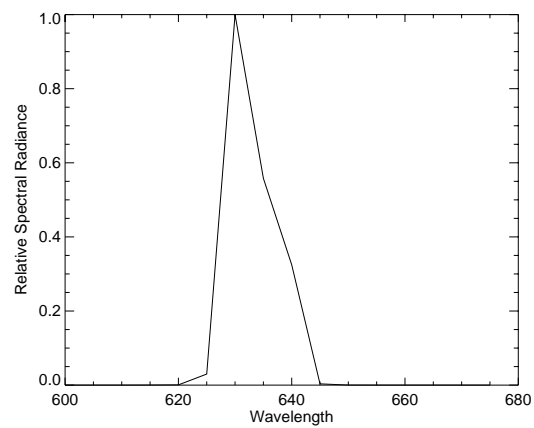


Figure C96: Laser line after 8 MART iterations

## APPENDIX D: IR CTIS PARAMETERS

### D.1. CGH Unit Cell Etch Depth Profile

The following etch depths are in microns and calculated for an index of refraction of 3.42

1.45	1.40	1.16	1.15	0.96	2.38	2.42	2.32	1.49	1.89
1.08	1.26	1.04	4.06	2.51	2.49	2.31	2.40	2.32	1.34
4.49	0.89	0.56	1.00	0.77	2.46	2.59	2.44	2.48	2.52
2.68	0.79	0.04	2.76	2.61	2.65	2.59	2.58	2.71	0.77
2.11	0.45	2.31	0.31	4.27	2.76	2.81	2.91	2.64	2.73
2.15	2.40	2.09	2.63	2.70	2.87	2.92	3.13	3.33	3.42
3.37	2.05	2.38	2.54	4.25	2.81	3.44	3.17	3.44	1.91
1.89	1.91	2.22	2.56	2.58	3.03	0.24	3.46	0.21	3.50
1.61	1.96	1.49	2.51	1.15	2.56	3.99	0.59	4.35	1.77
1.59	1.49	1.41	2.49	2.55	2.44	0.00	1.97	2.14	1.49

Table D1: CGH design etch depth profile

### D.2. Refractive optical element designs.

Using Code V<sup>®</sup> to optimize the lens design, we have the following specifications for each optical component of the IR system

Objective lens, EFL=19.1 mm

Y-Radius	Thickness	Material	Semi-aperture
17.86	5.50	SILICN_SPECIAL	4.81
-126.47	0.60	GERM_SPECIAL	3.94
28.87	10.00		3.81
Infinity	4.56		1.89

Table D2: Objective lens specifications

Collimating and re-imaging lenses, EFL=140 mm

Y-Radius	Thickness	Material	Semi-aperture
131.33	36.00	SILICN_SPECIAL	35.00
-1016.45	6.50	GERM_SPECIAL	29.70
216.28	20.00		28.39
Infinity	88.76		24.81

Table D3: Collimating and re-imaging lens specifications

Off-axis parabola for collimating and re-imaging components of reflective system,  
EFL=140 mm

Y-Radius	Thickness	Material	Semi-aperture	Decenter Type	Y-decenter	Alpha Tilt
Infinity	100		35.00	Decenter and Return	127.39	0.00
-280	0	Reflect	78.01	Basic	13.93	0.00
Infinity	-140		68.42	Basic	12.53	8.67
Infinity	0		1.02	Decenter and Return	7.61	14.75

Table D4: Off-axis parabola specifications

## REFERENCES

- <sup>1</sup> W. R. Dyer and M. Z. Tidrow, "Applications of MCT and QWIP to ballistic missile defense," E.L. Dereniak, R.E. Sampson, eds., in *Proceedings of SPIE*, Vol **3379**, pp 434-440 (1999).
- <sup>2</sup> A.C. Goldberg, et al, "Development of a dual-band LWIR/LWIR QWIP focal plane array for detection of buried mines," E.L. Dereniak, R.E. Sampson, eds., *Proceeding of SPIE* Vol **4721**, pp184-195 (2002).
- <sup>3</sup> W.R. Dyer M.Z. Tidrow, "Applications of MCT and QWIP to ballistic missile defense," E.L. Dereniak, R.E. Sampson, eds. in *Proceeding of SPIE* Vol **3379**, pp. 434-440, (April 1999).
- <sup>4</sup> A.C. Goldberg et.al, "Comparison of HgCdTe and quantum-well infrared photodetector dual-band focal plane array," in *Optical Engineering*, Vol. **42(1)**, p 30-46, (January 2003).
- <sup>5</sup> G. T. Herman, *Image Reconstruction from Projections, The Fundamentals of Computerized Tomography*, Academic Press, New York, (1980).
- <sup>6</sup> J Radon, "Über die bestimmung von funktionen durch ihre integralwert längs gewisser mannigfaltigkeiten", April 1917, in *Computed tomography, proceedings of symposia in applied mathematics*, Vol. **27**, pp 71-86, (1983).
- <sup>7</sup> Ziedses des Plantes, "Eine neue methods zur differenzierung in der roentgenographie," *Acta radiol.*, Vol **13**, pp. 182-192, (1932).
- <sup>8</sup> G.N Hounsfield, "Computed transverse axial scanning (tomography): I. Description of system." in *Brit. J. Radiol.*, Vol. **46**. pp. 1016-1022, (1973).
- <sup>9</sup> G.T. Herman, "Scanning the issue, the special issue on computerized tomography." in *Proceedings of the IEEE*, Vol. **71** no. **3**, pp. 291-292, (March 1983).
- <sup>10</sup> A.C Kak and M. Slaney, *Principles of computerized tomographic imaging*, IEEE Press, New York, pp. 1-3 (1988).
- <sup>11</sup> H.H. Barrett, K.J. Myers, *Foundations of image science*, Wiley. Hoboken, New Jersey, pp. 202-214, (2004).
- <sup>12</sup> D.G. Grant, "Tomosynthesis: a three-dimensional radiographic imaging technique." in *IEEE transactions on biomedical engineering*, Vol **BME-19**, No. **1**, pp. 20-28, (Jan. 1972).

- <sup>13</sup> M.R. Descour, "Non-scanning imaging spectrometry.", Ph.D. Dissertation, University of Arizona, pp. 24-36, (1994).
- <sup>14</sup> C.E. Volin, "Portable snapshot infrared imaging spectrometer", Ph.D. Dissertation, University of Arizona, pp. 32-37, (2000).
- <sup>15</sup> H.H. Barrett, pp. 48-49, (2004).
- <sup>16</sup> M.R. Descour, pp. 70-78, (1994).
- <sup>17</sup> C.E. Volin, pp. 66-88, (2000).
- <sup>18</sup> J.P Garcia and E.L. Dereniak, "Mixed-expectation Image-reconstruction technique." in *Applied Optics*, Vol. **38**, No **17**, pp. 3745-3748, (Jun 1999).
- <sup>19</sup> L. A. Shepp, Y. Vardi, "Maximum likelihood reconstruction for emission tomography." in *IEEE transactions on medical imaging*, Vol. **MI-1**, No. **2**, pp. 113-122, (Oct 1982).
- <sup>20</sup> C.E. Volin, pp. 66-67 (2000).
- <sup>21</sup> A. Lent, "A convergence algorithm for maximum entropy image restoration." in *Image analysis and evaluation, SPSE conference proceedings*, Rodney Shaw, ed., pp. 249-257, (Jul 1976).
- <sup>22</sup> C.E. Volin, p. 68, (2000).
- <sup>23</sup> R. Gordon, R. Bender, G.T. Herman, "Algebraic Reconstruction Techniques (ART) for three-dimensional electron microscopy and X-ray photography.", in *Journal of theoretical biology*, Vol. **29**, pp. 471-481, (Aug 1970).
- <sup>24</sup> J. Hartke, E Dereniak, "Hyperspectral-dual spectral region imaging spectrometer." In *Proc of SPIE*, E.L. Dereniak, R.E. Sampson, eds, Vol. **5563**, pp. 156-166, (2004).
- <sup>25</sup> R.W. Gerchberg and W.O. Saxton, "A practical algorithm for the determination of phase from image and diffraction plane pictures," in *Optik* **35**, pp. 237-246, (1972).
- <sup>26</sup> S. Kirkpatrick, C.D. Gelatt, M.P. Vecchi, "Optimization by simulated annealing," in *Science* Vol. **220**, pp. 671-680, (1983).

- <sup>27</sup> P.E. Keller, A.F. Gmitro, "Design and analysis of fixed planar holographic interconnects for optical neural networks," in *Appl. Opt.* Vol. **31**, pp. 5517-5526, (1992).
- <sup>28</sup> E.G. Johnson and M.A.G. Abushagur, "Microgenetic algorithm optimization methods applied to dielectric gratings," in *JOSA A*, Vol. **12**, p.1152, (1995).
- <sup>29</sup> C.E. Volin, M.R. Discour and E.L. Dereniak, "Design of broadband-optimized computer-generated hologram dispersers for the computed-tomography imaging spectrometer," in *Proc. of SPIE*, M.R. Descour, S.S. Shen, eds., Vol. **4480** pp 377-387, (2002).
- <sup>30</sup> C. E. Volin, (2000).
- <sup>31</sup> C. P. Tebow, E. L. Dereniak, D. Garrood, and C. E. Volin, "Tunable snapshot imaging spectrometer," in *Proc. of SPIE*, S.S. Shen, P.E. Lewis, eds., Vol **5159**, pp 64-72, (2003).
- <sup>32</sup> J. Mathews, R.L. Walker, "Mathematical Methods of Physics" 2<sup>nd</sup> Edition, Addison-Wesley Publishing, pp. 322-340, (1964).
- <sup>33</sup> W.J. Dallas, "Phase quantization – a compact derivation", *Appl. Optics* **10**, pp. 673-674, (1971).
- <sup>34</sup> E Cho et al, "Development of a QWIP dual-color FPA for mine detection applications", in *Proc of SPIE*. B.F. Andresen, G.F. Fulop, eds., Vol. **5074**, pp. 685-695, (2003).
- <sup>35</sup> S.D. Gunapala, S.V. Bandara, et al, "MWIR & LWIR megapixel QWIP focal plane arrays," in *Proc of the SPIE*, E.L. Dereniak, R.E. Sampson, eds., Vol **5563**, p141-148, (2004).
- <sup>36</sup> W. Cabanski, R. Breiter, et al. "Status of 3<sup>rd</sup> gen focal plane array IR detection modules at AIM," In *Proc of SPIE*, B.F. Andresen, G.F. Fulop, eds., Vol. **5074**, pp. 72-82, (2003).
- <sup>37</sup> B. McQuiston, E. Cho et.al., "QWIP chip dual-color and multi-color FPAs for military applications," in *Proc of SPIE*, R.G. Driggers, D.A. Huckridge, eds., Vol. **5612**, pp. 51-62, (2004).
- <sup>38</sup> W. Cabanski, K Eberhardt, et.al. "3<sup>rd</sup> gen focal plane array IR detection modules and applications," in *Proc of SPIE*, B.F. Andresen, G.F. Fulop, eds., Vol **5406**, pp 184 – 192, (2004).

- <sup>39</sup> E.L. Dereniak, G.D. Boreman, *Infrared Detectors and System*, Wiley, New York, pp. 348-350, (1996).
- <sup>40</sup> P.D. LeVan, private communications, (June, 2005).
- <sup>41</sup> Rogalski, "Toward Third Generation HgCdTe Infrared Detectors," in *Journal of Alloys and Compounds*, Vol. **371**, pp. 53-57, (2004).
- <sup>42</sup> M.B. Reine et al, "Simultaneous MW/LW dual-band MOVPE HgCdTe 64x64 FPAs", in *Proc. of SPIE*, E.L. Dereniak, R.E. Sampson, eds., Vol. **3379**, pp.200-212, (1998).
- <sup>43</sup> B McQuiston et.al "QWIP chip dual-color and multi-color FPAs for military applications," in *Proc. of SPIE*, R.G. Driggers, D.A. Huckridge, eds., Vol. **5612**, pp. 51-62, (2004).
- <sup>44</sup> A.C. Goldberg, S W Kennerly et.al. "Comparison of HgCdTe and quantum-well infrared photodetector dual-band plane arrays," in *Optical engineering*, Vol **42(1)**, pp. 30-46, (Jan. 2003).
- <sup>45</sup> W.L. Wolfe, G.J. Zissis, "The infrared handbook revised edition", Office of Naval Research, pp. 7-17 - 7-77, (1985).
- <sup>46</sup> C.E. Volin, pp. 66-88, (2000).
- <sup>47</sup> J.F. Scholl, et.al, "Phase grating design for a dual-band snapshot imaging spectrometer", *Appl Optics*, Vol. **42**, no 1, pp. 18 – 29, (Jan 2003).
- <sup>48</sup> R.S. Sokolova, N.A. Pashkova, "Multispectral antireflection coatings for the IR region," in *J. Opt. Technol.* Vol. 69 (2), pp. 86-87, (Feb 2002).
- <sup>49</sup> H.A. Macleod, private communications, (May 2005).
- <sup>50</sup> A. Mann, *Infrared optics and zoom lenses*, SPIE Press, Bellingham, Wa., pp. 23-24, (2000).
- <sup>51</sup> H.H Barrett, pp 479-507, (2004).